UNIVERSITY OF RIJEKA

FACULTY OF PHYSICS

Ivan Kovač

CHARGE CARRIER DYNAMICS ACROSS INORGANIC MANGANESE PEROVSKITES AND METAL OXIDES INTERFACES

DOCTORAL THESIS

Rijeka, 2026.

UNIVERSITY OF RIJEKA

FACULTY OF PHYSICS

Ivan Kovač

CHARGE CARRIER DYNAMICS ACROSS INORGANIC MANGANESE PEROVSKITES AND METAL OXIDES INTERFACES

DOCTORAL THESIS

Supervisor: Prof. Igor Lukačević

Co-supervisor: Assoc. Prof. Robert Peter

Rijeka, 2026.

SVEUČILIŠTE U RIJECI

FAKULTET ZA FIZIKU

Ivan Kovač

DINAMIKA NOSIOCA NABOJA KROZ MEĐUSLOJEVE ANORGANSKIH MANGANOVIH PEROVSKITA I METALNIH OKSIDA

DOKTORSKA DISERTACIJA

Mentor: prof. dr. sc . Igor Lukačević

Komentor: izv. prof. dr. sc. Robert Peter

Rijeka, 2026.

Mentor rada: prof. dr. sc. Igor Lukačević

Komentor rada: izv. prof. dr. sc. Robert Peter

Doktorski rad obranjen je dana _____ u/na _____

_____, pred povjerenstvom u sastavu:

1. _____
2. _____
3. _____
4. _____
5. _____

Acknowledgments

This work was supported by Croatian Science Foundation (HRZZ) under the grants HRZZ-IP-2018-01-5246 and HRZZ-DOK-2021-02-2147, by the Josip Juraj Strossmayer University of Osijek under the grant OFIZ-INT-2023-1, and by the HPC-Europa3 (Horizon 2020 programme) under the grant HPC17CH6I0. For starters, I would like to thank my supervisor Igor for helping me throughout this journey, for giving valuable advice, for having patience, and for keeping me from going astray, as I often get curious about various things that should not be the main focus of my work. I would also like to thank my supervisor for encouraging me to go on a research visit to ICTP when I first started my PhD, and for all the help with getting the funding from HPC-Europa3 project. I would also like to thank Robert for accepting to be my co-supervisor, although the topic of this thesis is not his field of research. Big thank you goes to my sisters Marija and Danijela and their families, who have always supported me and have always been by my side. Going through very difficult times together has built our bond, and I am grateful for having them by my side through difficult and good times. To my wife's family, I express big gratitude for quickly accepting me and for supporting me, especially throughout a very important period of my education. To my wife Gabrijela, and my beautiful daughter Eva, who have constantly reminded me why this is all worth it. After long days, spending time with them shone a light on it, and kept me going forward. A big thank you goes to SOS Children's Village organization, which provided me with everything I required to progress and achieve what I wanted to achieve, and supported me throughout my education, as well as my many other interests. There, I encountered many lovely people who raised me, and although I have been surrounded by many lovely people throughout my time in SOS Children's Village, I have to highlight and express my utmost gratitude to Željko, who has been of immense importance in my success, and believed in me when things did not go so smoothly. He stood by me in the toughest times, and is a crucial part of my academic achievements.

Abstract

Perovskite materials have stood out as excellent candidates for solar cell applications, and have been heavily studied over the last fifteen years. High power conversion efficiency has been achieved, surpassing standard silicon-based solar cells. On the other hand, throughout the years stability of perovskite based solar cells has been a highly investigated issue. The use of organic components and ion migration have been pointed out as two most impactful factors regarding the stability. Furthermore, all perovskites used in high efficiency devices contain lead, which can pose a problem for later disposal of unusable solar panels. This work proposes several inorganic manganese perovskites as potential candidates for solar cell applications. First, properties relevant for the use as optical absorbers have been studied. The study has shown that they posses desirable band gaps for optical absorption, as well as good absorption throughout the visible part of the spectrum, together with high joint density of states. Next, interface properties have been studied. Due to the architecture of perovskite solar cells, interface properties of perovskite absorber with surrounding charge transport layers are crucial for optimal device operation. After confirming that considered perovskites posses desirable electronic properties, the properties of their interfaces with metal oxide electron transport layers were investigated. This included investigation of properties that govern charge dynamics, such as effective mass, charge density, electrostatic potential, band offset, and formation of interface trap states. Several metal oxide/perovskite combinations showed favourable band offset which promotes efficient electron diffusion into electron transport layer. On the other hand, formation of interface trap states has been observed in several cases, which promotes charge recombination and often leads to reduced device efficiency. To deduce the impact of these factors on the device operation, further studies based on macroscopic models are required. In the end, possible future research directions are proposed.

Keywords: Absorber, band offset, charge carrier dynamics, electron transport layer, interface.

Sažetak

Perovskitni materijali istaknuli su se kao izvrsni kandidati za primjenu u solarnim ćelijama te su intenzivno proučavani tijekom posljednjih petnaest godina. Postignuta je visoka učinkovitost pretvorbe energije koja nadmašuje standardne solarne ćelije na bazi silicija. S druge strane, stabilnost solarnih ćelija na bazi perovskita godinama je bila predmetom brojnih istraživanja. Korištenje organskih komponenti i migracija iona istaknuti su kao dva najutjecajnija faktora s obzirom na stabilnost. Nadalje, svi perovskiti koji se koriste u uređajima visoke učinkovitosti sadrže olovo, što može predstavljati problem pri kasnijem odlaganju neupotrebljivih solarnih panela. Ovaj rad predlaže nekoliko anorganskih manganovih perovskita kao potencijalnih kandidata za primjenu u solarnim ćelijama. Za početak, proučena su relevantna svojstva za primjenu ovih materijala kao optičkih apsorbera. Istraživanje je pokazalo da posjeduju poželjne energijske procijepe za optičku apsorpciju, kao i dobru apsorpciju u vidljivom dijelu spektra, zajedno s visokom združenom gustoćom stanja. Potom su ispitana svojstva spoja dvaju materijala. Zbog arhitekture perovskitnih solarnih ćelija, svojstva spojeva između perovskitnog apsorbera i okolnih slojeva za transport naboja ključna su za optimalan rad uređaja. Nakon potvrde da razmatrani perovskiti posjeduju poželjna elektronska svojstva, istražena su svojstva njihovih spojeva s metalnim oksidima koji se koriste kao slojevi za transport elektrona. To je uključivalo istraživanje parametara koji određuju dinamiku naboja, kao što su efektivna masa, gustoća naboja, elektrostatski potencijal, pomak energetskih vrpci i stvaranje zamki (trap states) na spojevima. Nekoliko kombinacija metalnih oksida i perovskita pokazalo je povoljan pomak vrpci koji omogućuje efikasnu difuziju elektrona u sloj za transport elektrona. S druge strane, u nekoliko je slučajeva uočeno stvaranje zamki na spoju dvaju materijala, što potiče rekombinaciju naboja i često dovodi do smanjene učinkovitosti uređaja. Kako bi se izveo zaključak o utjecaju ovih čimbenika na rad uređaja, potrebne su daljnja istraživanja bazirana na makroskopskim modelima. Na kraju rada predloženi su mogući smjerovi budućih istraživanja.

Ključne riječi: Absorber, pomak vrpci, dinamika nosioca naboja, sloj za prijenos elektrona, međusloj.

Contents

List of Figures

List of Tables

List of Abbreviations

BMO barium manganite - $BaMnO_3$

CBM conduction band minimum

CBO conduction band offset

CMO calcium manganite - $CaMnO_3$

DFT density functional theory

EQE effective quantum efficiency

ETL electron transport layer

FAPI formamidinium lead iodide

HTL hole transport layer

JDOS joint density of states

LDA local density approximation

MA methylammonium

MAPI methylammonium lead iodide

PCE power conversion efficiency

PSC perovskite solar cell

SIE self-interaction error

SMO strontium manganite - $SrMnO_3$

TCO transparent conductive oxide

VBM valence band maximum

Chapter 1

Introduction

The rapid progress of society and significant technological advances rely heavily on the research of materials that can mediate such progress. One field of enduring interest is green energy. Solar panels have been in use for several decades, but total electrical energy production is still dominated by fossil fuels. Although silicon is an abundant element, the monocrystalline silicon often used in solar cells to improve efficiency is expensive due to high manufacturing costs. For the past 15 years, there has been a great interest in solar cells based on the perovskite materials, ever since the work of Kojima et al. [1]. First perovskite materials proposed for solar cells were methylammonium lead iodide (MAPI) and formamidinium lead iodide (FAPI). Despite initial test results showing limited promise for these materials (power conversion efficiency (PCE) of 3.81% for MAPI and 3.18% for FAPI), the abundant resources for their fabrication, low exciton binding energy, appropriate band-gap, and high electron mobility have prompted significant research and development efforts aimed at enhancing their performance. Recently, the solar cells based on perovskite materials surpassed silicon based solar cells in terms of efficiency, with record PCE of 26% [2]. However, the long-term stability of mixed organic-inorganic halide perovskites remains a primary challenge for practical application; specifically, instability towards moisture, illumination, and temperature must be mitigated for successful commercialization [3–5]. Investigation of degradation mechanisms has shown that the largest contributor towards the degradation of MAPI when exposed to light, moisture, and heat, is the methylammonium (MA) organic cation. The volatile reactions of the organic cation when exposed to environmental conditions quickly degrades MAPI performance. To deal with this, inorganic cation substitution for MA has been proposed, and has been highly investigated during the last 10 years [6]. The most promising candidates so far in the family of inorganic perovskites for PSC applications are $CsPbI_3$ and $CsPbBr_3$, due to higher resistance towards the environmental conditions [7, 8]. However, the efficiency of inorganic perovskites still hasn't reached the level of mixed halide perovskites, although

it is steadily increasing [9]. The potential issue with $CsPbI_3$ perovskite is its phase instability. Large ionic radius of caesium causes the perovskite to undergo a phase transition into a non-perovskite phase [8]. Inorganic perovskite composed of mixed halide anions has been investigated, where it was found that the mixing of iodide and bromide halogens in $CsPbI_{3-x}Br_x$ composition can lead to improved phase stability [10].

In addition, a significant drawback of inorganic perovskites such as $CsPbI_3$ and $CsPbBr_3$ is the continued incorporation of lead in their composition, which poses environmental challenges for the eventual disposal of solar panels. To address this, the partial replacement of toxic Pb^{2+} ions was investigated by Frolova et al. [11]. Their study demonstrated that only a partial substitution of Pb^{2+} with Hg^{2+}, in the form of $CH_3NH_3Pb_{1-x}Hg_xI_3$, leads to improved optoelectronic properties, such as higher PCE and effective quantum efficiency (EQE). However, the fact that performance was positively affected only for small fractions of Hg^{2+} (at most 15%) indicates that Pb^{2+} cannot be effectively replaced by more than a minor fraction without degrading device performance. Therefore, alternative perovskite compositions that exclude both toxic lead and volatile organic components are highly desirable to ensure long-term stability.

In most literature reviews, two factors are cited as having the greatest impact on overall PSC efficiency and stability: defects and interface properties. As individual materials, such as perovskite absorbers, are optimized, their internal defect density becomes negligible. Consequently, the majority of defects in modern PSCs occur at the interfaces [12]. For this reason, interface engineering has become a primary research focus for the further improvement of PSC technology.

1.1 Perovskites

Perovskites are a family of materials that have been known for nearly 200 years, with naturally occurring calcium titanate $CaTiO_3$ the first discovered perovskite. Perovskites are now a well known family of materials, where the chemical formula ABX_3 is shared amongst them. They have attracted the most attention with their excellent properties for optical absorption, as well as abundance of sources for their fabrication. They contain two cations (A and B) and three anions (X_3) in their primitive cell. The MAPI perovskite is formed from methylammonium $CH_3NH_3^+$ cation, Pb^{2+} cation and three I^- anions. In the cubic structure, MAPI $B-$site cation (Pb^{2+}) is 6-fold coordinated with iodide anions (I^-), which can be seen in Figure 1.1.

This arrangement of iodide anions forms an octahedron around Pb^{2+} cation, where MA organic cation is settled in between the octahedra. Other perovskite lattices are then formed by the octahedral distortion. The type of perovskite lattice can be predicted by knowing the ionic radii of the ions forming the perovskite structure through the Goldschmidt tolerance

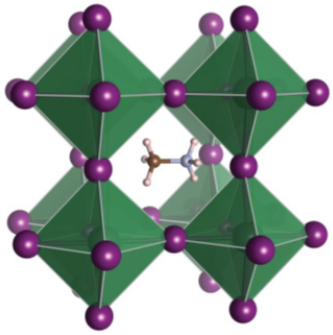

Figure 1.1: *Methylammonium lead iodide cubic perovskite structure showing corner sharing octahedra. Image taken from reference [13].*

factor [14]

$$t = \frac{r_A + r_X}{\sqrt{2}(r_B + r_X)}, \tag{1.1.1}$$

where r_A is the radius of the $A-$site cation, r_B is the radius of the $B-$site cation, and r_X is the radius of the anion. For the tolerance factor below 0.71, different non-perovskite structures are formed. Orthorhombic or rhombohedral perovskite structures are formed for tolerance factor in the range from 0.71 to 0.9, ideal cubic perovskite structure from 0.9 to 1.0, and hexagonal or tetragonal perovskite structures are formed for Goldschmidt tolerance factor slightly above 1.0. Consequently, the resulting crystal structure is primarily determined by the ratio of the $A-$site and $B-$site ionic radii. Other than solar cell applications, this family of materials is suitable for various technologies as they often exhibit properties such as ferroelectricity, ferromagnetism, multiferroicity, low exciton binding energy, and high electron mobility.

The wide range of tolerance factors that support the perovskite structure allows for significant flexibility in compositional tuning. It was shown previously that the partial exchange of $X-$site halide anion results in band gap modification [15]. In general, in perovskites, $B-$site cation and $X-$site anion are responsible for the optoelectronic properties of the perovskite, while $A-$site cation regulates structural stability through its larger ionic radius, and only indirectly affects optoelectronic properties, as its radius affects bond length and bond angle of the BX_6 octahedron. In a recent review on the performance and stability of perovskites [16], it was pointed out that multicomponent perovskites composed of various fractions of different ions are a promising strategy for improving stability, but can also improve performance in various ways. For perovskites as ionic systems, migration of mobile ions has also been detected as a significant contributor towards poor stability [17, 18]. Multicomponent perovskite formed as $Cs_{0.05}(FA_{0.83}MA_{0.17})_{0.95}Pb(I_{0.83}Br_{0.17})_3$ was investigated, and it was shown to have higher activation energy of mobile ions. This leads to improved stability as it reduces the negative effects of ion migration on the per-

ovskite stability. The multicomponent perovskite approach alternatively provides a way to tune both the lattice parameter and the band gap.

1.2 Perovskite solar cells

To have a better understanding of the importance of the research conducted within this thesis, next sections are focused on providing a basic understanding of PSC operation and architecture to get an overview of what drives the energy conversion in these devices. At the end of this section, a brief explanation on the scientific interest and contribution expected from this work is given.

1.2.1 Perovskite solar cell architecture and operation

PSC's are composed of layers of several different materials. Each of the materials has a distinct role within the cell. In both the so-called planar architecture and inverted planar architecture the same five layers are used, with only difference being the order in which the layers are stacked; metal electrode, hole transport layer (HTL), perovskite absorber, electron transport layer (ETL), and transparent conductive oxide (TCO). In Figure 1.2 both architectures are displayed. Although perovskite can serve several roles within PSC, its main role is as the optical absorber. Two very important layers in PSC are also charge transport layers, as they have an important task of transporting generated charge carriers towards respective electrodes.

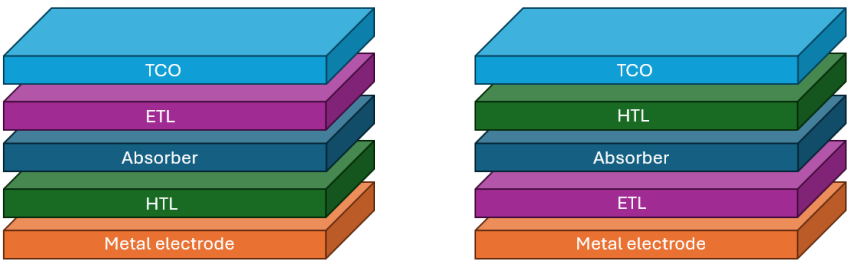

Figure 1.2: *Typical PSC architectures; planar (left) and inverted planar (right).*

When the sunlight reaches the surface of the PSC, it first encounters the two top layers in the planar architecture, which are formed by transparent conductive oxide TCO and ETL, both being large band gap semiconductors. Considering the transparency of both of these layers towards the visible light, it is transmitted to the perovskite layer. The photons with sufficient energy excite electrons from the valence band of the perovskite, creating electron-hole pairs (excitons). Because typically used perovskites have low exciton-binding energy,

in the order of 10 meV to 34 meV, electrons can easily be promoted from excitonic energy levels into the conduction band to become conduction electrons, i.e., free charge carriers.

Photo-generated electrons in the conduction band subsequently diffuse into the ETL, provided there is an energetically favorable band offset at the interface. Simultaneously, the resulting holes at the valence band maximum of the perovskite are extracted by the HTL. The required energy alignment is illustrated in Figure 1.3, where the rectangular boundaries represent the respective band edges. Facilitated by the high electron mobility in the ETL and high hole mobility in the HTL, these charge carriers are efficiently transported to and collected at the respective electrodes. The resulting accumulation of opposite charges—electrons at the TCO and holes at the metal electrode—generates the photovoltage.

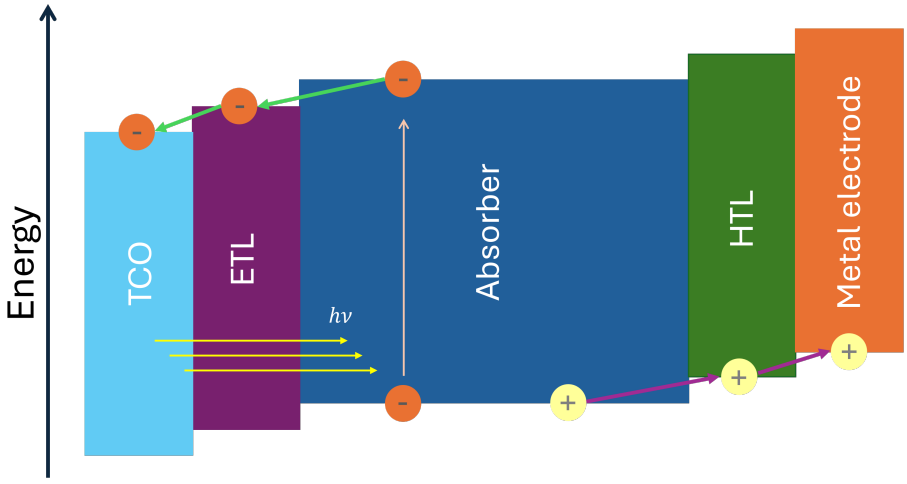

Figure 1.3: *A diagramatic display of the process of charge separation and transport within the perovskite solar cell.*

1.2.2 Interfaces in perovskite solar cells

Because of the architecture of PSC, there are four distinct interfaces between different materials. The properties at the interfaces between these materials, especially between the perovskite with surrounding charge transport layers, are of vital importance for efficient operation of the PSC. For optimal operation of the device, numerous factors need to be considered, such as lattice mismatch at the interfaces, materials processing, energy band alignment, defect density, etc. [19–24]. Various approaches have been explored over the years to deal with many of the aforementioned factors, including selective contacts which do not cause degradation of the perovskite active layer, defect passivators, interface engineering to influence band alignment, and materials processing engineering, to determine processing methods which do not cause the degradation of the substrate layers. As

good candidates for the individual roles have already been largely known and explored, the research thus far in the area of interfaces has been mostly focused on improving the interface properties between those materials.

In the work by Mosconi, Ronca and de Angelis [25], the addition of chlorine at the interface of MAPI with TiO_2 electron transport layer was investigated, where $MAPbI_{3-x}Cl_x$ mixed-halide perovskite was formed at the interface. Stronger coupling was observed at the interface containing chlorine in the $MAPbI_{3-x}Cl_x$ perovskite compared to the typical $MAPbI_3$ perovskite. It was expected that the stronger coupling should lead to more efficient electron collection at the interface, positively affecting PSC efficiency. In their next work, the same authors investigated the effect of excess of PbI_2 on the properties of the MAPI and TiO_2 interface. In this combined theoretical and experimental study, it was observed that excess PbI_2 from the precursor is mostly found at the interface of MAPI and TiO_2 ETL and favourably influences charge transfer of electrons from the perovskite layer towards the electron transport layer, hence positively contributing to the solar cell efficiency.

In the work by Welch et al., the stability of interfaces was investigated for various surface terminations of inorganic perovskite $CsPbBr_3$ with CuI hole transport layer [26]. Together with the study of interface stability in terms of the interface energy for various surface terminations, investigation of band offset and potential difference was conducted. A potential difference which should benefit charge separation was observed. It was also observed that the band offset type changes with the change in the number of layers indicating the possibility to tune band offset by controlling the layer thickness.

The theoretical approach based on DFT has previously also been used to investigate trap states at the interfaces of tunnel field-effect transistors (TFET). Although this is not directly related to solar cell applications, the implication that the DFT method can be effectively used to detect and characterize trap states is still relevant. This approach can be readily adapted to study interface defects within solar cell architectures. For instance, a study conducted by a group from ETH in Zürich investigated the origin of performance-limiting trap states at the interface of InAs and Si [27]. The electronic structure calculations revealed that the interface trap states originate from unsaturated arsenic orbitals. It was also proposed that hydrogen or sulphur atoms could be used to saturate the unsaturated orbitals, and hence passivate the interfacial defects. This shows the viability of theoretical approaches based on DFT to study various defects at the interfaces.

Previously, the implementation of barium titanate ($BaTiO_3$) buffer layer between perovskite absorber and metal oxide electro transport layer was studied [28]. The intrinsic ferroelectric property of $BaTiO_3$ was expected to aid in charge separation, which should lower recombination rate. However, to further study the impact of the added buffer layer, the interface properties with metal oxides of ZnO, SnO_2 and TiO_2 were studied. The study

was focused on charge dynamics, notably band offset and effective mass. A competition between different interface properties that govern the charge dynamics was revealed. Additionally, controllable parameters through which interface engineering can be implemented to obtain desirable properties were defined in this work.

The primary objective of this study is to investigate the properties of calcium manganite - $CaMnO_3$ (CMO) as an optical absorber. While CMO has been previously explored as an ETL to replace the conventional TiO_2 [29, 30], recent reports indicate that it also possesses a favorable bandgap and optical characteristics suitable for visible light absorption [30]. Consequently, the first part of this thesis evaluates the relevant properties of CMO as an optical absorber, alongside two derivative perovskites in which the A-site cation is substituted with strontium (strontium manganite - $SrMnO_3$ (SMO)) and barium (barium manganite - $BaMnO_3$ (BMO)). The findings of this initial investigation have been published in a peer-reviewed journal [31].

It is hypothesized that A-site substitution will not significantly diminish the favorable optical properties observed in CMO. Instead, this substitution is expected to primarily influence the interface dynamics with the adjacent ETL. This hypothesis forms the core of this thesis, which investigates the interface properties governing the transport of photogenerated charge carriers from the perovskite absorbers (CMO, SMO, and BMO) into metal-oxide ETLs (ZnO, SnO_2, and TiO_2). The principal results of this work have also been published in a peer-reviewed journal [32]. The selected metal oxides were chosen for their prevalence in high-performance PSCs and their beneficial electronic properties; a detailed discussion of these materials and their role as ETLs is provided in Chapter 3.

The thesis is based on several papers, as follows:

- M. Mužević et al. "Potential of AMnO3 (A = Ca, Sr, Ba, La) as Active Layer in Inorganic Perovskite Solar Cells." In: Chemphyschem : a European journal of chemical physics and physical chemistry (2023).
  Doctoral candidate's contribution: Simulations of electronic band structures and correlation with structural and optical properties of inorganic manganese perovskites ($XMnO_3$, X = Ca, Sr, Ba, La). The results published in this paper are presented in Chapter 3.

- I. Kovač et al. "Charge carrier dynamics across the metal oxide/BaTiO3 interfaces toward photovoltaic applications from the theoretical perspective". In: Surfaces and interfaces 39 (2023), p. 102974.
  Doctoral candidate's contribution: Doctoral candidate has led and coordinated the research for this paper. The candidate also did most of the calculations which were conducted and from which the results were obtained for this paper. Doctoral candidate additionally contributed with validation, visualization, formal analysis,

investigation, data curation, writing of the review and editing. Methodological approach used within this work is used throughout chapter 5. Main results are not explicitly presented in the thesis.

- I. Kovač et al. "Insights into the charge dynamics at metal oxide/manganate perovskite interfaces from density functional theory". In: Applied Surface Science (2026), p. 166497. issn: 0169-4332. doi: https://doi.org/10.1016/j.apsusc.2026.166497.
  Doctoral candidate's contribution: Conducted most of the calculations required for the investigation of metal oxides-perovskites interfaces, analysed structural and electronic properties of the interfaces, calculated relevant quantities that determine charge carrier dynamics across the interface, and also contributed through formal analysis, investigation, resources, validation, visualization and writing of the original draft. The main results and methodology used in this work are the focus of the doctoral thesis and are presented in chapter 5.

Chapter 2

Theoretical methods

2.1 Density functional theory (DFT)

Density functional theory has become a widely known tool for obtaining ground state properties of periodic systems. This approach can be very valuable for investigating unknown properties of novel systems, but also for investigating properties that are very difficult or impossible to measure with experimental techniques. Throughout this section the basics of density functional theory (DFT) will be explained to have a better understanding of how it can be effectively used and how it is valuable for materials science.

To determine various properties of the quantum mechanical systems, Schrödinger equation needs to be solved to obtain the energies of the system of interacting particles. The Hamiltonian describing the system of interacting electrons and nuclei can be written in the following form:

$$H = -\frac{\hbar^2}{2m_e}\sum_i \nabla_i^2 - \frac{1}{4\pi\epsilon_0}\sum_{i,I}\frac{Z_I e^2}{|\mathbf{r}_i - \mathbf{R}_I|} + \frac{1}{8\pi\epsilon_0}\sum_{i\neq j}\frac{e^2}{|\mathbf{r}_i - \mathbf{r}_j|} - \sum_I \frac{\hbar^2}{2M_I}\nabla_I^2 + \frac{1}{8\pi\epsilon_0}\sum_{I\neq J}\frac{Z_I Z_J e^2}{|\mathbf{R}_I - \mathbf{R}_J|}. \quad (2.1.1)$$

The first term represents the kinetic energy of the electrons, the second term is the Coulomb interaction between electrons and nuclei, where Z_I is the atomic number of the nuclei with index I, third term is the electron-electron Coulomb repulsion, the fourth term is the kinetic energy of the nuclei, and the last term is the nuclei-nuclei Coulomb repulsion. Upper case indices denote the nuclei, and lower case indices denote the electrons. In the following expressions, the Hamiltonian form will be simplified by including Hartree atomic units, where $\hbar = m_e = e = 4\pi\epsilon_0 = 1$.

All of the systems which will be investigated incorporate what is called Born-Oppenheimer approximation. Within Born-Oppenheimer approximation, due to a larger mass of the nu-

clei relative to electronic mass, the nuclei are approximated as immobile. Therefore, in the total Hamiltonian the nuclei-nuclei Coulomb interaction is considered as constant, as the positions of the nuclei remain constant. Also, the potential that nuclei create is thought of as a background potential which also includes the electrons which are tightly bound to the core. Thus, within these models, only the valence electrons are explicitly treated, and core electrons are considered to create a background potential together with positive nucleus. Additionally, as nuclei are approximated as immobile, their kinetic energy is approximated to be zero. Energy due to interaction between nuclei can be later added to the so-called electronic Hamiltonian. With nuclei-nuclei interaction term excluded, the electronic Hamiltonian can be written as

$$H = -\frac{1}{2}\sum_i \nabla_i^2 - \sum_{i,I} \frac{Z_I e^2}{|\mathbf{r}_i - \mathbf{R}_I|} + \frac{1}{2}\sum_{i \neq j} \frac{e^2}{|\mathbf{r}_i - \mathbf{r}_j|}, \tag{2.1.2}$$

to which, in the end, the nuclei interaction term is added, which is typically denoted as E_{II}.

2.1.1 Hohenberg - Kohn energy functional

Although electron density implementation into many-electron systems came in 1927. by Thomas and Fermi [33, 34], the DFT as we know it today started with the work of Hohenberg and Kohn. In their paper published in 1964. titled "Inhomogeneous electron gas" [35], they showed that the total energy of a system is a unique functional of electron density of that system. Therefore, by finding the ground state density of a many-electron system, one uniquely determines its properties. Further, they proved that the ground state density obtained this way is in fact the exact ground state density that minimizes the total energy. The work of Hohenberg and Kohn still did not lead to a conclusion on how to effectively use this model, as it needs to include the correlation of electrons, and it needs to obey the Pauli exclusion principle. However, this leads to an energy functional which is charge density dependent, rather than being dependent on the exact positions of the electrons. As electron density is a function which depends on three parameters, energy becomes a function of three variables, rather than 3N, where N is the number of electrons in a system. No matter how many electrons a system has, energy is always dependent on three parameters. This energy functional has the form

$$E[n(\mathbf{r})] = T[n(\mathbf{r})] + E_{int}[n(\mathbf{r})] + \int V_{ext}(\mathbf{r}) n(\mathbf{r}) d^3r + E_{II}, \tag{2.1.3}$$

where $n(\mathbf{r})$ is electron density, $T[n(\mathbf{r})]$ is electron kinetic energy, $E_{int}[n(\mathbf{r})]$ is the energy due to electron-electron interaction, $V_{ext}(\mathbf{r})$ is the external potential generated by nuclei and

core electrons which acts on the valence electrons, and E_{II} is the nuclei-nuclei interaction energy. The real difficulty remaining is applying this to an interacting many-body system.

2.1.2 Kohn - Sham equations

The Kohn-Sham approach is based on the replacement of the difficult to solve many-body system of interacting particles with a system of non-interacting particles [36]. This is under assumption that their ground state density is equal. This can then be exactly solved by numerical calculations, while terms dealing with exchange of electrons and their correlation are placed within a single term called exchange-correlation functional. The ground state properties of an interacting many-particle system are then exactly determined up to exchange-correlation functional, which is approximated. Therefore, the precision with which the ground state properties of a system are determined highly depends on the accurate approximation to the exchange-correlation functional. With electron density of the non-interacting system being defined as

$$n(\mathbf{r}) = \sum_i |\psi_i(\mathbf{r})|^2, \tag{2.1.4}$$

the so-called Kohn-Sham energy functional is then given by

$$E_{KS}[n(\mathbf{r})] = -\frac{1}{2}\sum_i \int |\nabla\psi_i(\mathbf{r})|^2 d^3r + \frac{1}{2}\int \frac{n(\mathbf{r})n(\mathbf{r}')}{|\mathbf{r}-\mathbf{r}'|} d^3d^3r' + \int V_{ext}(\mathbf{r})n(\mathbf{r})d^3r + E_{xc}[n(\mathbf{r})] + E_{II}, \tag{2.1.5}$$

where the first term is the kinetic energy of the non-interacting electrons, and the second term is the classical Coulomb interaction energy where electron density interacts with itself, and E_{xc} is the exchange-correlation energy functional. The interaction of electron density with itself leads to a so called self-interaction error, which would get corrected with the use of exact correlation functional, but since it is an approximate functional, there is still residual error due to which some of the properties of highly correlated systems get incorrectly approximated. By using exchange-correlation functionals, which are explained in the following chapter, Kohn-Sham equations are solved self-consistently by making an initial guess to the density of the system. From this density, electron wave functions are calculated, from which new density is calculated. By comparing newly obtained density with the initial guess, self-consistency is tested. The self-consistency is reached when the difference in the density obtained in two successive runs is below a certain threshold, depending on the accuracy required for the investigation of properties of a system.

2.1.3 Exchange and correlation approximation

The most basic approximation to the exchange-correlation functional was made by Kohn and Sham in their original paper [36]. In this approximation, solids are considered to be close to the limit of the homogeneous electron gas. Because of this, exchange and correlation effects have local character, and local density approximation (LDA) is therefore obtained as an integral over all space, where exchange-correlation energy for the solid is equal as that of the homogeneous electron gas

$$E_{xc}^{LDA}[n(\mathbf{r})] = \int n(\mathbf{r})\epsilon_{xc}^{heg}[n(\mathbf{r})]d^3r, \tag{2.1.6}$$

where $\epsilon_{xc}^{heg}[n(\mathbf{r})]$ is the exchange-correlation energy of the homogeneous electron gas. This energy can be split into two terms, exchange term and correlation term. While exchange energy per particle for the homogeneous electron gas is exactly known, the correlation energy is not known exactly, and can only be approximated using quantum Monte Carlo calculations.

This approximation to the exchange-correlation functional can be improved by additionally considering the gradient of the density locally in the so-called generalized gradient approximation (GGA). This gives new exchange-correlation functional in the form

$$E_{xc}^{GGA}[n(\mathbf{r})] = \int n(\mathbf{r})\epsilon_{xc}^{heg}[n(\mathbf{r}), \nabla n(\mathbf{r})]d^3r. \tag{2.1.7}$$

Alternative exchange-correlation functionals have been explored over the years, with the most notable being meta-GGA functionals where local kinetic energy is additionally included, and hybrid functionals, which combine exact exchange of the Hartree-Fock theory with exchange-correlation functionals of DFT [37].

2.1.4 Pseudopotentials

Because DFT explicitly only considers valence electrons, core electrons need to somehow be integrated in this theory. This is done by implementing pseudopotentials. The interaction of explicitly considered valence electrons with core electrons and nuclei is replaced with an effective potential, called pseudopotential. This effective potential perfectly mimics the exact wave function behavior beyond certain cutoff radius away from the core, while having smoothed behavior near the core, as can be observed in Figure 2.1. This is implemented in order to simplify the electronic problem, as most of the significant properties of the system are determined from the valence electron properties. Furthermore, this effective potential is considered because near the core, the exact wave function has highly oscillatory nature, where because the wave functions are expressed as a product

of a periodic function and plane wave according to Bloch theorem, a very large number of wave functions would be required to appropriately describe this behavior. Inclusion of pseudopotentials, therefore, simplifies the core electron, and nuclei description.

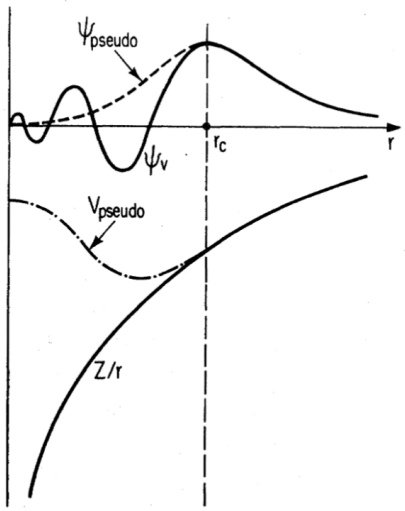

Figure 2.1: *Plot showing the behavior of the pseudo wave function in comparison to the exact wave function, and of pseudopotential compared to the exact potential. Beyond the cutoff radius shown with r_c the pseudopotential and pseudo wave function match exactly. Image taken from reference [38].*

2.1.5 Relaxation of the crystal structure

To find the relaxed positions for atoms in a crystal lattice, a structural relaxation is performed. The optimal structure is the one in which the forces acting on atoms are zero. The forces are calculated from the Hellman-Feynman theorem [39] as

$$\mathbf{F}_I = -\frac{\partial E}{\partial \mathbf{R}_I}. \tag{2.1.8}$$

In the actual implementation of the structural relaxation, several algorithms are typically used. The algorithm used in this work is BFGS algorithm [40], named after Broyden, Fletcher, Goldfarb and Shanno, the developers of the algorithm.

2.1.6 Self-interaction error correction

As in Kohn-Sham theory the Hamiltonian is solved in terms of electron density instead of exact electron positions, within the Coulomb interaction of electrons, there is essentially a problem of interaction of electron density with parts of its own density, or partial interaction of electron with itself. This error should be corrected within exchange-correlation functional, but since this functional is not exact, the so-called self interaction error does not

get corrected exactly. This self-interaction error then leads to unphysical orbital energies leading to a number of errors of incorrectly represented physical properties, especially in the case of highly correlated materials with electrons in d or f orbitals. This error can be corrected in several ways within DFT, such as with the use of Hubbard U parameter, by using hybrid functionals, etc. In our work we chose the correction with Hubbard U parameter, often called DFT+U method, due to its simplicity and low cost. Historically, the value of the Hubbard U parameter has had to be obtained semi-empirically. This way, one has to rely on the existence and accuracy of experimental measurements. As of 2018., there is a model through which the Hubbard U parameters can be obtained from first principles by employing the linear response to external perturbation approach in an efficient manner [41]. Hubbard U parameter which is used to correct a number of poorly approximated properties of the material is obtained self-consistently within this model. The obtained Hubbard U value is then added to energy calculated with DFT.

$$E = E_{DFT} + \frac{1}{2}\sum_{I,\sigma} U^I \mathrm{Tr}[(\mathbf{1} - \mathbf{n}^{I\sigma})\mathbf{n}^{I\sigma}] \tag{2.1.9}$$

where Tr is trace of a matrix (sum over diagonal elements of the matrix), m_1 and m_2 are magnetic quantum numbers of a specific angular momentum, and **n** is occupation matrix defined as projection of Kohn - Sham wavefunctions ψ (which are wavefunctions obtained with DFT) onto localized orbitals φ

$$(\mathbf{n}^{I\sigma})_{m_1 m_2} = \sum_i f_i \langle \psi_{i\sigma} | \varphi^I_{m_2} \rangle \langle \varphi^I_{m_1} | \psi_{i\sigma} \rangle. \tag{2.1.10}$$

The so-called Hubbard projector defined as

$$\hat{P}^I_{m_2 m_1} = |\varphi^I_{m_2}\rangle \langle \varphi^I_{m_1}| \tag{2.1.11}$$

is an important element of this correction method as it defines upon which orbital (manifold) the correction is applied to. The linear response method for obtaining Hubbard U correction was previously derived by Cococcioni and de Gironcoli [42]. This approach has not been heavily used in practice as it required perturbation calculation on a superlattice, leading to a computationally expensive approach. Timrov et al. derived a new approach using monochromatic perturbations. The total response to a perturbation is calculated by summing the responses to monochromatic perturbations in a primitive unit cell.

Although DFT+U method can be applied for both closed-shell and open-shell systems, the use of linear response approach on systems with fully occupied d orbitals, such as for instance ZnO, often leads to very high Hubbard U values [43, 44], or can lead to

numerical instabilities [45, 46]. The details of the DFT+U implementation can be found in the Appendix A.

2.1.7 Dielectric function - optical response

Within DFT, the imaginary part of the dielectric function is treated as a response function. This is achievable if one treats it within the adiabatic perturbation theory. The complex dielectric function can be expressed as

$$\epsilon_{\alpha\beta}(\omega) = 1 + \frac{4\pi e^2}{\Omega N_{\mathbf{k}} m^2} \sum_{n,n'} \sum_{\mathbf{k}} \frac{\hat{\mathbf{M}}_{\alpha,\beta}}{(E_{\mathbf{k},n'} - E_{\mathbf{k},n})^2} \cdots \\ \cdots \left\{ \frac{f(E_{\mathbf{k},n})}{E_{\mathbf{k},n'} - E_{\mathbf{k},n} + \hbar\omega + i\hbar\Gamma} + \frac{f(E_{\mathbf{k},n})}{E_{\mathbf{k},n'} - E_{\mathbf{k},n} - \hbar\omega - i\hbar\Gamma} \right\}, \quad (2.1.12)$$

where Ω is unit cell volume, N_k is the number of k-points, m is electron mass, $f(E_{k.n})$ is the Fermi distribution, Γ is the adiabatic parameter which must tend to zero for total energy conservation, and $\hat{\mathbf{M}}_{\alpha,\beta}$ is the squared matrix element which describes the transition of an electron upon interaction with a photon through the momentum operator from an initial state denoted as n, to a final state n', and then relaxing back from the excited state to state n

$$\hat{\mathbf{M}}_{\alpha,\beta} = \langle u_{\mathbf{k},n'} | \, \hat{p}_\alpha \, | u_{\mathbf{k},n} \rangle \, \langle u_{\mathbf{k},n} | \, \hat{p}^\dagger_\beta \, | u_{\mathbf{k},n'} \rangle \, . \quad (2.1.13)$$

Here, $u_{\mathbf{k},n}$ is the factor of the single particle Bloch functions as obtained in DFT and which are expanded in the plane-wave basis set. Imaginary part of the dielectric function, which is directly related to the absorption, with implementation of a Dirac Delta function δ is then expressed as

$$\epsilon_{2\alpha\beta}(\omega) = \frac{4\pi e^2}{\Omega N_{\mathbf{k}} m^2} \sum_{n,n'} \sum_{\mathbf{k}} \frac{\hat{\mathbf{M}}_{\alpha,\beta} f(E_{\mathbf{k},n)}}{(E_{\mathbf{k},n'} - E_{\mathbf{k},n})^2} \cdots \\ \cdots [\delta(E_{\mathbf{k},n'} - E_{\mathbf{k},n} + \hbar\omega) + \delta(E_{\mathbf{k},n'} - E_{\mathbf{k},n} - \hbar\omega)]. \quad (2.1.14)$$

From the imaginary part of the dielectric function, one can obtain the real part by using the Kramers-Kronig relation

$$\epsilon_{1\alpha\beta}(\omega) = 1 + \frac{2}{\pi} \int_0^\infty \frac{\omega' \epsilon_{2\alpha\beta}(\omega')}{\omega'^2 - \omega^2} d\omega'. \quad (2.1.15)$$

The real and imaginary part of the dielectric function are then further used to calculate

various optical properties [47], such as refractive index

$$n(\omega) = \sqrt{\frac{\sqrt{(\epsilon_1^2(\omega) + \epsilon_2^2(\omega))} + \epsilon_1(\omega)}{2}}, \tag{2.1.16}$$

extinction coefficient,

$$\kappa(\omega) = \sqrt{\frac{\sqrt{(\epsilon_1^2(\omega) + \epsilon_2^2(\omega))} - \epsilon_1(\omega)}{2}}, \tag{2.1.17}$$

reflectivity,

$$R(\omega) = \frac{\left[n(\omega) - 1\right]^2 + \kappa^2(\omega)}{\left[n(\omega) + 1\right]^2 + \kappa^2(\omega)}, \tag{2.1.18}$$

and absorption coefficient

$$\alpha(\omega) = \frac{2\omega}{c}\sqrt{\frac{\sqrt{(\epsilon_1^2(\omega) + \epsilon_2^2(\omega))} - \epsilon_1(\omega)}{2}} = \frac{2\omega}{c}\kappa(\omega). \tag{2.1.19}$$

Dielectric function obtained within random phase approximation (RPA) does not explicitly account for the excitonic effects, which can lead to less accurate results, especially at high frequencies. This effect is especially pronounced for highly correlated insulators with pronounced excitonic effects. Still, it was shown that for semiconductors with moderate band gaps RPA based dielectric function compares well to experimental results, as well as more accurate theoretical results obtained within GW approximation [48]. This suggests that for perovskites studied within this thesis, which have relatively low band gaps, RPA should provide sufficiently accurate results.

2.1.8 Interface electrostatic potential and charge density

In planar architecture of the PSC, the charge transfer is mostly governed by the relative position of the valence and conduction bands of neighboring materials. Due to a non-local nature of the Coulomb interaction, the relative positions of valence band maximum (VBM) and conduction band minimum (CBM) cannot simply be calculated from their bulk positions [49]. Especially in heterovalent interfaces, the relative positions of the band edges highly depend on the interaction of the two surfaces in contact. Therefore, one must conduct simulations of a supercell model to deduct how interface interaction contributes to band offset. The supercell model usually takes the form of a heterostructure with two slabs of different materials surrounded by a slab of vacuum, often called the isolated interface model. To be able to align the energy band edges, a common reference is required. For the band offset calculation the average electrostatic potential is often used

as a common reference. The average electrostatic potential is a sum of the ionic potential and Hartree potential averaged over the direction of the growth of the heterostructure. Electrostatic potential is calculated as a three-dimensional quantity, where to simplify its display it can be averaged over the plane perpendicular to a certain surface. If the plane-averaged electrostatic potential is calculated along z axis, it is obtained from

$$\bar{V}(z) = \frac{1}{S}\int_S V(x,y,z)dxdy. \tag{2.1.20}$$

This can also be applied to the valence electron charge density,

$$\bar{\rho}(z) = \frac{1}{S}\int_S \rho(x,y,z)dxdy. \tag{2.1.21}$$

Atomic oscillations in plane averaged density or potential are generally not of interest. On the other hand, average values over a certain region are often important quantities. The macroscopic average, known from basic electrodynamics, is used for averaging the electrostatic potential or charge density around the heterojunctions, and was introduced into this theory by Baldereschi et al. [50]. For a general plane averaged function

$$\bar{f}(z) = \frac{1}{S}\int_S f(x,y,z)dxdy, \tag{2.1.22}$$

the macroscopic average is calculated as

$$f^{(macro)}(\mathbf{r}) = \int w(\mathbf{r}-\mathbf{r}')f^{(micro)}(\mathbf{r}')d\mathbf{r}', \tag{2.1.23}$$

where w is a filter function which depends on the geometry of the system. If the growth of the heterostructure occurs in z direction, the filter function can be expresed as

$$w(z) = \frac{1}{a}\Theta\left(\frac{a}{2} - |z|\right), \tag{2.1.24}$$

with a being the period over which the macroscopic average is performed, determined by the thickness of the unit cell in the z direction, and Θ being a one dimensional step function. For lattice mismatched systems, the period a is different, where the double macroscopic average technique needs to be performed [51]. This is done by first calculating the macroscopic average over period equal to the unit cell length along the growth of the heterostructure for one material, then for the second. It is typically done using a single filter function

$$\bar{\bar{f}} = \int w_A(\mathbf{r}-\mathbf{r}')w_B(\mathbf{r}')dr'. \tag{2.1.25}$$

This gives out a function which has smooth behavior in the bulk-like region of the slabs,

and shows divergence from the smooth behavior at the interface region.

2.1.9 Band offset calculation

The values of the average potential assumed at the bulk region in both sides of the heterostructure are used for the band offset calculation in the following way

$$VBO = \Delta E_v + \Delta V, \tag{2.1.26}$$

$$CBO = \Delta E_c + \Delta V, \tag{2.1.27}$$

where VBO is the valence band offset, CBO is the conduction band offset, and ΔV is the potential line-up between two bulk regions in a supercell. The ΔE_v and ΔE_c are the terms often referred to as band structure terms, and calculate the difference between the band edges and the average bulk electrostatic potential

$$\Delta E_v = (E_A^{VBM} - \bar{V_A}) - (E_B^{VBM} - \bar{V_B}), \tag{2.1.28}$$

$$\Delta E_c = (E_A^{CBM} - \bar{V_A}) - (E_B^{CBM} - \bar{V_B}). \tag{2.1.29}$$

Here, E_A^{VBM} and E_B^{VBM} are the VBM of material A and B, respectively, E_A^{CBM} and E_B^{CBM} are their CBM, and $\bar{V_A}$ is the average bulk potential of material A, and $\bar{V_B}$ the average bulk potential of material B. Through the band structure term all of the bulk effects are captured, while all of the interface interaction contributions towards the relative band positions are captured within the electrostatic potential of the interface supercell model.

2.2 Effective mass

One of the very important properties governing the charge dynamics is the effective mass. Electron effective mass is directly related with the electron mobility through term

$$\mu_e = \frac{e\tau}{m_e^*}, \tag{2.2.1}$$

where μ_e is electron mobility, e is unit charge, τ is carrier lifetime, and m_e^* is electron effective mass. In the simplest form, effective mass can typically be calculated by approximating the curvature of the Bloch bands, where the curvature of CBM is approximated to calculate electron effective mass. The energy of an electron near the conduction band edge can locally be approximated as [52]

$$E(\mathbf{k}) = E_c + \frac{\hbar^2}{2m_e^*}\mathbf{k}^2, \tag{2.2.2}$$

where E_c is the energy at conduction band edge, $\mathbf{k}$ is wavevector at which the energy is calculated, and m_e^* is effective mass of electron. This term resembles parabola equation

$$y(x) = b + ax^2, \tag{2.2.3}$$

where a and b are constants. Therefore, we can relate constant a of the quadratic term as

$$a = \frac{\hbar^2}{2m_e^*}. \tag{2.2.4}$$

Therefore, by approximating the curvature of the Bloch band with parabola equation, from the leading coefficient of the quadratic term the effective mass of the electrons can be calculated as

$$m_e^* = \frac{\hbar^2}{2a}. \tag{2.2.5}$$

Chapter 3

Bulk perovskites

To distinguish the interface effects in metal oxide/perovskite heterojunction systems, first the properties of bulk systems will be presented, followed by analysis of their interface properties, with the emphasis on the properties governing the charge dynamics.

$CaMnO_3$ perovskite was previously investigated for the role of the buffer layer in the PSC. The high curvature of the CBM, indicative of low effective mass and high electron mobility, highly contributed to the improvement of transport properties over typically used TiO_2 ETL [29]. It was also previously indicated that CMO has good optical properties, such as high absorption coefficient with a prominent peak in the visible part of the spectrum [30]. Due to previously reported good optical properties, as well as a suitable band gap, CMO could be of interest as the absorber layer in PSC. Although the substitution of $A-$site cation does not alter its optical properties significantly, it was proposed that this substitution should be of interest as it could lead to different interaction and bonding properties at the interface with neighbouring ETL.

Therefore, the inorganic manganese perovskites studied within this thesis for the role of PSC optical absorber are $CaMnO_3$, $SrMnO_3$, and $BaMnO_3$. CMO and SMO compounds have a typical cubic perovskite phase at high temperatures, above 900°C and 1400°C respectively, but at room temperature they crystallize in either orthorombic structure (CMO), or 4H hexagonal structure (SMO) [53, 54]. BMO exists in several hexagonal phases at room temperature, with increase in cubic layer characteristics above 1150°C [55]. Hexagonal perovskite phases of BMO are 2H, 4H, and 6H. In this work, 4H perovskite phase of BMO was studied. The orthorombic and hexagonal structures are a result of the distortion of the corner sharing MnO_6 octahedra. The distortions of the MnO_6 octahedra can be seen in the Figure 3.1, where in the case of orthorhombic structure a slight tilt of the octahedra can be observed. For hexagonal structure there is a significant tilt of the octahedra which leads to the formation of the edge-sharing octahedra. The space group of the orthorhombic CMO is $Pnma$, and of hexagonal SMO and BMO $P6_3/mmc$.

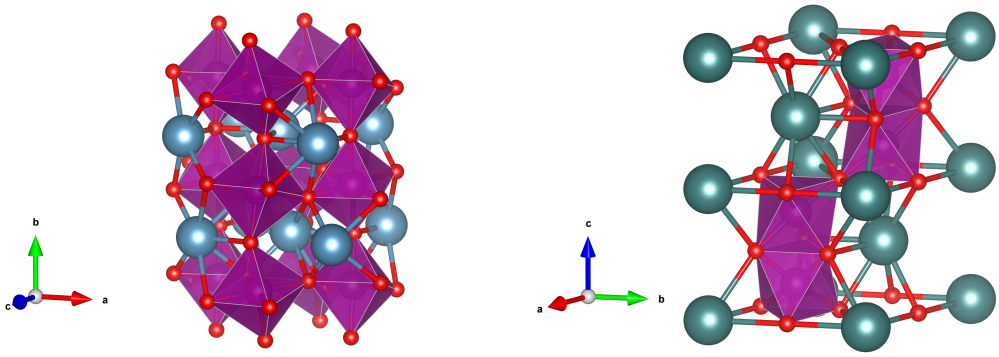

Figure 3.1: *Distortion of the MnO_6 octahedra in orthorombic lattice (left), and hexagonal lattice (right) of manganese perovskites.*

All of the investigated perovskites are antiferomagnetic compounds, with multiple reported spin configurations, but with G-type antiferromagnetic ordering being the most stable [56–58]. They are composed of manganese Mn^{4+} $B-$site cation, oxygen O^{2-} $X-$site anion, and A cation site is occupied by either Ca^{2+}, Sr^{2+} or Ba^{2+}. The substitution of the $A-$site cation affects the bond length of the MnO_6 octahedra, hence changing the overall structure. Because manganese has electrons in 3d orbital, to correctly represent the properties of these systems, the Hubbard U parameter for self-interaction error (SIE) is included. This is especially important for these perovskites as their optoelectronic properties are determined by the MnO_6 octahedra. The following sections, thus, are concerned with the investigation of relevant properties of bulk perovskites of interest. Additionally, bulk perovskites are investigated to asses whether our DFT model predicts their properties accurately compared to previous studies. This is important as these compounds are further used as a basis for the investigation of the properties of the heterojunctions, which are a highlight of this thesis.

3.1 Structural properties

Three investigated perovskites were initially placed in a unit cell according to previously measured lattice parameters and atomic positions. Typical lattices at room temperature for these compounds are shown in Figure 3.2.

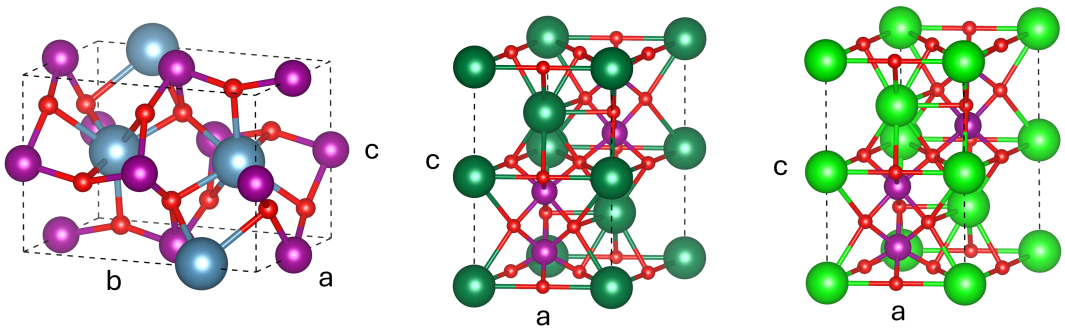

Figure 3.2: *Orthorhombic unit cell of $CaMnO_3$, and hexagonal unit cells of $SrMnO_3$ and $BaMnO_3$.*

Structural relaxation is then performed for lattice parameters and atomic positions. The obtained lattice parameters using both basic DFT and DFT+U are shown in Table 3.1.

Table 3.1: *Lattice parameters of $CaMnO_3$, $SrMnO_3$ and $BaMnO_3$ obtained without and with the use of self interaction error correction via Hubbard U parameter and compared to experimental measurements.*

	$CaMnO_3$			$SrMnO_3$			$BaMnO_3$		
	DFT	DFT+U	EXP [59]	DFT	DFT+U	EXP [60]	DFT	DFT+U	EXP [61]
a (Å)	5.31	5.41	5.28	5.48	5.53	5.45	5.68	5.74	5.64
b (Å)	7.47	7.57	7.45	-	-	-	-	-	-
c (Å)	5.27	5.34	5.26	9.10	9.28	9.09	9.27	9.44	9.22

Basic DFT predicts the lattice parameters which are in better agreement with the experimental measurements. Application of the DFT+U method leads to overestimated lattice parameters for all three systems. This effect was already reported, which is the result of a decrease of Mn-3d and O-2p hybridization due to higher localization of Mn-3d electrons [62]. This leads to reduced bonding effects, which affects the lattice parameters. Nevertheless, even with DFT+U approach, the discrepancy from experimental results for lattice parameters is reasonably low, in general below 2%, with largest discrepancy being 2.46%. The largest discrepancy, calculated for a lattice parameter of CMO, presumably occurs due to the largest Hubbard U value used on Mn-3d states. However, due to values of Hubbard U parameter being nearly the same ($U_{Mn\text{-}3d}$(CMO) = 5.91 eV, $U_{Mn\text{-}3d}$(SMO) = 5.75 eV, $U_{Mn\text{-}3d}$(BMO) = 5.82 eV), the average error in all three compounds is very similar. Although DFT+U predicts lattice parameters less accurately compared to DFT, the inclusion of this correction is crucial for the correct approximation of the band gaps.

3.2 Electronic properties

After the structural relaxations, electronic properties were investigated. For CMO, DFT gives an indirect band gap of 0.80 eV. The inclusion of DFT+U method increases the band gap to 0.92 eV. Despite the used correction, the band gap is still underestimated compared to previous experimental measurements (Table 3.2). The addition of Hubbard U correction for oxygen 2p states would likely lead to improved band gap. However, attempts to include it within linear response approach led to numerical instabilities. Therefore, despite band gap being underestimated, no correction was applied to oxygen 2p states. From Figure 3.3 it can be seen that with both DFT and DFT+U approach the high curvature around Γ point is present. In general the character of the conduction band near the gap is very similar. The included SIE correction, however, leads to higher density of valence states near the forbidden region. This indicates that a large number of electrons are available for optical excitation. Although indirect band gap is observed, in both cases the difference in energy between an indirect and a direct gap at the Γ point is negligible, leading to a conclusion that a large portion of the electrons should undergo a direct non-phonon assisted excitation. In both SMO and BMO, DFT+U approach leads to a reduction in band gap which basic DFT overestimates: 1.88 eV and 1.80 eV, respectively. The DFT+U band gap values, 1.44 eV for SMO, and 1.22 eV for BMO, are in excellent agreement with the experimental measurements (Table 3.2).

Table 3.2: *Optical band gap values of $CaMnO_3$, $SrMnO_3$ and $BaMnO_3$ in electronvolt obtained with reflection-transmission (R,T) measurements and luminescence (Lum) measurements and compared to DFT and DFT+U calculations.*

	Band gap in eV			
	E_g - R,T [31]	E_g - Lum [31]	E_g - DFT	E_g - DFT + U
$CaMnO_3$	1.15	1.23	0.80	0.92
$SrMnO_3$	1.40	1.50	1.88	1.44
$BaMnO_3$	1.30	1.24	1.80	1.22

Basic DFT gives the indirect band gap for both SMO and BMO (Figure 3.3). The band gap character remains the same for SMO, with a shift of VBM from K to Γ point, and shift of CBM from Γ to M. However, similar to CMO case, direct band gap value differs very little from the indirect gap. More pronounced changes occur within the valence bands with respect to the conduction bands in both compounds. High curvature of edge valence state is noticeable, with retained high density deeper within the valence band. The band

structures of SMO and BMO are similar due to the same lattice, and valence electron configuration. The obtained band gap values for two hexagonal systems are ideal for PSC applications, which is also true for previous experimental measurements of the band gap of CMO. This is because according to the Shokley-Queisser limit, this is where optimal power conversion efficiency is achieved. In this range, thermal losses are balanced, as are the losses due to non-absorbed photons of energy lower than band gap value [63].

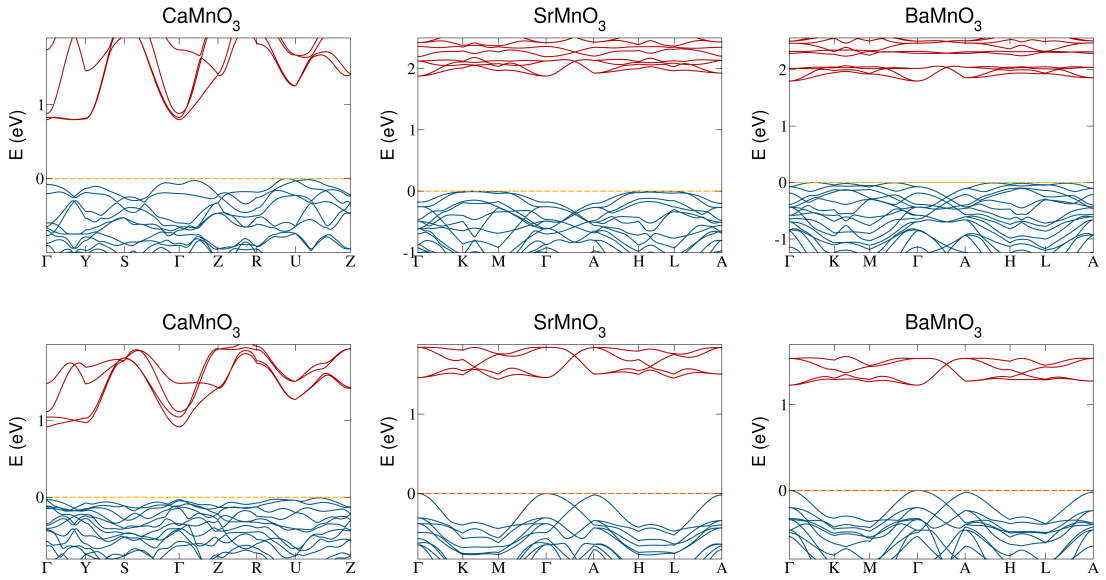

Figure 3.3: *Band structures of $CaMnO_3$, $SrMnO_3$ and $BaMnO_3$ obtained with DFT (top row) and DFT+U (bottom row).*

To further investigate the effect of SIE error correction, total and partial density of states are shown in Figure 3.4 for DFT and DFT+U method. The high dominance of Mn-3d and O-2p states towards total DOS is evident, which is the reason why constituents of the MnO_6 octahedra dictate the optical properties. It is easily seen from Figure 3.4 that summing the contributions of these states gives the total DOS, meaning that other states have little to no contribution at this energy range. For CMO, there is an increase in density of valence states at the top of the band, while opposite is visible in SMO and BMO. In SMO and BMO, due to the high curvature of the edge valence state (Figure 3.3), the very edge of the valence band has lower DOS compared to basic DFT. In general, there is an increase in DOS deeper within the valence band for all three compounds. With DFT+U approach, top of the valence band is highly dominated by oxygen 2p states. This is the result of change in the charge density of manganese 3d electrons, as with DFT+U approach they become more localized within the 3d manifold. There is a slight change at the bottom of the conduction band, visible both in the band structure and in the partial density of states. There is an overall increase in contribution of oxygen 2p states towards

entire conduction band. In terms of partial density of states, nearly identical conclusion can be drawn for all three perovskites. Implementation of the DFT+U approach leads to the dominance of 2p states towards top of the valence bands. For the conduction band, DFT+U predicts a strong hybridization of oxygen 2p and manganese 3d states.

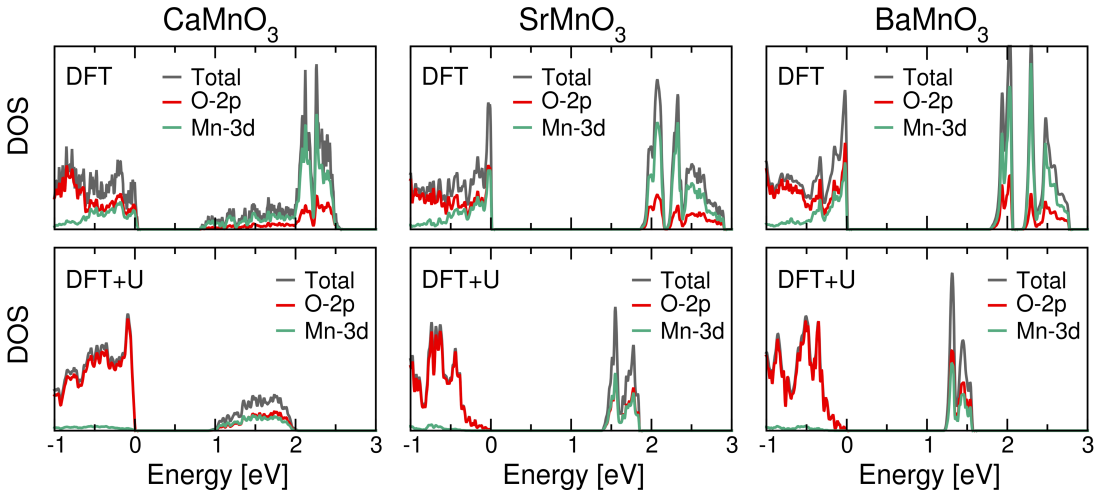

Figure 3.4: *Total and partial density of states of $CaMnO_3$, $SrMnO_3$ and $BaMnO_3$ obtained with DFT (top row) and DFT+U (bottom row).*

3.3 Optical properties

Optical properties are studied through the absorption coefficient, refractive index and reflectivity. For all three perovskites a red shift is observed when Hubbard correction is applied. Due to this red shift, local peaks are observed within the visible part of the absorption spectrum. From the absorption spectrum of CMO, although its band gap is underestimated, it is noticeable that more significant absorption starts beyond 1 eV. Absorption maximum is observed at around 2.3 eV, with a noticeable reduction in absorption at higher energies. CMO shows reflectivity above 30% throughout the majority of the visible spectrum, with a significant drop at higher energies. High reflectivity at lower energies within visible spectrum is undesirable. However, compared to previous theoretical results concerning the reflectivity for CMO [29], they are in excellent agreement. There is generally a good qualitative agreement of absorption coefficient and refractive index with previous work of Zhao et al., where they were experimentally measured [30]. However, at higher frequencies, beyond the visible region, larger deviations from the experimental measurements can be observed. Additionally, in the experimental work two distinct peaks in the absorption spectrum can be observed within visible range, which cannot be found in the theoretical prediction. Nevertheless, the photon energy at which peak emerges

within visible spectrum is very similar to where experimentally measured peaks emerge. Comparison of reflectivity of $CaMnO_3$ with experimental work of Hung et al. [64] reveals generally good qualitative agreement. Theoretical predictions based on DFT+U method, however, overestimate the value of reflectivity, where peak at close to 40% is predicted. Experimental measurements demonstrate that reflectivity of $CaMnO_3$ is below 20%. Furthermore, similarly to other optical constants, deviations of reflectivity from the experimental measurements are found at higher frequencies beyond visible range. For $SrMnO_3$, experimental study on optical properties conducted by Žužić et al. revealed that reflectivity has a nearly constant value below 20% throughout visible range [65]. In comparison, in this work reflectivity is overestimated with a peak at around 2.2 eV where reflectivity is around 30%. Additionally, reflectivity does not show the same constant behavior visible in the experimental measurement. Refractive index also differs compared to the same experimental work, where nearly constant value of the refractive index across the visible range is not reproduced accurately within approach used in this work. There were no further experimental studies where optical properties of the hexagonal perovskites of $SrMnO_3$ and $BaMnO_3$ in 4H phase were studied, up to the authors knowledge. In the papers concerning experimental measurements either polymorphous structures are reported, or different phases than the ones studied in this thesis, making direct comparison impossible due to a difference in the local environment of MnO_6 octahedra for different phases. From PDOS high dominance of O 2p states is predicted towards top of the valence band, while bottom of the conduction band is dominated by both O 2p and Mn 3d states for all studied perovskites. While no definitive conclusions on the nature of optical transitions can be drawn from PDOS displayed in Figure 3.4, it can be expected that main transitions which result in prominent peaks are O 2p to Mn 3d, or O 2p to hybridized p-d orbitals. In the previous work on $CaMnO_3$ it was reported that main transitions are electric dipole (allowed) transitions, from O 2p to e_g [64]. A recent report on $SrMnO_3$ demonstrated that main transitions also occur between O 2p and Mn 3d states. Considering they are allowed electric dipole transitions, they are the main contributors towards prominent absorption peaks [66]. Similar can be expected for $BaMnO_3$.

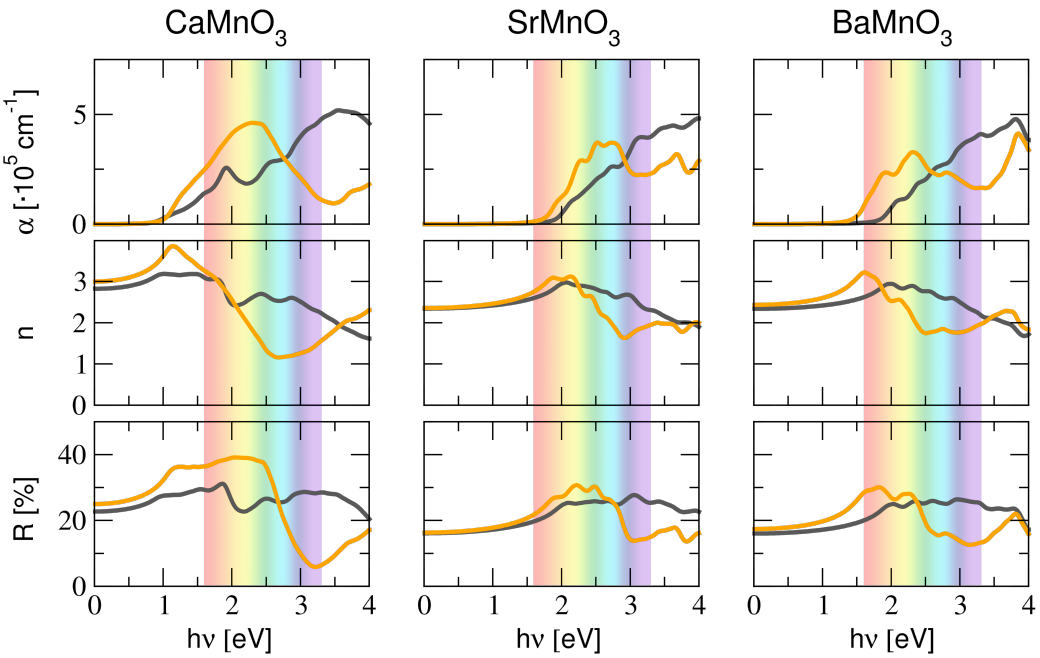

Figure 3.5: *Absorption coefficient α, refractive index n and reflectivity R of $CaMnO_3$, $SrMnO_3$ and $BaMnO_3$. Orange lines represent results obtained with the use of DFT+U approach, and black lines represent basic DFT results.*

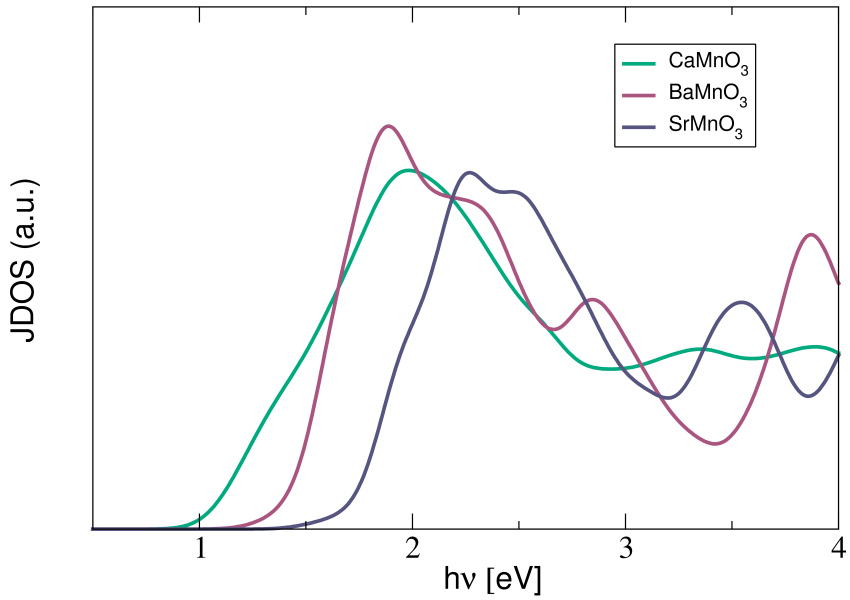

Figure 3.6: *Joint density of states of $CaMnO_3$, $SrMnO_3$ and $BaMnO_3$.*

Refractive indices are relevant for good optical coupling with adjacent layers, in this case ETL. Static refractive index of CMO is 2.98, higher than the indices of the studied metal oxide ETL's, which have static refractive index between around 2.00 to 2.60 [67–70]. Previous theoretical study has found similar behavior of the refractive index of CMO, but with static refractive index between 2.12 and 2.50 [29]. In that study, the value of the refractive index increases to around 3.00, similar to what was calculated in this study. For SMO and BMO, static refractive indices were calculated at 2.36 and 2.43 respectively, showing good optical coupling with studied metal oxide ETL's. High density of valence states near the gap indicates that a large proportion of electrons can participate in the excitation process, which is further confirmed by the joint density of states (JDOS). Figure 3.6 shows that a high number of allowed optical transitions is available for all perovskites in the range from around 1.8 eV to 2.6 eV. In general, the results of investigated optical constants indicate that these materials could be promising candidates as PSC absorber layer.

Chapter 4

Metal oxides as electron transport layers

An important process taking place within the PSC is the charge separation and transport towards the electrodes. This is mainly governed by the band alignment between the perovskite absorber and the surrounding charge transport layers. From the band alignment shown in Figure 1.3, it can be observed that a good transport layer allows only one type of charge carrier to be transported towards respective electrode. In ETL, the band offset with the perovskite should be type II, also called staggered offset, where both VBM and CBM of the metal oxide ETL are lower in energy compared to the perovskite. This enables spontaneous diffusion of excited electrons from the perovskite into the ETL conduction band. It also blocks holes from being transported towards the same electrode, as valence states of ETL are at lower energies than in the perovskite. In typical planar architecture, several metal oxides are commonly used as ETL, due to their large band gap (3.0 eV to 3.6 eV), high transmission of visible radiation, good stability, high electron mobility, and because they do not cause degradation of the perovskite absorber layer. The most commonly used metal oxide ETL is TiO_2. Besides TiO_2, ZnO and SnO_2 are also being frequently used. However, TiO_2 can also cause reduction in PSC performance due to its photocatalytic activity induced by the UV light [71]. SnO_2, compared to TiO_2, requires lower processing temperatures, while also providing good band alignment with most commonly used perovskites, high electron mobility, large band gap, and good stability [72, 73]. ZnO is also a good alternative, having large band gap, high electron mobility, favourable band alignment with commonly used perovskites, and lower processing temperatures than TiO_2. However, ZnO based PSC have generally had lower efficiency compared to SnO_2 and TiO_2 [74]. A recent study has targeted the issues emerging at the interface of ZnO and perovskites that mainly impact the stability, but also affects the efficiency. Autors have highlighted surface chemistry as an important aspect that impacts the relevant factors of the stability and efficiency in ZnO-based PSC, with ammonia-terminated ZnO surfaces showing enhanced stability and efficiency [75].

4.1 Structural properties

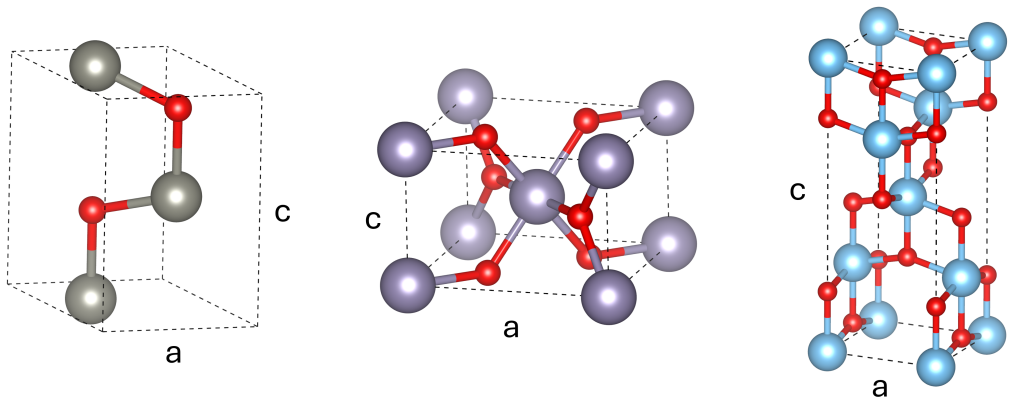

Figure 4.1: *Hexagonal unit cell of ZnO, and tetragonal unit cells of TiO_2 and SnO_2.*

To simulate the properties of metal oxides DFT+U method is also used, since they contain transition metal elements with partially or fully occupied d orbitals. Here, the results with included Hubbard U correction are not compared to uncorrected models. For all three systems the value of the Hubbard U parameter was obtained via semi-empirical approach, where the parameter value which gives the best band gap value is chosen. Details on the Hubbard U parameter calculation can be found in the Appendix A.

Table 4.1: *Lattice parameters and band gaps of ZnO, SnO_2 and TiO_2 obtained without and with the use of self interaction error correction via Hubbard U parameter and compared to experimental measurements.*

	ZnO		SnO_2		TiO_2	
	DFT+U	EXP	DFT+U	EXP	DFT+U	EXP
a (Å)	3.25	3.25[76]	4.76	4.78[77]	3.81	3.79 [78]
c (Å)	5.20	5.21[76]	3.19	3.19[77]	9.87	9.52[78]
E_g (eV)	3.47	3.41[79]	3.65	3.60[80]	3.13	3.20[81]

The lattice parameters obtained with DFT+U approach are shown in Table 4.1 and compared to previous experimental measurements. Very good agreement is obtained for ZnO and SnO_2 lattice parameters. The a lattice parameter of TiO_2 is in excellent agreement with experimental results, with larger discrepancy of around 3.6% for c parameter. This effect was previously observed for TiO_2 in the study by Dong et al. [82], where discrepancy in

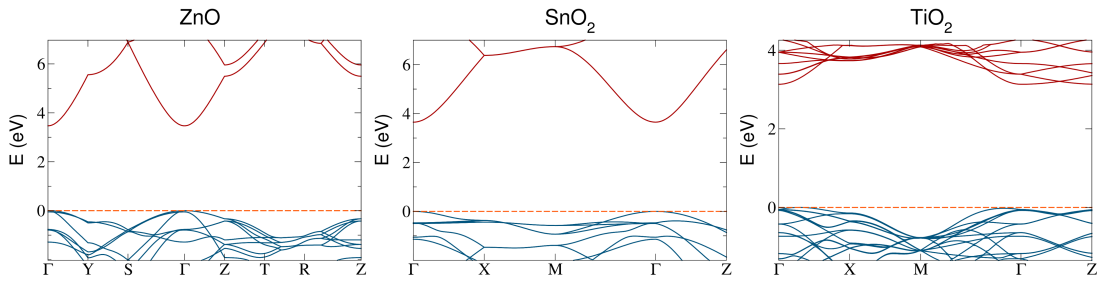

Figure 4.2: *Band structures of ZnO, SnO_2 and TiO_2.*

lattice parameters was increased with the increase of Hubbard U value, which is required for correct approximation of the band gap.

4.2 Electronic properties

Band structures of studied metal oxides are shown in Figure 4.2. For all three metal oxides DFT+U approach gives band gaps larger than 3 eV, in excellent agreement with experimental measurements (Table 4.1). Displayed band structures additionally show high curvature of the conduction band edges for all three metal oxides, characteristic for these materials, which hints at high electron mobility due to low effective mass of electrons. Effective mass of electrons of these materials will be analysed in more detail in the following sections.

Chapter 5

Heterostructures

In heterovalent interfaces, the relative band alignment critically depends on the interaction between two surfaces in contact. One of the main goals of this thesis is to infer as much as possible information about the interactions at perovskite/metal oxide interfaces. To gain information on band offsets between two semiconductors, supercell models were generated. For this, pseudomorphic growth of the manganese perovskites on metal oxide ETL was assumed. This means that in the vicinity of the interface the perovskites were strained to accomodate for the difference in the lattice parameters with the neighboring metal oxide ETL. Because large lattice mismatch often leads to a large number of dislocation defects, it is an important factor to consider in the heterostructure models. To assist the stability of the interface and low density of defects, it is desirable to have a small lattice mismatch [19]. Furthermore, simply putting two individually stable surfaces does not ensure stability of the interface, as interface stability depends on the chemical composition of the two surfaces in contact, which in turn depends on the surface orientation and surface termination [20]. A study of $BiOIO_3$(010)/(100) interface has shown that by choosing the most stable surface terminations, the band offset did not match experimental observations. On contrary, to obtain results which are in line with experiments, a less stable (010) surface termination had to be selected, and joined with the most stable (100) surface termination. This interface arrangement led to the formation of chemical bonds at the interface, showing thermodynamic stability of the interface with significant charge transfer [83]. Therefore, for the interfaces considered in this work, the surface orientation was determined based on the minimal lattice mismatch condition. Heterostructures for PSC applications with larger lattice mismatch can also bee considered, as they have been, for example, in a study by Sultana et al. [84], but one has to keep in mind that it could lead to the formation of defects and structural instabilities. Further, in the direction of the growth of the heterostructure, the supercell needs to have sufficient number of atomic layers so that far away from the interface periodic behavior is recovered which is not affected

by the presence of the interface. Typically, interface effects are present only within the first few atomic layers away from the interface, while deeper into the slab the bulk-like behavior is restored. That means that the relevant properties, such as band offset, can be studied in supercells formed by joining two materials composed of several unit cells [49]. Supercell models can be created in two ways:

- as an alternating model, where several unit cell thick slabs of two materials are periodically repeated,
- as an isolated interface, where two slabs are joined together, and their outer surfaces are separated by a sufficiently thick layer of vacuum so that the interaction between the outer surfaces does not significantly affect the total energy of the supercell.

In this work the isolated interface model was used, where the thickness of the vacuum was tested for convergence. This means that the thickness of the vacuum was chosen based on the condition that the interaction of the outer surfaces has negligible effect on the total energy of the system. The convergence of the vacuum layer thickness is covered in the Appendix A. This model, however, introduces some undesirable effects, such as dangling bonds, which can lead to the formation of mid-gap localized states in the band structure. Because studied materials belong to different lattice systems, some of them needed to undergo a coordinate transformation. As two of the metal oxides are tetragonal lattice systems, the easiest way to join those metal oxides with hexagonal lattice perovskites is by redefining the hexagonal lattice systems in an orthorhombic basis. This does not change the physics or the chemistry of those systems. It is merely a change of the coordinate basis, or in other words, change of the frame of reference. Then, strain is introduced to compensate for the lattice mismatch. Because of the large lattice mismatch between ZnO and BMO/SMO hexagonal lattice parameter a, they were all redefined in the orthorhombic basis to comply with the low lattice mismatch condition. Additionally, due to large lattice mismatch between TiO_2 a lattice constant with all investigated perovskites, TiO_2 was rotated around z axis by $45°$, making its x-y plane diagonal the "new" a lattice parameter. The lattice parameters which were used for heterostructure supercell models are listed in Table 5.1. Rearrangement of hexagonal systems into orthorhombic lattice, and rotation of TiO_2 led to lattice mismatches below 4% in most cases, which can be seen in Table 5.2. Conversion of SMO, BMO and ZnO into orthorhombic lattice is represented schematically in Figure 5.1. The conversion also included rightward shift of the unit cell in SMO and BMO case, setting oxygen anions at the corners. This was done because metal oxides mostly contain transition metal cations at the corners of their cells, which should ensure interaction of oppositely charged ions at their interface with the perovskites.

Table 5.1: *Lattice parameters used for generation of the supercell heterostructure models. All hexagonal lattices are converted to orthorhombic lattice, and TiO_2 is rotated $45°$ around z-axis, making its diagonal the new a lattice parameter.*

	ZnO^{ortho}	SnO_2	TiO_2	$CaMnO_3$	$SrMnO_3{}^{ortho}$	$BaMnO_3{}^{ortho}$
a (Å)	5.63	4.76	5.36	5.41	5.53	5.74
b (Å)	3.25	-	-	7.57	9.57	9.94
c (Å)	5.20	3.19	9.86	5.34	9.28	9.44

Because in most cases low strain is imposed on the perovskite, no large changes of out-of-plane lattice parameter in the perovskite should occur. This was further tested on bulk strained models, where only out-of-plane parameter was alowed to relax, with in-plane lattice parameters fixed to the values imposed by the metal oxide substrate. In general, very small change of out-of-plane lattice parameter was observed, between 0.01 Å and 0.08 Å. The exception is CMO conformed to SnO_2, for which very large change was observed. Due to very large biaxial compressive strain on CMO conformed to SnO_2 lattice, a significant expansion of the out-of-plane lattice parameter of CMO is predicted, from 7.57 Å to 10.42 Å. Because of this, for CMO heterostructure with SnO_2, the out-of-plane lattice parameter of CMO in the heterostructure was set at its expanded value, while for other heterostructures the perovskite out-of-plane lattice parameter was initially set to their bulk value. Furthermore, for supercell of this size, the out-of-plane lattice parameter cannot be defined very precisely as in the bulk case, since the interface interaction can affect interlayer distance in the vicinity of the interface. Only for sufficiently large supercells would out-of-plane lattice parameters eventually relax to their true value. For optimal lattice matching, in several cases ETL slab needed to be formed by stacking several unit cells in certain directions. For instance, heterostructures of ZnO with SMO and BMO contain three unit cells of ZnO stacked in y direction, where b lattice parameter becomes 9.75 Å, ensuring excellent matching with b lattice parameters of SMO and BMO of 9.54 Å, and 9.95 Å, respectively. Similarly, to ensure good matching with both b and c lattice parameters of SMO and BMO, SnO_2 slab contained two unit cells in both x and y directions. SMO and BMO were then rotated to join their (010) surface with (001) surface of SnO_2. Using double unit cells of SnO_2 in both x and y direction gave lattice parameter of 9.52 Å in the tetragonal supercell, leading to a low mismatch with lattice parameters of SMO and BMO.

Table 5.2: *Difference in lattice parameters for selected surface orientations of studied heterostructures.*

	$CaMnO_3$	$SrMnO_3$	$BaMnO_3$
ZnO	3.9%, -2.7%	1.8%, 1.8%	-1.9%, -1.9%
SnO_2	-13.7%, -12.2%	2.5%, -0.5%	-4.4%, 0.8%
TiO_2	-0.9%, 0.4%	-3.1%, 2.9%	-7.1%, -0.8%

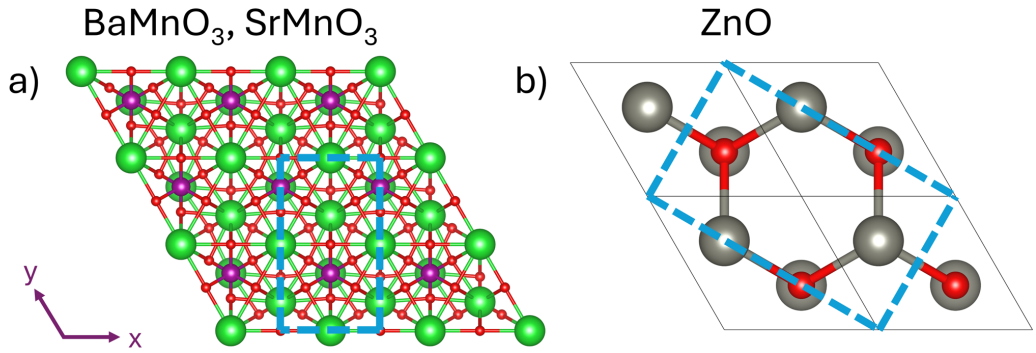

Figure 5.1: *Conversion of hexagonal lattice into orthorhombic for a) $SrMnO_3$ and $BaMnO_3$, and b) ZnO. Blue rectangle displays edges of the orthorhombic lattice.*

Regarding the surface terminations of perovskites, terminations with mixed anion-cation compositions were chosen, for better coupling with metal oxides, as all used metal oxides in considered directions have mixed composition. Only for wurtzite ZnO that could not be achieved with the (001) surface orientation, as it has only two possible terminations in that direction, either Zn or O termination, which are both polar. However, this orientation was only used in ZnO heterostructure with SMO and BMO. For these heterostructures Zn termination was selected, because SMO and BMO contain the same number of oxygen anions as the number of Zn cations at ZnO (001) surface. Other possible surface termination of SMO and BMO in (001) direction is Mn termination, which is also polar. If the ZnO/SMO and ZnO/BMO interface was formed with oxygen terminated ZnO surface and manganese terminated SMO and BMO surface, strong electrostatic interaction could be expected. However, due to the mismatch in the number of oppositely charged ions at those two surfaces and complex mixed ionic-covalent bond that these compounds have, it is difficult to predict whether this type of interface would be more stable than the interface arrangement that was studied. Additional investigation of this interface formation would provide answers, but due to high computational cost that interface configuration

was not considered. For TiO_2 heterostructure, SMO and BMO (001) orientation was also selected, with barium/strontium and oxygen termination, as the only other option was, again, manganese termination. In (010) direction, SMO and BMO have two possible terminations. Mixed termination, composed of all constituents (A, B and X), and oxygen only termination. The oxygen only termination would likely not make a stable interface with SnO_2, because the interface would be over saturated with anions. CMO has two possible terminations in (010) direction, MnO_2 and CaO termination. Previous reports on the stability of these terminations are contradictory [85, 86]. Because the chosen surfaces of metal oxides are always formed by both transition metal cations and oxygen anions (for CMO-based heterostructures), MnO_2 terminated CMO surface was considered as the better choice, as it enables oxygen-transition metal bonding at the interface.

Because of the strain imposed on the perovskites, in the vicinity of the interface their electronic properties might undergo changes. This highly depends on the type and magnitude of strain. Next section is dedicated to the investigation of changes in the electronic properties of the perovskites under induced strain. This is also very important as the strain can affect the position of VBM and CBM with respect to the average potential, hence affecting the band offset.

5.1 Strained perovskites

Inducing strain on the perovskites changes the overlap of atomic orbitals and the periodic crystal potential. This induces changes in the electronic structure. The effect depends on how large the lattice mismatch is, and whether the strain is compressive or tensile. Because in most cases the lattice mismatch is small, the strain caused by the lattice mismatch will presumably not induce significant changes in the electronic structure. Nevertheless, those changes are important to consider even for low strain, due to the contribution to effective mass and band offset.

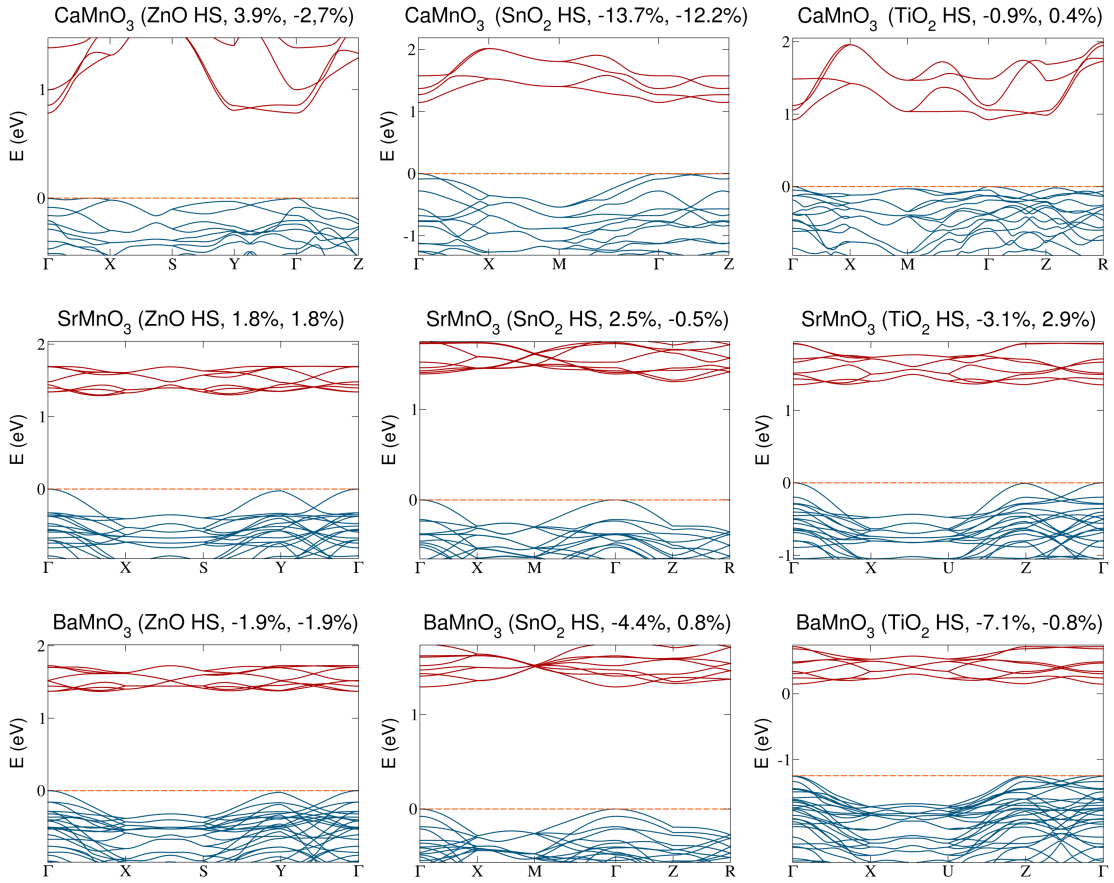

Figure 5.2: *Band structures of manganese perovskites under strain. Metal oxides and induced strains are given in the parentheses.*

Figure 5.2 displays band structures of the strained perovskites. For CMO, under smaller strain, high curvature of the conduction bands is retained. When high compressive strain is induced, conduction bands flatten noticeably. A decrease of the band gap to 0.78 eV for predominantly tensile strain is visible, as well as an increase of the band gap to around 1.15 eV for large compressive strain. For CMO strained over TiO_2 lattice, the band gap is nearly identical to the band gap of bulk CMO, as expected for low imposed strain.

In SMO and BMO even with small imposed strain, flattening of the conduction bands can be seen. Changes also occur within the valence band, but high density of valence states is retained. In SMO, both conformed to ZnO and SnO_2, a reduction of the band gap is observed due to tensile strain, calculated at 1.29 eV and 1.31 eV, respectively. For SMO conformed to TiO_2 lattice, despite more balanced strain with slight dominance of compressive component, the band gap is reduced to 1.35 eV. On BMO, compressive strain was imposed, leading to an increase of the band gap: it is 1.37 eV when conformed to ZnO, 1.29 eV when conformed to SnO_2, and 1.39 eV for BMO strained over TiO_2 lattice. Among strained CMO structures, the position of VBM is the lowest for CMO conformed

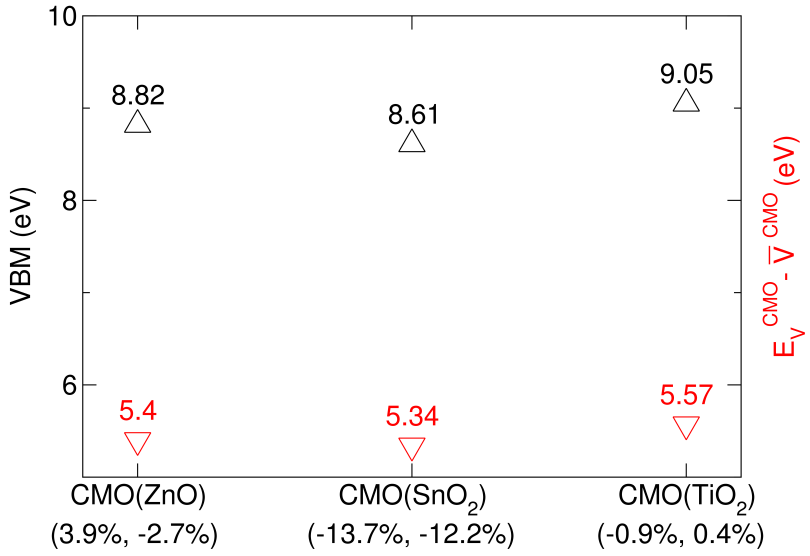

Figure 5.3: *Valence band maximum position and difference between valence band maximum and average potential for strained $CaMnO_3$.*

to SnO_2, facilitated by the large expansion of the unit cell in z direction (Figure 5.3), and is lower than VBM for non-strained CMO (9.00 eV). For band offset, the change in the difference between VBM and the average potential is even more significant. Figure 5.3 shows similar differences between VBM and average potential for all CMO structures, despite differences in strain. In CMO conformed to ZnO and TiO_2, this is due to low and fairly balanced strain (very similar magnitude of tensile and compressive strain in two different directions). In CMO conformed to SnO_2, this is due to previously mentioned large expansion of the lattice parameter perpendicular to the interface. In general, band edge positions are more impacted by the strain than the average potential. This is because the strain mostly affects the average potential through expansion or contraction of the lattice parameter perpendicular to the interface, as it affects interlayer distance. On the other hand, positions of VBM and CBM are affected through the change in the bond length and bond angle of the MnO_6 octahedra, which change due to the difference in orbital overlap under different strain conditions.

Figure 5.4 shows that the positions of VBM in SMO are lowered compared to non-strained SMO when tensile strain is introduced (bulk non-strained VBM position is at 9.42 eV). SMO conformed to TiO_2 is closest to the non-strained SMO in terms of VBM position, which is due to fairly balanced compressive and tensile strain magnitudes. This enables much of the induced biaxial strain to be relaxed without significant change in the lattice parameter perpendicular to the interface. When SMO is conformed to ZnO lattice, the

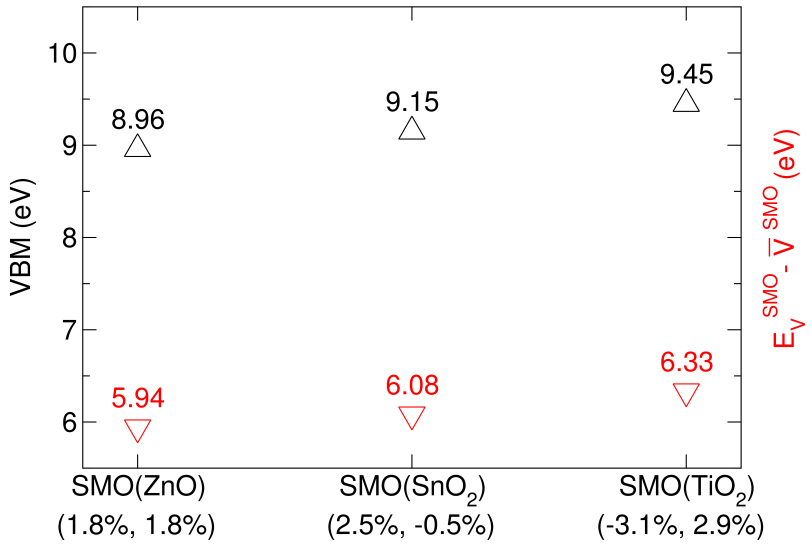

Figure 5.4: *Valence band maximum position and difference between valence band maximum and average potential for strained $SrMnO_3$. Lattice mismatch percentages are given in the parentheses.*

most noticeable shift of VBM occurs under uniform biaxial strain, while nearly uniaxial strain on SMO conformed to SnO_2 lattice produces lower VBM shift, as expected. Band structures and average potentials were calculated on models where the lattice parameter perpendicular to the interface was not relaxed, except for the case of CMO conformed to SnO_2. Because of that, the strain produces less pronounced change in the average potential compared to change which was induced on VBM positions. The reasons this approach was taken will be further explained in the following sections. While VBM did slightly shift upon strain relaxation, as well as the position of average potential, the difference between VBM and average potential changed very little between non-strain relaxed and strain relaxed case. While this can affect the relative positions of VBM and CBM, it will further be revealed why this approach was considered as reasonable.

For strained BMO, the largest change in VBM position compared to non-strained VBM (9.60 eV) is found when it is conformed to TiO_2 lattice, causing a VBM shift of around 1 eV, while the shift of around 0.4 eV to 0.5 eV occurs in other two cases. Because the VBM position for BMO conformed to ZnO and SnO_2 is nearly the same, the difference between VBM and average potential is nearly identical. For BMO conformed to TiO_2 this difference is slightly larger. For BMO, two different strain conditions (for ZnO lattice and and SnO_2), produce less noticeable changes in VBM position compared to similar case in SMO. Furthermore, for both SMO and BMO conformed to SnO_2 lattice strain is more pronounced along a single axis, but the uniaxial strain is of larger magnitude for BMO.

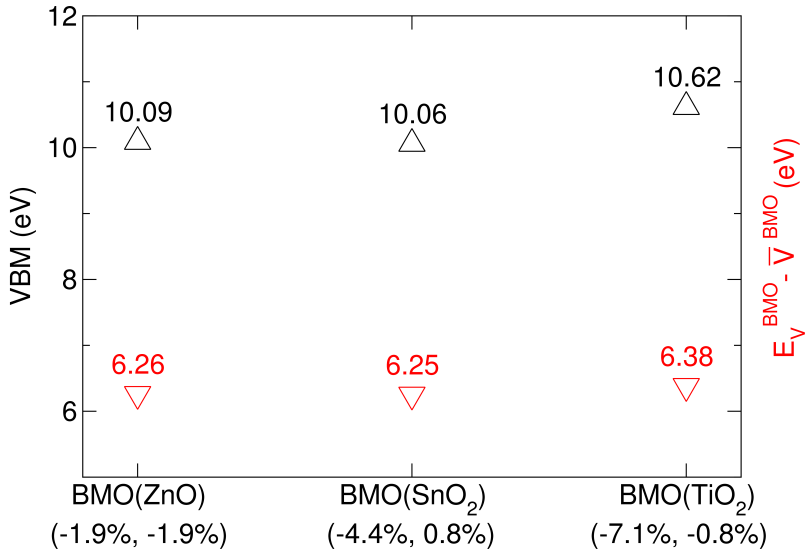

Figure 5.5: *Valence band maximum position and difference between valence band maximum and average potential for strained $BaMnO_3$.*

This indicates that SMO undergoes more significant changes at the top of the valence band compared to BMO, and is likely more prone to structural deformations than BMO. It is also possible that tensile strain produces larger changes in the valence bands than compressive strain of similar magnitude.

For the strained perovskites the optical properties were not investigated because the strained layer is not very thick, and perovskites regain their bulk properties far from the interface. However, even if the perovskites retain the strained structure, the strained perovskites band gaps are all in the desirable range for optical absorption, and their band structures still indicate high density of valence states, indicative of high JDOS at nearly the same energy range as in the non-strained bulk configuration. This means that for the most part, their optical properties are not negatively impacted by the imposed strain.

5.2 Structural properties of the heterostructures

Because some of the heterostructures contain large number of atoms, the generation and relaxation of the heterostructure models had to be conducted in several steps. To reach the relaxed structure, the first step included the formation of the supercell model with one unit cell of metal oxide and one unit cell of the perovskite. Their periodic images are separated by a sufficiently thick vacuum slab. Interface distance in all heterostructures was set to 2 Å. To prevent surface reconstruction, the atomic layers at the outer slab surfaces were fixed. After the relaxation was conducted, additional unit cell was added to both

sides. This formed a heterostructure model composed of two unit cells of metal oxide, and two unit cells of perovskite. For this model, the outer surface layers were also fixed. The final supercell models contained three unit cells of both slabs. To relax the slab with three unit cells, the individual two unit cell slabs were isolated with previously relaxed atomic coordinates. To ensure smooth transition from the interface region to the bulk-like region, the added third unit cell needed to be relaxed to smoothly join with the two-unit cell slab. As interface effects have already been considered, the interface unit cell of each slab had fixed atomic positions. The rest of the atoms, except for the outer surface layer atoms, were allowed to fully relax their positions. This way, interface effects are included, bulk-like region has smooth behavior, and surface reconstruction does not take place. Surface reconstruction is undesirable, as it would introduce difficulties, such as the distortion of the structure towards the outer edge, leaving limited room for bulk-like structure to develop. Figure 5.6 shows the initial heterostructure configurations and the relaxed structures. For CMO heterostructures, no major changes occur within CMO slab for low strained cases (ZnO and TiO_2 heterostructures). What can be seen in those cases is a very subtle displacement of oxygen anions in the interface atomic layer of CMO. In ZnO/CMO heterostructure the interface effects are only visible in the boundary layers at the interface, with barely noticeable changes at the next atomic layer in each slab. Deeper within the slab on each side both materials retain their bulk-like structure, which is expected for ZnO due to no imposed strain, but could also be expected in CMO because of simultaneous tensile and compressive strain of similar magnitudes. In TiO_2/CMO the small strain on CMO causes no visible changes within the slab. To form oxygen-transition metal bonds at the interface, oxygen ions displace. Due to MnO_2 layer symmetry, two oxygen ions of TiO_2 layer move down, and two oxygen ions on the right side of TiO_2 interface layer only slightly displace, likely to form a bond with manganese ion shown in the middle of the MnO_2 interface layer in Figure 5.6. Because of the increased distance between two oxygen ions of TiO_2 interface layer to any of the manganese interface ions, it is unlikely they were able to form bonds. Also visible is the shift of entire CMO slab to the left, with most noticeable shift at the close to the interface. Only minor changes were observed within second atomic layers in both slabs, and regain of bulk-like behavior deeper within each slab. In SnO_2/CMO heterostructure more pronounced changes are visible at the interface, although not very significant apart from a displacement of oxygen ions in MnO_2 interface layer away from the atomic layer center. What is more evident is the change within the perovskite due to high strain. Large expansion of CMO along the direction of the growth of the heterostructure caused substantial atomic layer rearrangement, disrupting the symmetry.

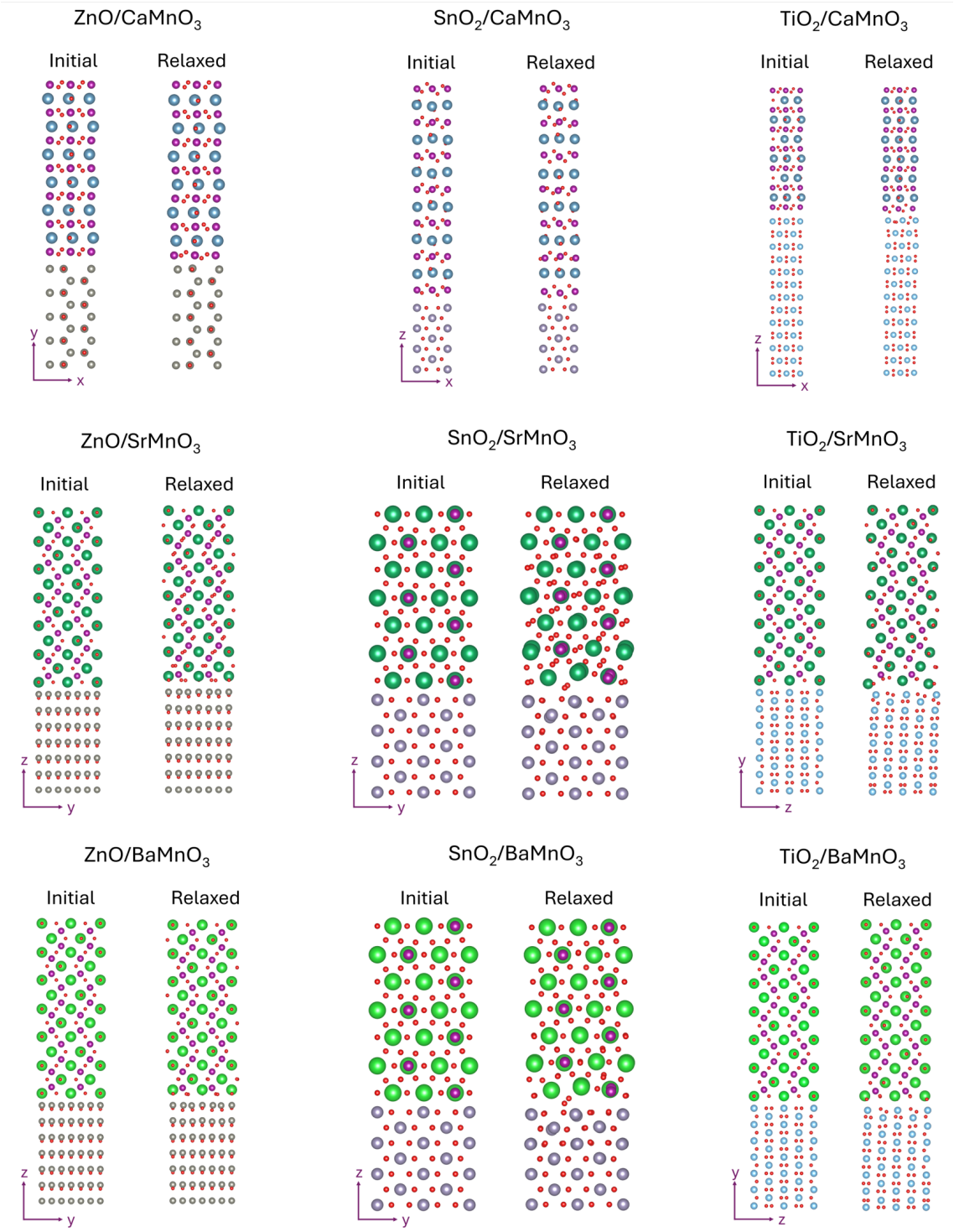

Figure 5.6: *Starting configurations for the nine heterostructures and configurations after structural relaxation. To distinguish between different ions, they are colored as follows:* ● *oxygen,* ● *calcium,* ● *strontium,* ● *barium,* ● *manganese,* ● *zinc,* ● *tin, and* ● *titanium.*

In the heterostructure form the lattice parameter perpendicular to the interface in relatively small supercells, such as these, is not as well defined as it would be for much larger supercells. The average of the lattice parameter which is perpendicular to the interface was closer to their bulk values then to the values obtained under strain relaxation. The exception is CMO conformed to SnO_2 for which this lattice parameter was initially set to the expanded value.

In SMO and BMO, again, due to many similarities, very similar changes occur upon structural relaxation. In their heterostructure with ZnO, the number of zinc ions in the zinc terminated surface is the same as the number of oxygen anions in the boundary layer of the perovskites. This leads to the displacement of oxygen anions towards the interface (Figure 5.6), while barium/strontium cations displace towards the manganese atomic layer. How this affects the charge density and bonding at the interface will be further analyzed later. Similar displacements occur in SMO and BMO heterostructure with SnO_2. Due to the position of strontium/barium cation with respect to the middle tin cation, strontium/barium atoms displace upward, and perovskite boundary oxygen anions displace toward the interface to balance the interface charge density. A single oxygen ion of SnO_2 displaced to the middle of the interface to bond with manganese and strontium/barium, with more pronounced displacement in SnO_2/SMO heterostructure. In TiO_2 heterostructures, most noticeable is the oxygen displacement at both sides of the interface. Again, more severe changes occur at TiO_2/SMO interface than for BMO. Most notably, a much more significant shift of oxygen from SMO interface layer occurs. This is visible from the shift of oxygen with respect to edge strontium cations, which is much more pronounced than shift of edge oxygen at BMO interface layer. Additionally, the two inner oxygen cations from the interface layer slightly move upward towards manganese in BMO, but displace significantly more in SMO. It appears as the interface interaction of TiO_2 with SMO causes a noticeable tilt of TiO_2 slab. This tilt is occurs close to the interface in BMO heterostructure, but not nearly significant as in SMO heterostructure. TiO_2/BMO heterostructure shows boundary layer oxygen displacements on both sides of the interface. While two corner oxygen ions from BMO boundary layer move towards the interface, two middle oxygen ions move toward BMO slab, reducing the bond length with manganese. This likely occurs due to increase of bond length of manganese with corner oxygen ions, which moved toward the interface to form bonds with corner titanium. Periodic arrangement is restored from third atomic layer away from the interface in both slabs. Due to the arrangement of TiO_2 and SMO and BMO surfaces, there is several ions that were unable to form interface bonds. Again, larger changes within the perovskite slab are visible in SMO compared to BMO in their heterostructure with TiO_2, despite larger strain being imposed on BMO. As the strain on SMO in this case is predominantly

compressive, the larger changes within the slab can no longer be assumed to result from the difference in strain type. In SMO and BMO heterostructures with all studied metal oxides, a more pronounced change within SMO slab can be observed compared to BMO slab. While BMO retains bulk-like atomic positions deeper within the slab, SMO undergoes noticeable changes. This can be attributed to larger displacement of interface ions in the y direction in SMO heterostructures compared to BMO. SMO, additionally, has lower bulk modulus, which also impacts the changes it undergoes under strain [87, 88]. The observed structural changes in SMO are in line with previously larger observed changes in VBM position in SMO compared to BMO with similar strain magnitude. Nevertheless, the new atomic arrangement assumed upon relaxation further repeats within the slab of SMO in a periodic manner, showing that the imposed strain and interface interaction leads to the change of symmetry within SMO slab. In the following sections electronic properties are going to be correlated to the structural changes upon interface interaction.

5.3 Electronic properties

5.3.1 Charge density

To analyse the changes in the electronic properties induced by the interface interaction, valence electron charge density is first investigated. Figure 5.7 shows that for all three CMO heterostructures changes of the interface MnO_2 layer charge density mostly occurs due to the displacement of oxygen ions from the atomic layer, which is centered on manganese cations. In ZnO/CMO heterostructure this effect is almost non-existent. This results in a charge density peak of the same height as deeper within CMO slab. Charge density peaks are also consistent throughout the ZnO slab, as well as at the interface. More pronounced changes occur in TiO_2/CMO heterostructure. The displacement of oxygen of MnO_2 lowers the density peak of the interface atomic layer, while the changes at TiO_2 interface layer produced by the interaction with CMO surface increase the density peak. This is due to the composition of MnO_2 atomic layer, which has two oxygen ions below and two above manganese atom. Due to the proximity of two MnO_2 oxygen ions to TiO_2 oxygen, TiO_2 oxygen ions shifted downward, increasing the charge density of the interface layer of TiO_2. In SnO_2/CMO heterostructure, charge density of the interface MnO_2 layer decreased as two oxygen ions moved further away from the atomic layer centered at manganese cation. Changes also occur in the SnO_2 interface atomic layer, mainly due to the change in the interlayer distance between two atomic layers closest to the interface. Also visible is the inconsistency of charge density across CMO slab, which is a result of structural changes caused by large imposed strain. In TiO_2/CMO, MnO_2 layer oxygen displacement lowered the plane-averaged charge density peak, and lowered the interlayer distance between MnO_2

and CaO layers, evident from the reduction of the value of the local minimum between those two layers.

Figure 5.7 further shows similar charge density plots for SMO and BMO based heterostructures. In their heterostructure with ZnO, interface layer of mixed anion-cation composition demonstrates changes in the charge density. Oxygen ions displace towards the interface, and the remaining cation-only atomic layer displaces towards the perovskite slab. Changes are restricted to two atomic layers closest to the interface. Because interface layer barium/strontium ions shift deeper towards the middle of the perovskite slab, the charge density of the second atomic layer away from the interface increases. This is because of increased proximity of large cations (barium/strontium) to smaller manganese cations, or in other words, due to reduction of interlayer distance between barium/strontium and manganese atomic layers. In ZnO, reduction of the second charge density peak away from the interface is visible, which was affected by a small displacement of several zinc ions. In SnO_2 heterostructures with SMO and BMO, the lowering of the interface layer charge density peaks also comes from the displacements of oxygen ions at both surfaces. However, this was not as pronounced as in ZnO heterostructures. Additionally, a single oxygen ion of SnO_2 displaced significantly as it moved into the middle of the interface, which lowered the charge density peak of SnO_2 interface atomic layer. Further into the slabs the periodic bulk-like behavior is restored beyond second atomic layer away from the interface, visible from the constant value of the macroscopic average of the charge density. In TiO_2/BMO significant changes were observed in charge density around the interface (Figure 5.7). The shift of several oxygen ions towards manganese atomic layer increased the charge density at that area, and reduced charge density of the interface atomic layer. Similarly, ionic displacements of first two atomic layers of TiO_2 closest to the interface caused significant changes in the charge density. Further away in both slabs macroscopic averaged charge density settled at a constant value, demonstrating bulk-like behavior in the middle of each slab. In TiO_2/SMO charge density at the interface displays large differences compared to charge density deeper within each slab, facilitated by the larger changes of interface surfaces compared to BMO case. Further beyond second atomic layer periodic behavior is restored.

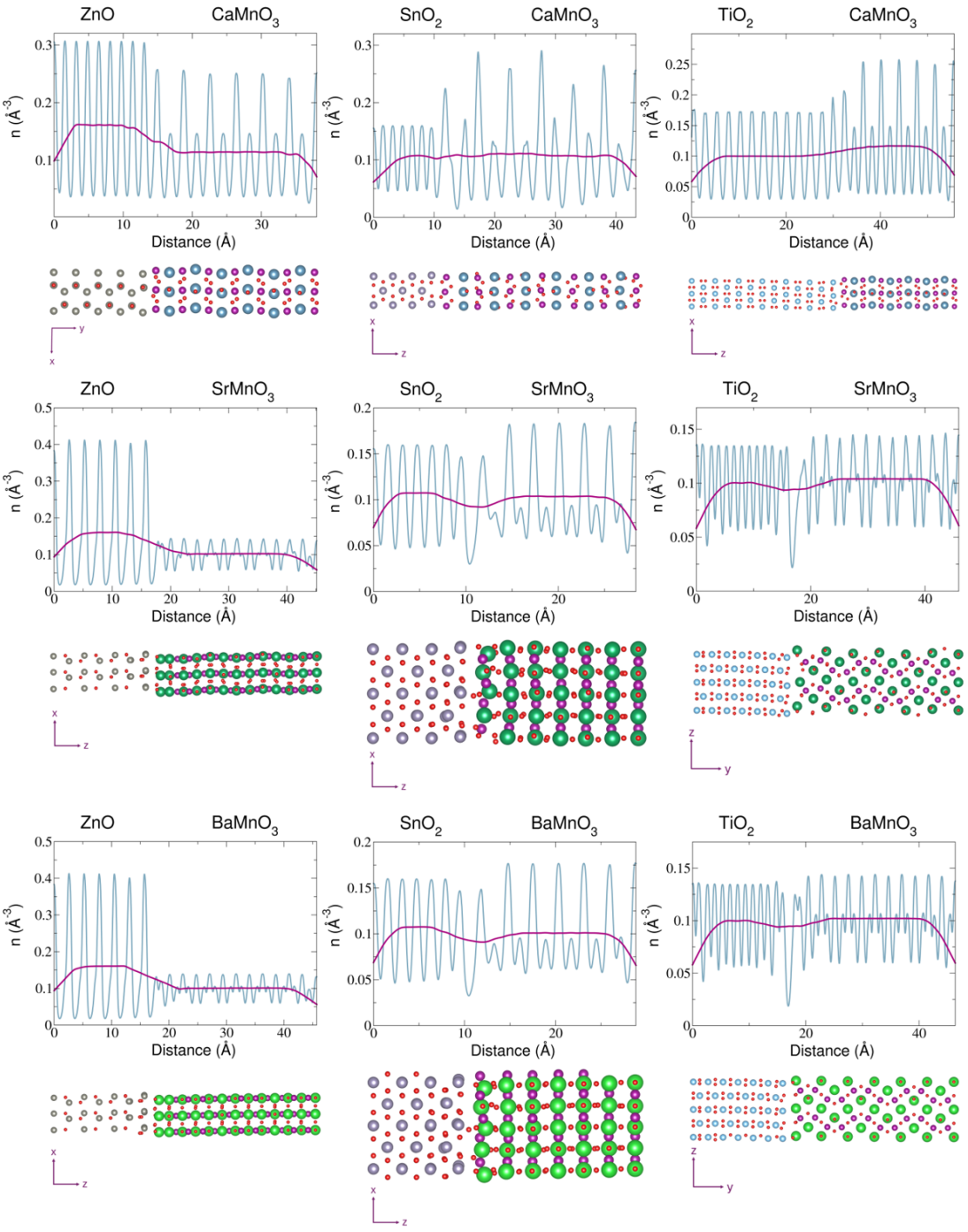

Figure 5.7: *Plane-averaged valence electron charge density shown with blue lines, and macroscopic average of the charge density shown with magenta lines for all nine heterostructures. Below each charge density plot a heterostructure supercell is shown for easier navigation. The ions are distinguished by colors as:* ● *oxygen,* ● *calcium,* ● *strontium,* ● *barium,* ● *manganese,* ● *zinc,* ● *tin, and* ● *titanium.*

However, throughout SMO slab difference in the plane-averaged charge density are noticeable compared to BMO slab. While throughout BMO slab a true bulk-like plane-averaged valence electron charge density behavior is found, where smaller density peaks belonging to manganese atomic layers have the same peak value, in SMO they are of different heights. This confirms that the changes in SMO slab are not restricted to only interface region, and that interface interaction causes changes throughout SMO slab. Nevertheless, the plane-averaged charge density demonstrates that this repeats periodically throughout the slab, further showing that interface interaction and possibly strain caused changes in the symmetry of SMO.

More detailed picture on the changes in the charge density upon interaction at the interface can be obtained by calculating the charge density difference. This difference is expressed as the difference between charge density of the interface and of two isolated slabs, where atomic positions are kept the same as in the heterostructure model

$$\Delta\rho = \rho_{MO/XMO} - \rho_{MO} - \rho_{XMO}, \tag{5.3.1}$$

where $\rho_{MO/XMO}$ is the charge density of the metal oxide/perovskite heterostructure, while ρ_{MO} and ρ_{XMO} are the charge densities of the isolated slabs. This way one can observe changes in the charge density that occur only due to the interaction at the interface.
For ZnO/CMO, charge density difference shows charge accumulation regions formed mainly around oxygen ions, and along oxygen-transition metal bonds. This confirs covalent bond formation. Arrangement of ZnO surface atoms at ZnO/CMO interface allows all manganese ions at the MnO_2 surface to form bonds with oxygen of ZnO, as well as zinc with oxygen of CMO. Displayed charge density difference indicates that the interface should be stable due to the formation of interface bonds. For CMO heterostructures with SnO_2 and TiO_2 this is not the case, as charge density difference shows partial bond formation at those interfaces. For SnO_2/CMO, plane-averaged charge density difference reveals electric dipole formation at the interface, due to charge accumulation region at SnO_2 surface, followed by a charge depletion region at the interface of similar magnitude. After the relaxation, oxygen ion of SnO_2 and of CMO got close enough that the electrostatic repulsion between them caused electrons to move away and form a depletion region between. Small fluctuations of the plane-averaged charge density difference within SnO_2 slab show that the charge density responds to formed interface dipole. In TiO_2/CMO, charge density difference in Figure 5.8 shows significant charge redistribution at the interface region. Very similar to SnO_2/CMO, a large depletion region is formed between two interface oxygen ions which got fairly close due to MnO_2 layer symmetry, and due to oxygen placement at TiO_2 surface. Charge accumulation at the interface region confirms covalent bond formation, mainly between titanium and MnO_2 layer oxygen, and partly

due to manganese-oxygen interface bond. Only partial Mn-O bond formation resulted in larger charge transfer from TiO_2 interface to CMO interface layer than from CMO to TiO_2, which will be confirmed with Löwdin charge analysis. In ZnO/SMO and ZnO/BMO, charge density difference plot reveals charge depletion regions around zinc ions, and charge accumulation around displaced oxygen ions of the perovskite (Figure 5.8).

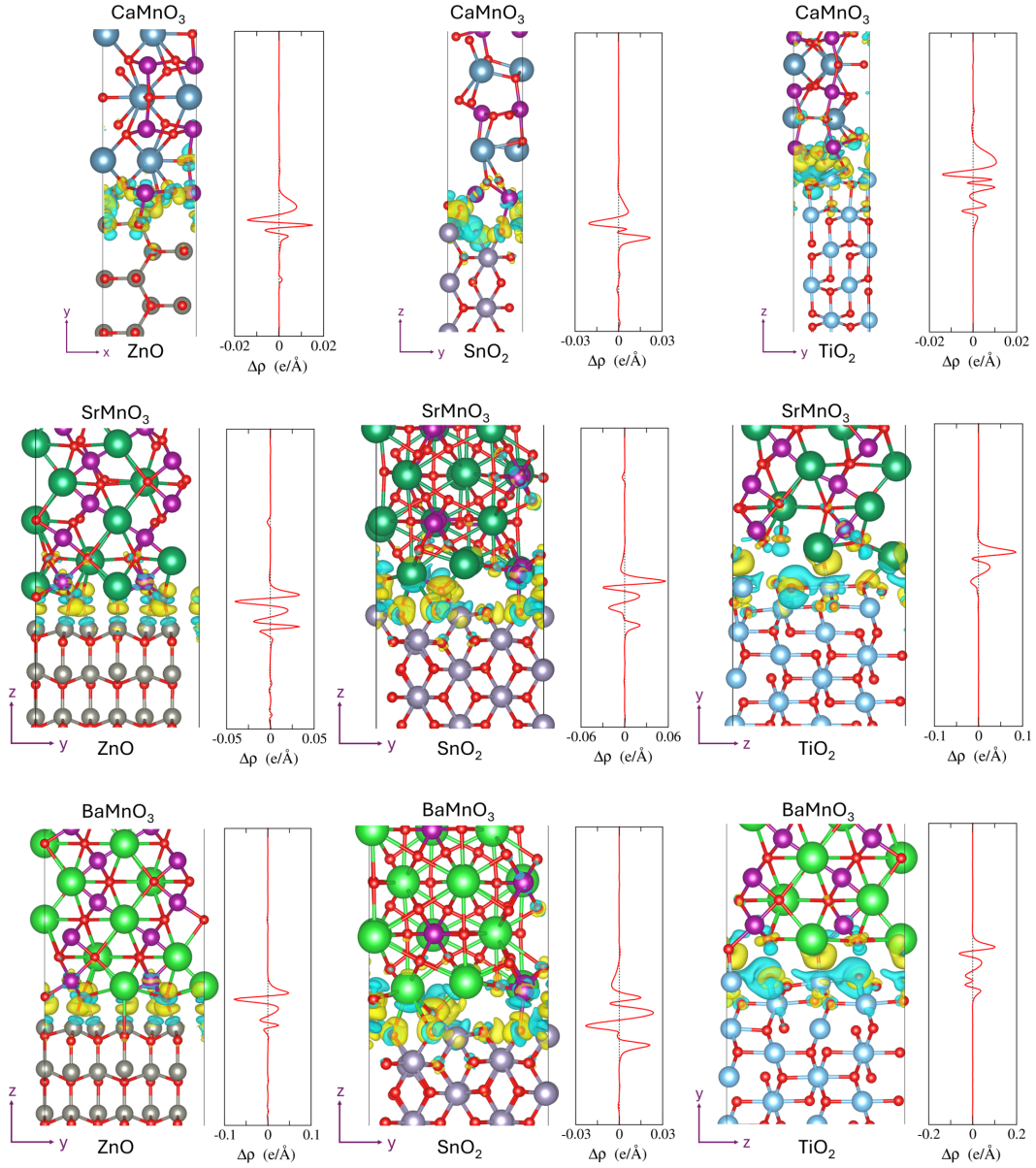

Figure 5.8: *Charge density difference isosurfaces and plane-averaged charge density differences at the interfaces of all studied heterostructures. Yellow isosurfaces show charge accumulation regions, and blue isosurfaces display charge depletion regions in all charge density difference visualizations. The isovalue was set at 0.005 e/Å^3. Here, ions are colored as:* ● *oxygen,* ● *calcium,* ● *strontium,* ● *barium,* ● *manganese,* ● *zinc,* ● *tin, and* ● *titanium.*

This creates well defined regions of charge depletion and accumulation along the direction of the growth of the heterostructure, forming an interface dipole. Because of the locations of the charge depletion and accumulation regions, ionic character of Zn-O bond can be assumed. Additionally, charge density distribution along the bond points to the partial covalent bond character. One dimensional plot of the charge density difference in Figure 5.8 shows large depletion region at the interface, followed by a charge accumulation region at oxygen atomic layer. A large depletion region around oxygen ions of BMO was shown to be a result of a weakened bond between oxygen and barium, due to the increased distance between oxygen and barium, and due to bond formation with zinc. In SMO and BMO heterostructure with SnO_2, changes in the charge density are easily visible at two layers closest to the interface in both materials. For SnO_2/SMO and SnO_2/BMO, although Figure 5.8 reveals a fairly balanced charge depletion and accumulation regions, polarity changes were observed at the second and third layer of SnO_2 around oxygen ions. This indicated the presence of the electric field due to interface dipole. Most interface ions were able to form bonds, although several were left with dangling bonds. This is easily visible from the centre towards the right side in SnO_2/SMO and SnO_2/BMO heterostructures in Figure 5.8, where several ions without interface bonds can be observed. For TiO_2/BMO and TiO_2/SMO, charge density difference in Figure 5.8 shows Ti-O bond formation. However, at TiO_2/BMO interface none of barium ions were able to form bonds, leaving them, and several oxygen ions from TiO_2 with dangling bonds. In SMO case, due to larger interface atomic displacements, one of two strontium ions was able to bond with oxygen of TiO_2. Density depletion region at the interface was formed above titanium ions in both cases. Because of large electronegativity difference between titanium and oxygen, titanium loses electrons to oxygen for partly ionic bond, while charge accumulation along the bond demonstrates covalent bond character as well. Charge is also depleted above several oxygen ions of TiO_2 due to proximity of BMO/SMO oxygen ions. Based on the plane-averaged charge density difference plots, TiO_2/BMO appears to undergo the most severe charge density changes, due to by far the highest valued peaks of charge depletion and charge accumulation. The largest value of charge accumulation is found below oxygen ions of BMO interface layer. Charge is depleted below them as they form no interface bonds, and electrons are redistributed along Ba-O and Mn-O bonds. A large accumulation region is also found across the interface, a result of Ti-O covalent bond formation.

Importantly, both macroscopic average plots and 3D charge density differences show that the bulk-like periodic behavior is restored within one unit cell away from the interface. This confirms that the models are sufficiently large so that relevant interface properties can be studied.

Charge transfer at the interface

To further study the interactions at the interface and bond formation, Löwdin charge analysis was performed [89]. Charge analysis allows one to gain knowledge on possible charge transfer which impacts potential alignment. For this, total charge of the atomic layers close to the interface was calculated. This was done for interface supercell model and for individual slabs. By calculating total charge difference of the same atomic layers in the heterostructure and in the isolated slabs, a redistribution of charge at the interface can be revealed. Table 5.3 shows the amount of charge each surface gained or lost due to interface interaction. For total charge of interface layers the charge of each ion forming the interface layer was summed. This was conducted for isolated slabs, and for the interface. Finally, to deduce possible charge transfer, the difference between total charge of the metal oxide interface atomic layer in slab structure and in interface model was calculated. The same was done for the perovskite interface atomic layer. In most cases charge is transfered from the metal oxide interface layer to perovskite interface layer. Opposite charge transfer was observed only in SnO_2 heterostructures with SMO and BMO. This is mainly due to the interface composition of SMO and BMO in those heterostructures, where they contain manganese in their interface layers. This led to significant charge transfer from manganese to oxygen of SnO_2 upon bond formation. In the cases where charge was transfered from metal oxide layer to perovskite interface layer, charge transfer mostly occured from transition metal cations to perovskite oxygen. Charge transfer further confirms partial ionic bond formation at interfaces. It was found that the largest charge transfer from metal oxide interface layer to perovskite interface layer occurs at ZnO/BMO and ZnO/SMO interfaces. This is a result of interface layer compositions. Because of large electronegativity difference between zinc from ZnO interface layer, and oxygen anions from SMO and BMO interface layer, significant charge transfer occurs from zinc to oxygen.

Table 5.3: *Total charge difference for interface models and slab models calculated from Löwdin charge analysis. Negative value indicates the loss of charge for the interface atomic layer in the interface model compared to isolated slab model, and positive value indicates gain of charge for the interface model compared to isolated slab model. All total charge values are expressed in the units of e, where e is unit charge.*

	ZnO/ $CaMnO_3$	SnO_2/ $CaMnO_3$	TiO_2/ $CaMnO_3$	ZnO/ $SrMnO_3$	SnO_2/ $SrMnO_3$	TiO_2/ $SrMnO_3$	ZnO/ $BaMnO_3$	SnO_2/ $BaMnO_3$	TiO_2/ $BaMnO_3$
metal oxide	-0.16	-0.18	-0.13	-1.34	+1.56	-0.01	-1.36	+1.53	-0.44
perovskite	+0.31	+0.14	+0.09	+1.82	-1.06	+0.10	+1.85	-1.06	+0.29

It is worth noting that the total charge transfer also depends on the number of ions that form the interface layer on both sides of the interface. Because of that, SMO and BMO heterostructures generally show larger charge transfer compared to CMO heterostructures. However, in TiO_2/SMO and TiO_2/BMO heterostructures smaller overall charge loss is found on TiO_2 side, mainly due to charge depletion on an oxygen ion of TiO_2, and not so much due to charge transfer. In the interface model titanium ions slightly gain charge, which is attributed to redistribution of the charge of oxygen ions which did not form interface bonds with SMO and BMO interface layer ions. At TiO_2/CMO interface, charge transfer across the interface is found mainly between titanium and oxygen, while due to partial Mn-O bond formation, charge transfer from CMO interface layer to TiO_2 interface layer was much smaller. Because manganese and titanium have nearly the same electronegativity, and both interface layers contain the same type of anions, similar charge transfer from metal oxide to perovskite, and from perovskite to metal oxide could have been expected if all transition metal-oxygen bonds were formed. However, as only one of two manganese ions formed interface bond, while all titanium ions bonded with oxygen of CMO, there is larger charge transfer from metal oxide surface to perovskite surface. Additionally, from Table 5.3 it can be easily seen that charge difference in TiO_2/CMO is the smallest among all studied heterostructures, due to several ions at each surface that did not form interface bonds. Perovskite to metal oxide charge transfer across SnO_2/SMO and SnO_2/BMO interface has a magnitude comparable to charge transfer of ZnO/SMO and ZnO/BMO interfaces. Much lower charge transfer is found at CMO interfaces compared to SMO and BMO interfaces. This can be mainly attributed to CMO surface termination. While transition metal-oxygen bonds generally contribute to the interface stability, with Ca-O termination a larger charge transfer could be expected due to larger electronegativity difference between calcium and oxygen at two different surfaces. However, most studies on methylammonium lead iodide perovskite and metal oxides interfaces show higher interface stability when MAPI is terminated with PbI_2 surface.

5.3.2 Heterostructure band structures and effective masses

The band structures of the interface supercell models are shown in Figure 5.9. Because the band structures show energies of the entire supercell, and not just the interface region, issues can arise during the analysis. One of such issues is the formation of states localized at the outer surfaces, a result of dangling bonds. Because these types of states do not appear in the heterojunction devices, and are a result of the limited size model, such states are disregarded and not considered in the analysis. The nature of the mid-gap states is investigated by calculating the probability density for these states, and plotting their isosurfaces. If the states appear localized at the outer surfaces of either slab, they are

disregarded. One such state is found in ZnO/CMO heterostructure, and two in SnO_2/CMO and TiO_2/CMO (Figure 5.10). Surface states are plotted with dotted blue lines in Figure 5.9.

Curvature of conduction bands in ZnO/CMO is visible. This indicates low effective mass around the interface region in ZnO/CMO heterostructure. In SnO_2/CMO a sharp peak of CBM is visible, and high curvature of the first unoccupied state. However, further at higher energies, conduction bands lose much of the curvature, which suggests increased electron effective mass. Similarly to ZnO/CMO, with low imposed strain on CMO in its supercell with TiO_2 ETL, high curvature of conduction bands is evident. With low imposed strain on CMO its heterostructures display relatively high curvature of the conduction band, indicative of lower electron effective mass. Additionally, probability density has revealed that two unoccupied states at the bottom of the conduction band in ZnO/CMO heterostructure are states localized to the interface region (Figure 5.11). These states are shallow electron trap states that are only slightly lower in energy than the subsequent conduction band states.

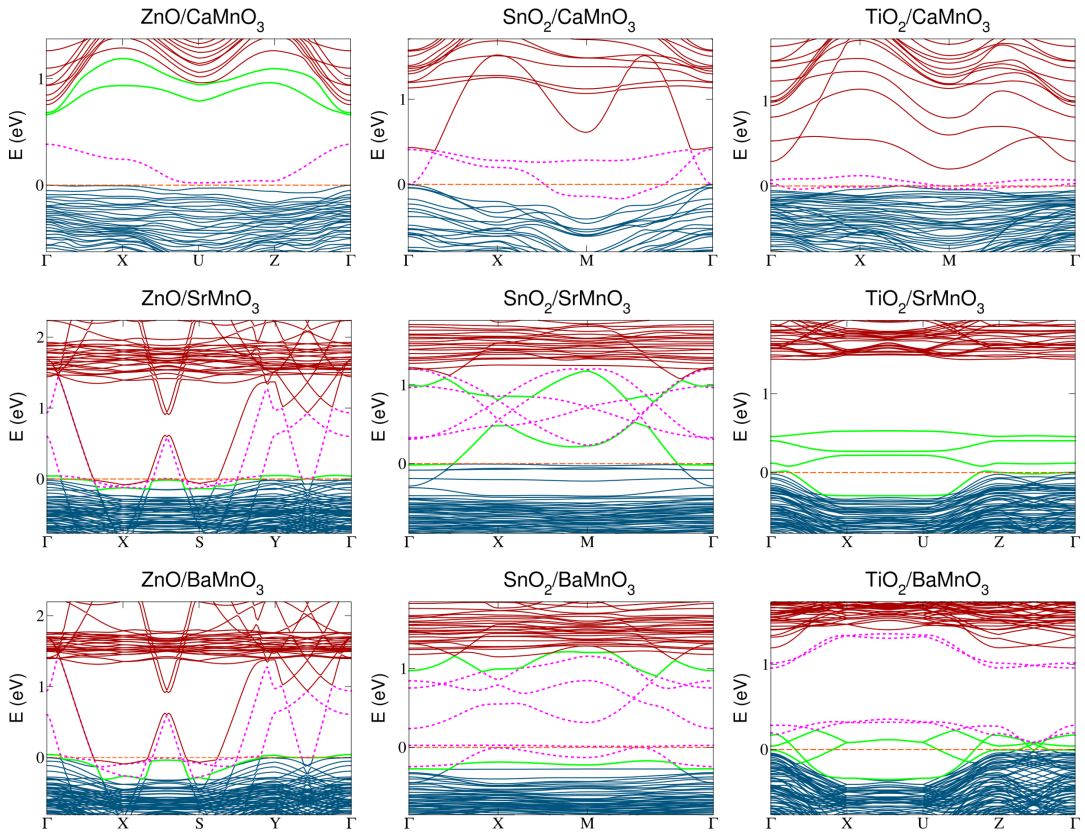

Figure 5.9: *Band structures of isolated interface models. Magenta dotted lines represent localized surface states. Green lines represent localized interface states. For all band structures zero energy level is set at the top of the valence band. Energy bands are projected in the plane parallel to the interface.*

While shallow electron trap states can act as recombination centers if they are formed below conduction band edge of ETL, they generally do not contribute as significantly towards increased recombination compared to deep trap states that can form mid-gap. No localized interface states are found at the gap area in SnO_2/CMO and TiO_2/CMO interfaces. SMO and BMO heterostructures with SnO_2 ETL show several mid-gap localized surface states. It is assumed that a larger number of localized surface states appear due to larger number of ions at the surface with dangling bonds. The confirmation that these states are surfaces states can be seen in Figure 5.12.

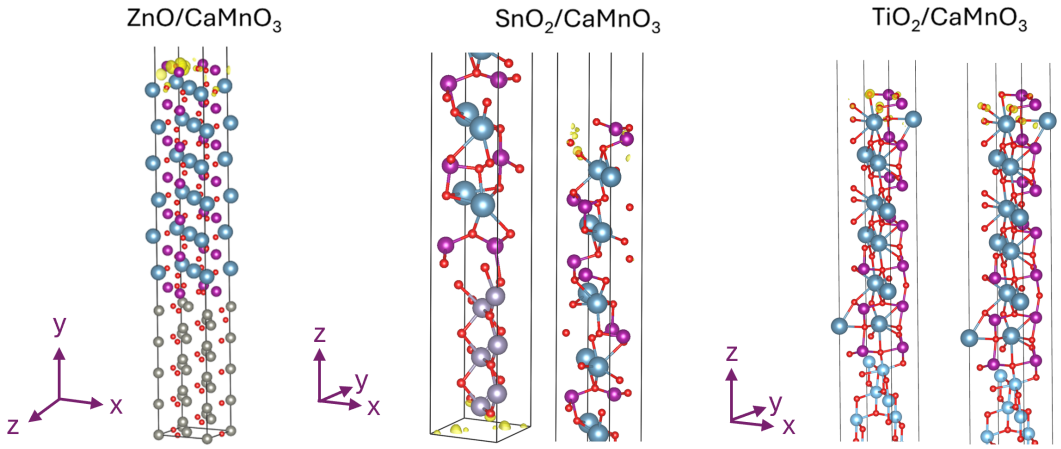

Figure 5.10: *Probability density isosurfaces for mid-gap states in $ZnO/CaMnO_3$, $SnO_2/CaMnO_3$ and $TiO_2/CaMnO_3$ heterostructures.*

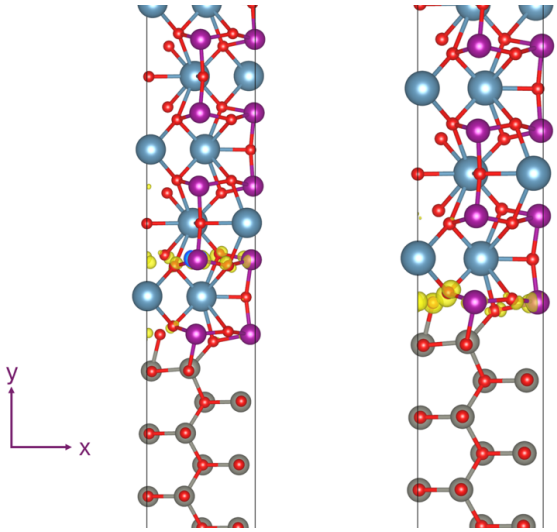

Figure 5.11: *Probability density isosurfaces for first two unoccupied non-surface states in $ZnO/CaMnO_3$ heterostructure.*

It can be further observed from probability density isosurfaces that the first unoccupied state in SnO_2/SMO and SnO_2/BMO heterostructures is an interface state (Figure 5.13). While in SnO_2/BMO heterostructure this is a shallow electron trap state, slightly below subsequent conduction band states, in SMO heterostructure it is formed deeper within band gap, making it much more detrimental for charge recombination. Furthermore, in both heterostructures an interface state is found at lower energies. In BMO heterostructure it is formed below Fermi energy, and shows a very shallow character, being only slightly higher in energy compared to energy levels below. For SMO heterostructure, top of the valence band interface state is much more dispersive and goes deeper towards unoccupied states. Therefore, it can be concluded that in SMO and SnO_2 heterostructure states localized at the interface have formed that have a significant impact on charge recombination. This is mainly a result of a larger displacement of SnO_2 oxygen towards the center of the interface in SnO_2/SMO than in SnO_2/BMO heterostructure.

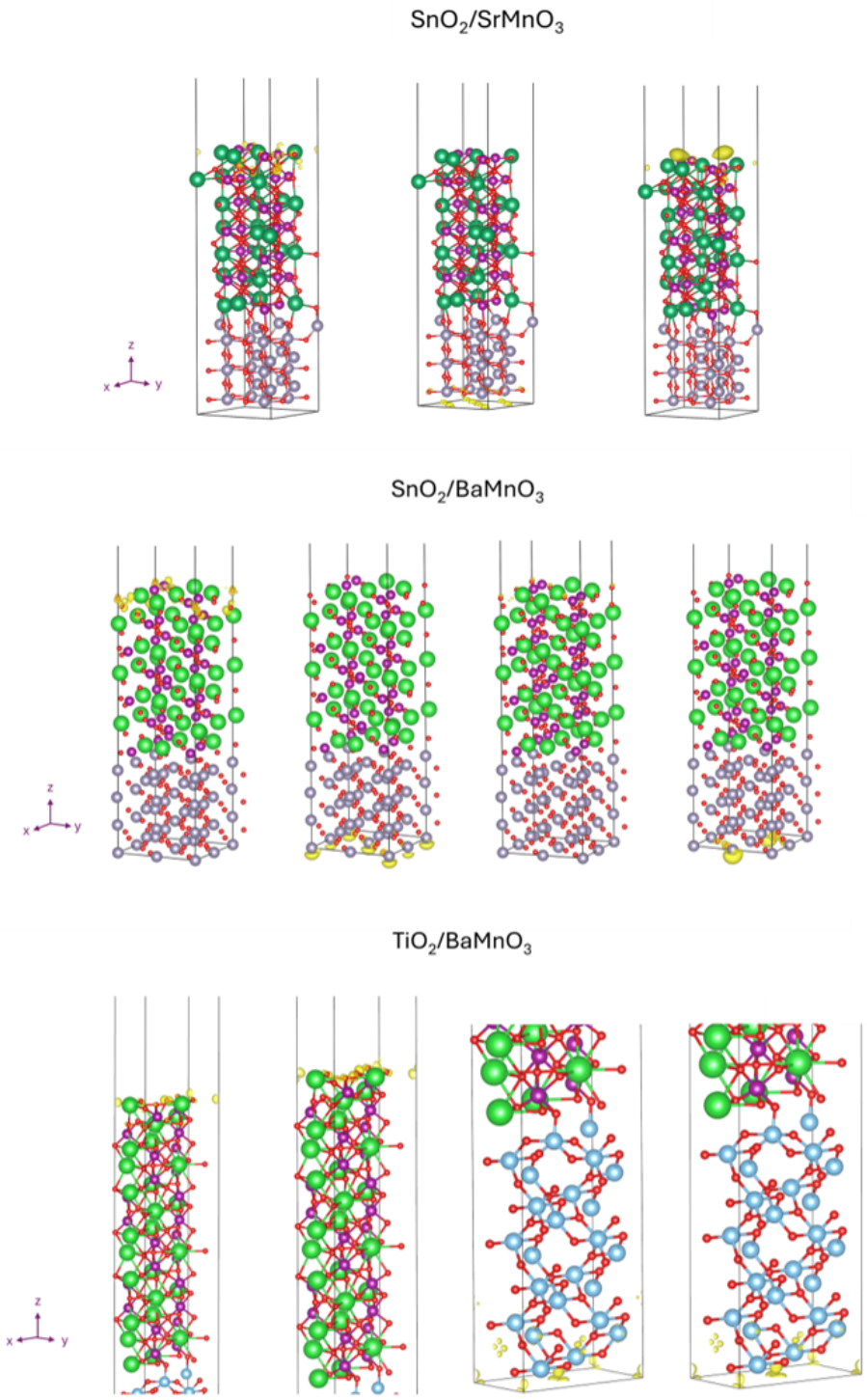

Figure 5.12: *Probability density isosurfaces for several mid-gap energy states in $SnO_2/SrMnO_3$, $SnO_2/BaMnO_3$, $TiO_2/BaMnO_3$ heterostructures. Yellow isosurfaces demonstrate that dotted lines in the band structures are localized surface states. The order of the isosurface plots corresponds to order of energy states, from lower to higher energy. Isovalue was set to 0.002 e/Å^3 for SnO_2 heterostructures, and to 0.01 e/Å^3 for TiO_2 heterostructures.*

Beyond formed interface state in SnO_2/SMO and SnO_2/BMO heterostructure, the rest of the conduction bands have a flat character, indicating higher effective mass. While this has an impact on electron mobility through the interface region, this region is very thin compared to the size of thin films in photovoltaic devices, being in the range of several tens of nanometers to several micrometers. For instance, optimal SnO_2 ETL thickness was found to be 15 nm [90]. Compared to the thickness of the interface region, which is around 1 nm, it is easily concluded that this is a very narrow area compared to device layer thickness, especially considering that perovskite thin films are typically even thicker, around 250 nm to 750 nm [91]. In TiO_2/SMO four interface states formed, and in TiO_2/BMO heterostructure, three interface states formed above occupied states, followed by four localized surface states. In TiO_2/SMO heterostructure, the formed interface states form deeper within the gap, while in TiO_2/BMO, interface states that emerge are shallow hole trap states which do not significantly increase recombination as the difference between top of the valence band and top of the interface trap states is around 0.2 eV. Localization of interface states is visualized in Figure 5.14, and four surface states are visualized in Figure 5.12. Bottom of the conduction band in TiO_2/BMO resembles the bottom of the conduction band of TiO_2. It was further confirmed from probability density that first two unoccupied states are TiO_2 bulk states. This suggests that the electron effective mass in the vicinity of this interface should be around the same value as in the bulk of TiO_2.

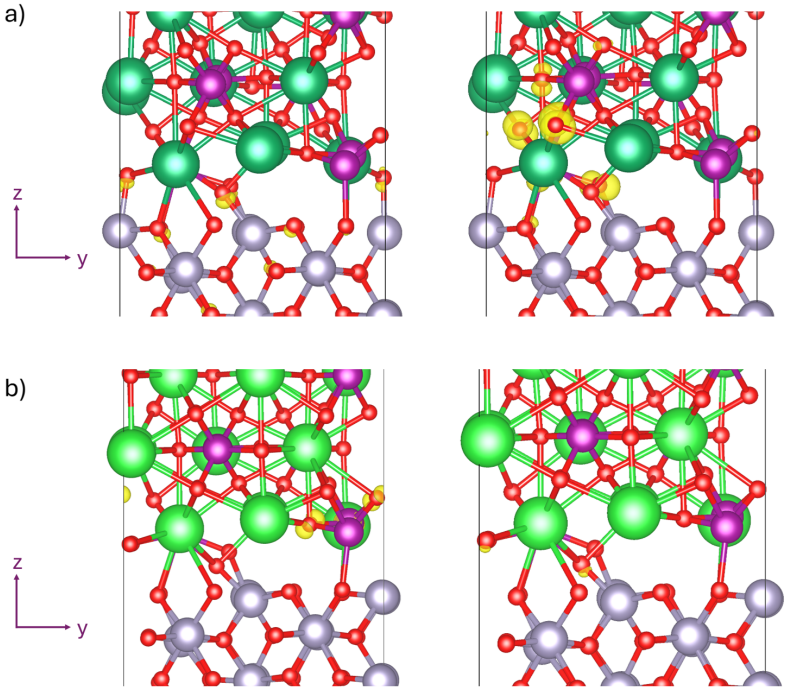

Figure 5.13: *Probability density of two gap energy states of a) SnO_2/$SrMnO_3$ and b) SnO_2/$BaMnO_3$ heterostructures. Yellow isosurface shows localization of the probability density to the oxygen ions at the interface region. Isovalue was set at 0.005 e/Å^3.*

In TiO_2/SMO, the bottom of the conduction band has a flatter character, where likely SMO conduction band states are at the bottom. This suggests that TiO_2 bulk conduction states are at higher energies than SMO bulk states, hinting at type I band offset. Formed interface states are a results of unbonded interface ions, mainly oxygen of BMO and SMO. Although there was only partial bonding at the interface, no deep trap states were formed mid-gap as a result of dangling bonds. Further, in SMO and BMO heterostructure with ZnO ETL, highly dispersive states emerge. The nature of these dispersive states was further investigated via probability density isosurfaces, which have shown that the first unoccupied state is a localized interface state, two highly dispersive states are localized zinc surface states, and the last highly dispersive state is perovskite bulk-like state. Probability density plots for these states are given in Figure 5.15. Isovalue for the shown isosurfaces was intentionally increased so that the isosurfaces show the most probable locations, and not the entire range of possible locations, making it easier to facilitate characterization. Despite band structures of ZnO/SMO and ZnO/BMO heterostructures displaying that band gap is non-existent, because the formed states are identified as surface states, the actual interface does not have a metallic character. This will be further confirmed from LDOS in Chapter 5.3.4. A formed interface state is again a shallow hole trap state, formed at the top of the valence band. Generally, most of the conduction bands at ZnO/BMO and ZnO/SMO interfaces are flat, with increase in curvature at higher energies. This means that for the most part lower electron mobility is predicted at these interfaces.

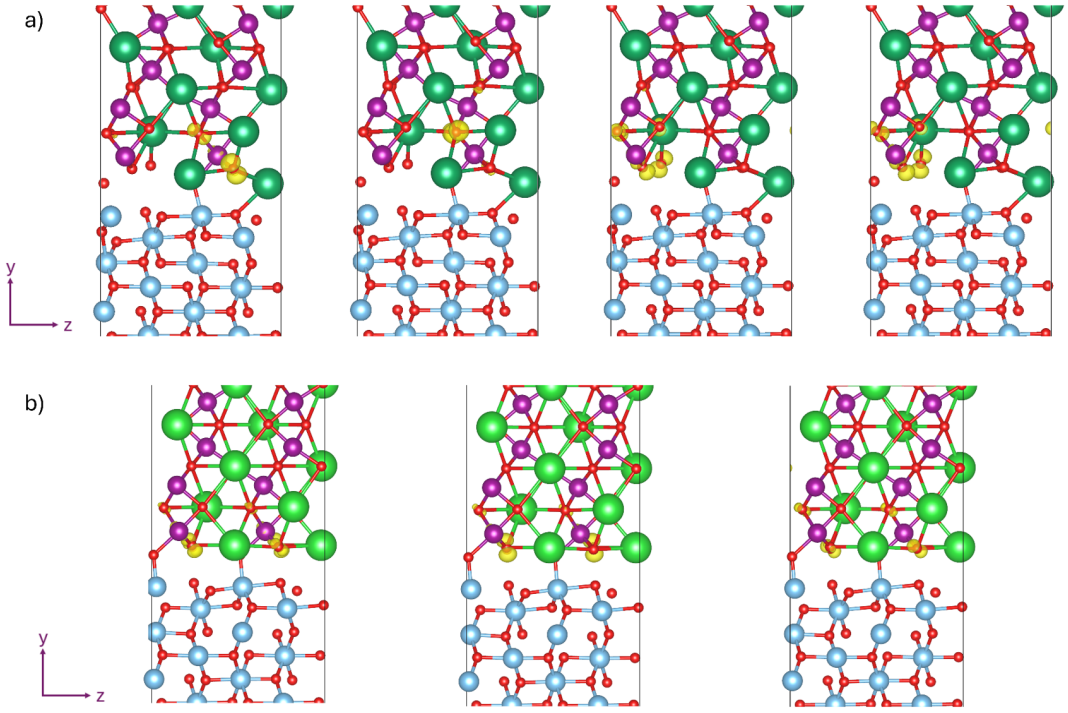

Figure 5.14: *Probability density isosurfaces for a) four interface states in TiO_2/SMO, and b) first three unoccupied states in TiO_2/$BaMnO_3$ heterostructure. These states were highlighted with green color in the corresponding band structures. The isovalue was set at 0.005 e/Å^3.*

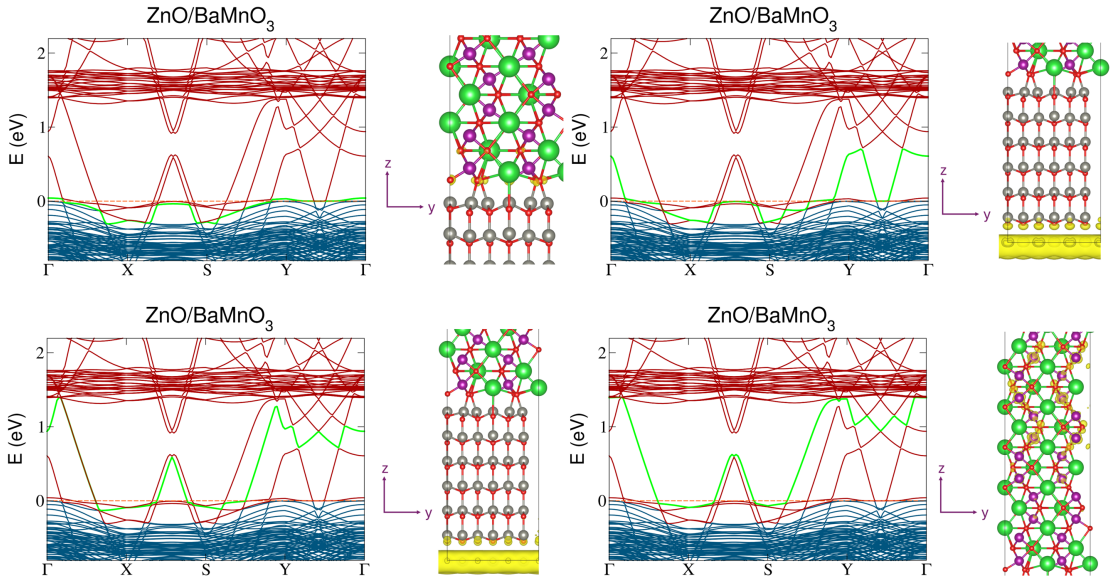

Figure 5.15: *Band structures and probability densities for ZnO/$BaMnO_3$ heterostructure. Probability density isosurfaces in yellow are showing the locations of the electrons populating the energy states highlighted in green color in the band structure plots.*

To calculate the change in the effective mass in the vicinity of the interface, lowest electron effective mass was calculated for metal oxides and strained perovskites. Figure 5.16 shows schematically how electron effective mass changes in the vicinity of the interface. Within strained perovskites the electron effective mass is between $0.44m_0$ and $5.99m_0$. Higher electron effective mass within strained SMO and BMO means that it is more difficult to transport photoexcited electrons through the strained region due to reduced mobility. However, once the electrons are transported into the ETL, smaller effective mass aids in their transport towards the electrode by reducing carrier recombination. For metal oxides, the calculated effective mass was compared to previous measurements. Excellent agreement was found for all three metal oxides. Previous measurements conducted via cyclotron resonance gave SnO_2 electron effective mass of $0.23m_0$, and for ZnO $0.29m_0$. Theoretical calculation of the effective mass for TiO_2 which was previously conducted based on GGA+U approach gave electron effective mass of $0.59m_0$, also in very good agreement with our results.

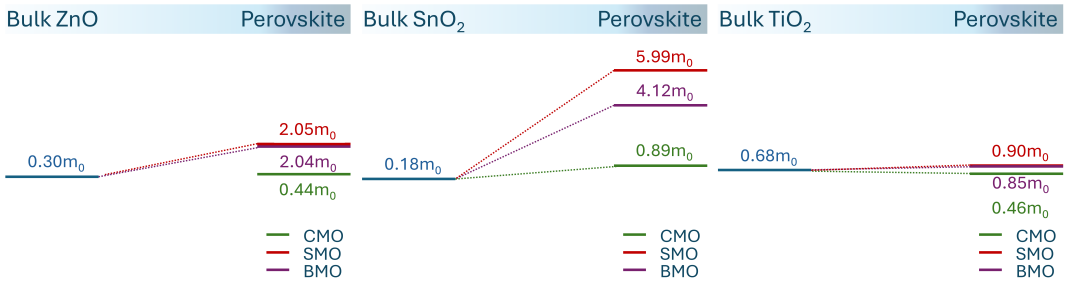

Figure 5.16: *Approximated electron effective mass in bulk metal oxides and strained perovskites.*

5.3.3 Electrostatic potential

With theoretical methods, there are generally two approaches to calculate the band offset. One approach is through the calculation of local density of states. Local density of states (LDOS) shows spatial and energy dependence of density of states, and it can be effectively used to study how energy bands align at the boundary of two semiconductors. However, this approach is not used often due to high computational cost, as accurate calculation of LDOS requires very dense k-point grid. Additionally, it is often difficult to obtain precise values of band offsets. The second approach which can be applied to find the relative band alignment of two semiconductors in contact is the electrostatic potential approach. In this method, the average electrostatic potential is used as the common reference for band edge position alignment. This is done by aligning the energy band edges (VBM and CBM) to the average potential level of the bulk. Far from the interface the macroscopic average assumes bulk-like behavior, indicated by the constant value of the macroscopic average of the electrostatic potential. The differences between the position of the VBM and CBM to the average bulk potential are transferred to the heterostructure electrostatic potential. This is done on both sides of the interface, hence demonstrating how band edges join at the junction. Potential lineup of two semiconductors is affected by several factors, such as chemical composition of the semiconductors, electron affinities, Fermi levels, surface orientation, and surface termination. Just as with charge density, electrostatic potential is plane-averaged, where local minima correspond to atomic layers. Figure 5.17 shows plane-averaged potentials and their corresponding macroscopic averages. Small deviations from the bulk-like behavior of the potential are found at ZnO/CMO interface. This is in line with slight changes of the charge density due to the interface interaction, and no predicted electric dipole formation.

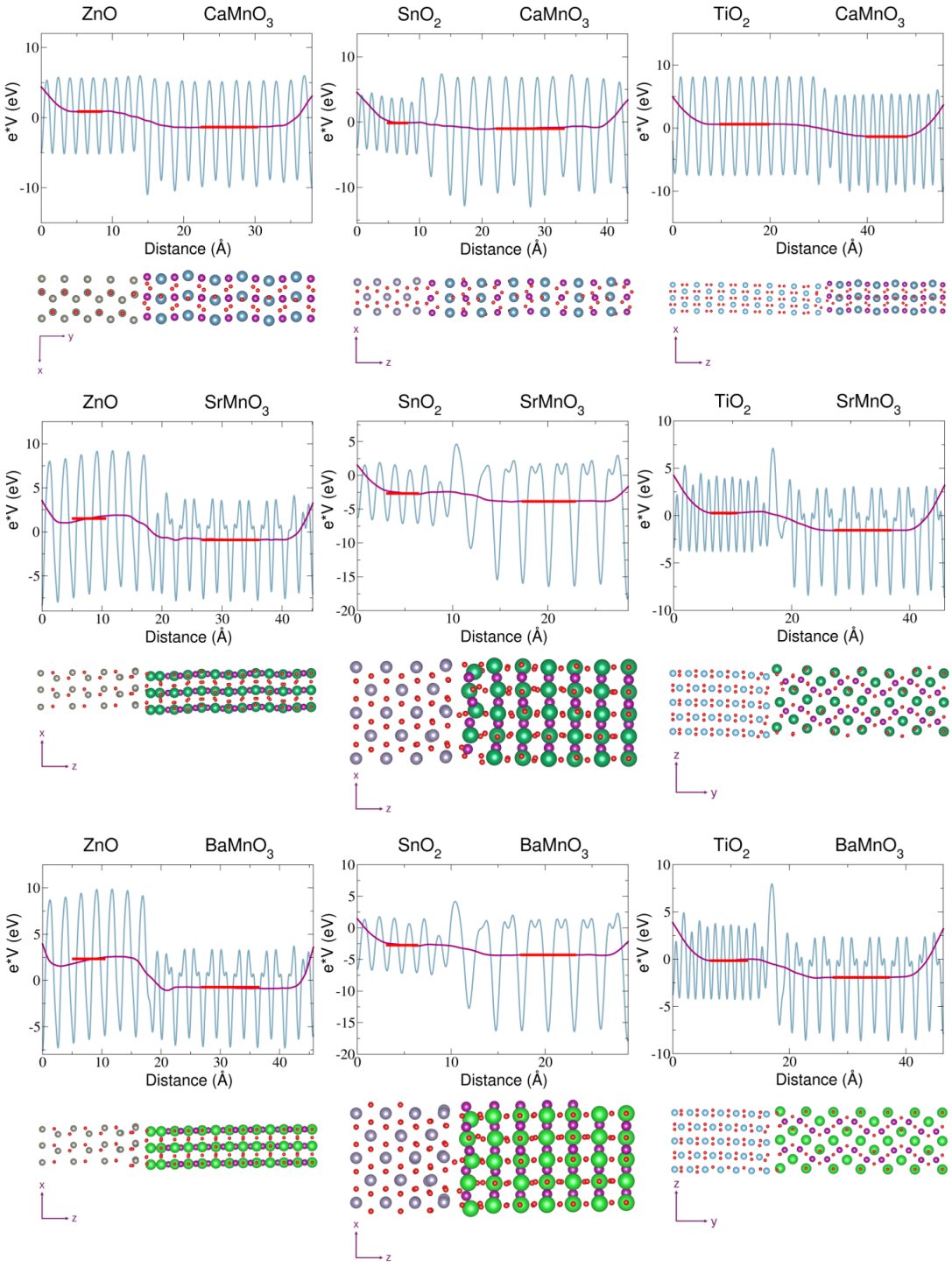

Figure 5.17: *Plane-averaged electrostatic potential displayed with blue lines, and macroscopic average of the electrostatic potential displayed with magenta lines. Red lines highlight constant values of the electrostatic potential used for the potential difference (lineup) calculation.*

Similar behaviour is found in TiO_2/CMO heterostructure, with slightly more noticeable changes at the interface region, but with again, no observable electric dipole formation. In SnO_2/CMO heterostructure, interface region shows larger changes of the electrostatic potential, caused by more pronounced interface interaction, and a small slope of the electrostatic potential across metal oxide slab. Plane-averaged electrostatic potential shows changes throughout CMO slab due to significant structural changes. Table 5.4 shows potential differences calculated from the macroscopic average potential lineup. The values of the potential used for potential difference calculations are highlighted with red in Figure 5.17. This potential value corresponds to the bulk average potential. In all three heterostructures, CMO macroscopic averaged potential is deeper with respect to metal oxide average potential. For CMO heterostructures with ZnO and TiO_2, the potential difference is similar. For SnO_2/CMO heterostructure, much smaller potential difference was calculated. Small potential difference is in part a result of an increase of interlayer distance in CMO due to the large expansion in the direction of the growth of the heterostructure under compressive strain. This shifts CMO potential upwards, giving small potential difference with SnO_2. For SMO and BMO, nearly the same electrostatic potential plots were obtained, with small differences mainly due to difference in imposed strain, and due to differences in interface interaction. A larger slope of the macroscopic average of the electrostatic potential is found within ZnO slab in its heterostructures with SMO and BMO, and very subtle slope in SnO_2/SMO and SnO_2/BMO heterostructures, again, only on the metal oxide side of the heterostructure. In all studied heterostructures no observable slope was found in the perovskite side. In TiO_2/BMO interface region electrostatic potential shows larger deviations from the bulk-like behavior. Despite larger deviations at the interface, beyond unit cell closest to the interface macroscopic potential on both sides attains constant value, demonstrating regain of bulk-like behavior. No interface dipole effect was observed in Figure 5.17 for TiO_2/BMO heterostructure, as macroscopic average has a constant value throughout the majority of each slab. A large spike of the electrostatic potential in the middle of the interface corresponds to low density region at the interface. This is because the only contribution towards charge density across the interface was found along Ti-O bonds. Even larger potential difference is found between SMO and ZnO, and especially between BMO and ZnO compared to ZnO heterostructure with CMO.

Table 5.4: *Potential difference (lineup) across $XMnO_3$ heterostructures (X = Ca, Sr, Ba).*

	ZnO/ $CaMnO_3$	SnO_2 $CaMnO_3$	TiO_2/ $CaMnO_3$	ZnO/ $SrMnO_3$	SnO_2 $SrMnO_3$	TiO_2/ $SrMnO_3$	ZnO/ $BaMnO_3$	SnO_2 $BaMnO_3$	TiO_2/ $BaMnO_3$
$\Delta V(eV)$	-2.22	-0.86	-1.97	-2.43	-1.18	-0.57	-3.17	-1.54	-1.77

For SMO and BMO the lowest potential difference was calculated in their heterostructures with SnO_2. Same was found for CMO heterostructures. Because metal oxides have significantly larger band gap, more than double compared to manganese perovskites, it is expected that smaller potential difference should benefit the band alignment. TiO_2/BMO heterostructure shows larger potential difference, but still substantially smaller than in ZnO based heterostructures. As hexagonal systems can easily be directly compared, the potential difference calculations suggest that BMO based heterostructures have significantly higher potential difference with studied metal oxides compared to SMO heterostructures. While this can partially be attributed to strain differences on perovskites, the rest comes down to interaction difference due to different $A-$site cation, and due to larger total number of electrons in barium compared to strontium, raising the total charge density, and thereby lowering the electrostatic potential of BMO compared to SMO.

Potential difference is affected by the charge transfer at the interface. In ZnO/CMO heterostructure, the largest charge transfer from CMO to metal oxide was observed among CMO heterostructures, leading to the largest potential difference. In ZnO/SMO and ZnO/BMO heterostructure the largest overall charge transfer from the metal oxide surface ions to perovskite surface ions occurs, which causes the largest potential difference out of all studied heterostructures. In TiO_2/SMO and TiO_2/BMO heterostructures charge transfer from TiO_2 surface to perovskite surface also occurs, but at much smaller scale. This causes lower relative potential difference compared to ZnO based heterostructures. Only in SMO and BMO heterostructures with SnO_2 charge transfer from the perovskite surface to SnO_2 surface was observed, which led to the lowest potential difference among SMO and BMO heterostructures.

In the previous section, charge density difference isosurfaces have disclosed the presence of the interface dipole. In ZnO/BMO and ZnO/SMO it was easily noticeable from layered charged depletion and charge accumulation regions along the growth of the heterostructure, and in SnO_2/BMO and SnO_2/SMO the presence of electric field due to interface dipole was observed from the polarity changes at SnO_2 atomic layers. The slope of the electrostatic potential can introduce uncertainties into potential lineup calculation. The level of uncertainty depends on the magnitude of the generated electric field, and on the response of the charge density, as this electric dipole persists through the heterostructure (non-vanishing dipole). To determine why metal oxides charge density responds far more significantly to the electric dipole than the perovskites charge density, charge density difference isosurfaces were studied with significantly lowered isovalue. This reveals smaller changes in the electron charge density, which shows as very useful for studying the effects of induced interface electric dipole. Significantly lowered isovalue for ZnO/BMO interface demonstrates polarity changes around oxygen ions in ZnO. Because of Zn-O

bond type and bond angle, charge density is depleted on the bottom side of oxygen ions throughout the ZnO slab, and accumulates on top, with also visible polarity changes around zinc ions, albeit at smaller scale. The alignment of charge depletion and accumulation regions causes a pronounced slope of the electrostatic potential across ZnO slab in the heterostructures with SMO and BMO. For the same isovalue no charge depletion and accumulation regions emerge across SMO and BMO perovskites. To notice any changes in the charge density of the perovskite slab, isovalue had to be further lowered. It was then possible to observe local charge depletion and accumulation regions around oxygen ions within BMO. However, the fact that isovalue had to be lowered significantly points to the fact that the response of SMO and BMO charge density is minor. Due to the nature of the bonding in SMO and BMO perovskites, the charge density responds in a way that does not lead to slope of electrostatic potential across perovskite slab. More precisely, the shown density charge accumulation and depletion regions resemble the shape of the π antibonding orbitals. Because of the bond angles with surrounding cations, the bonding orbitals are oriented in a way that the induced polarity changes have no net effect on the electrostatic potential in the direction of the growth of the heterostructure. Similar effect is also found at BMO heterostructure with SnO_2. However, due to the bond angle of oxygen with tin, which is angled relative to the direction of the growth of the heterostructure, and due to lower magnitude of electric field generated by interface electric dipole, the response of the charge density around oxygen ions throughout SnO_2 slab is much lower (Figure 5.19). Therefore, to be able to observe any polarity changes within SnO_2 slab, isovalue had to be reduced by an order of magnitude compared to ZnO/BMO case.

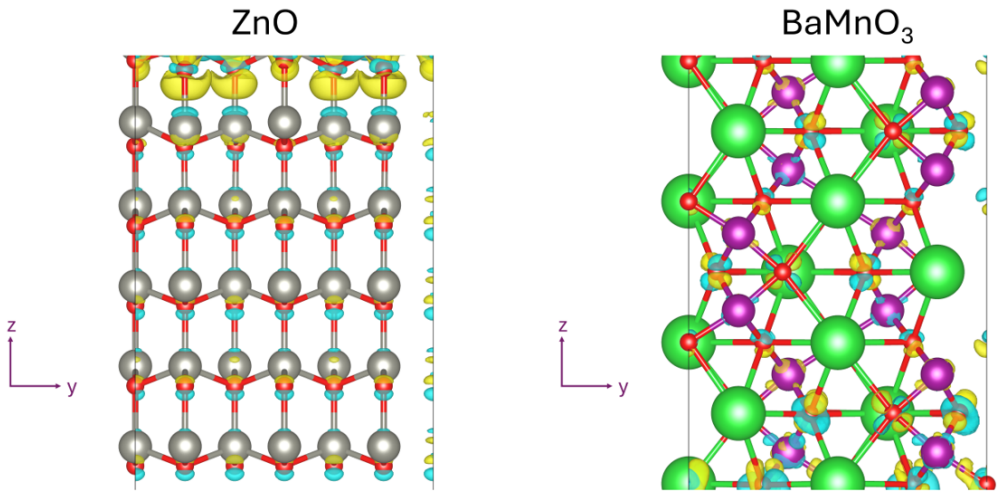

Figure 5.18: *Charge density difference isosurface for ZnO and $BaMnO_3$ slabs extracted from their heterostructure. Isovalue for ZnO slab was set at 0.001 e/Å^3, and for $BaMnO_3$ the isovalue was set at 0.0001 e/Å^3.*

Even with such a low isovalue no visible changes were observed in BMO slab. Again, isovalue had to be lowered another order of magnitude to be able to see any changes in BMO slab charge density, which showed very similar charge depletion and accumulation regions around oxygen ions as in ZnO/BMO case. Due to Mn-O and Ba-O bond angle and bond type, charge density surrounding oxygen ions throughout BMO slab is barely impacted by the interface dipole, and produces no net effect along the growth of the heterostructure. Similar effects were found in SMO heterostructures. In general, the slope of the macroscopic average of the electrostatic potential found in these heterostructures can be attributed to larger polarity changes in metal oxide slabs than in perovskite slabs, which depends on surface orientation and termination [92, 93].

For potential difference calculations of two slabs joined to form the interface, a constant value of the electrostatic potential in the bulk-like region is required. For sloped electrostatic potentials, the average potential over the middle unit cell in the metal oxide slab was used. It was calculated as an average value of the plane-averaged electrostatic potential across the region that corresponds to the middle of the metal oxide slab. The average value calculated this way is highlighted in red in Figure 5.17.While it can be seen that there is significant overlap of the red line for the SnO_2 based heterostructures, there is significant deviation of the edges of the red line across ZnO middle unit cell in ZnO/SMO heterostructure, and even more so in ZnO/BMO heterostructure. In the previous study on the band offset in polar and nonpolar heterostructures the potential lineup for polar interfaces was calculated using the linear least squares fitting [94].

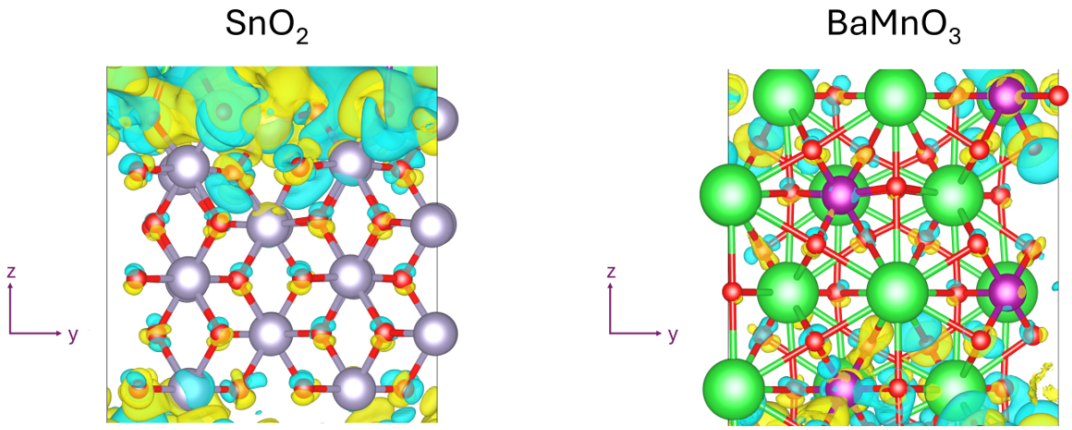

Figure 5.19: *Charge density diffence isosurfaces for SnO_2 and $BaMnO_3$ slabs extracted from their heterostructure. Isovalue for charge density difference was lowered so that polarity changes induced by interface dipole can be observed. Isovalue for SnO_2 slab was set at 0.001 e/Å^3, and for $BaMnO_3$ the isovalue was set at 0.0001 e/Å^3.*

There, it was assumed that the effects of interface dipole exist only in the two atomic layers closest to the interface. From this assumption, the linear least squares fit line was drawn along the macroscopic average of the potential, and the value of the potential at which the linear squares fit line intersected the center of the second atomic layer was chosen as the potential value for potential lineup calculation. In this thesis, this method was not used to avoid making assumptions on how deep within the slab does the interface dipole have an effect. However, the choice of average potential value over the middle unit cell leads to uncertainties in the exact band offset for ZnO heterostructures with SMO and BMO perovskites.

Surface dipole correction

Due to charge asymmetry in slab models, and due to periodic boundary conditions, an artificial electric field can be formed through the vacuum region. This manifests in the slope of the vacuum potential, and can lead to errors in band offset calculation as it can affect the electrostatic potential alignment. The artificial electric field can affect the electrostatic potential, giving a different average potential value in the bulk-like region to the one that would be calculated if no artificial electric field was present. To determine how surface dipoles affect the electrostatic potential, which is a crucial part of band offset calculation, surface dipole correction was implemented for the case where the largest surface dipole was found. If it is determined that it has no large contribution towards potential lineup when electric field due to surface dipole has the largest magnitude, it is reasonable to assume that for lower magnitude electric fields it has even less of an impact on potential lineup, and can be effectively disregarded. Because the implementation of the dipole correction can introduce difficulties in reaching self consistency and obtaining the ground state energy of the system, it is beneficial if it does not need to be applied for relatively precise band offset values. The largest surface dipole produced the largest slope of the electrostatic potential of the vacuum slab. To counteract the effects of the induced electric field, a correction can be applied where charge is placed within vacuum region to negate the effects. If the surface dipole is formed in the z direction of the supercell, the surface dipole correction is calculated as [95]

$$V_{dip}(z) = 4\pi m \left(\frac{z}{z_m} - \frac{1}{2} \right), 0 < z < z_m, \tag{5.3.2}$$

where z_m is the length of the supercell, and m is the surface dipole density

$$m = \int_{-\infty}^{\infty} \rho_{av}(z') z' dz'. \tag{5.3.3}$$

It is crucial to implement dipole correction within the vacuum region so that supercell

charge density is not affected other than by counteracting surface dipole effect. After the surface dipole correction was applied, electrostatic potential was recalculated to asses how significantly surface dipole affects the macroscopic potential from which the potential lineup is calculated. In the vacuum region of SnO_2/BMO heterostructure the largest magnitude of surface dipole was found. When dipole correction was applied, the electrostatic potential and its macroscopic average had nearly the same behavior. From Figure 5.20 it is evident that surface dipole contributes very little to the overall electrostatic potential and its macroscopic average. Both plane-averaged electrostatic potential and the macroscopic average overlap regardless of applied dipole correction. This result proves that the dipole correction is not necessary for accurate band offset results. Upon closer inspection of Figure 5.20, it can be observed that there is nearly a complete overlap of macroscopic averages when surface dipole is corrected and when it is not corrected within BMO slab. Slight deviation is found through SnO_2 slab. This is again a result of different response to the induced electric field of metal oxide and perovskite due to previously described reasons. However, the deviation of macroscopic average with applied dipole correction was found to be around 0.05 eV in the middle of SnO_2 slab, leading to the conclusion that it does not significantly affect potential difference calculation. Given that the potential difference over vacuum region is around seven to ten times larger for SnO_2/BMO heterostructure (slightly smaller for SnO_2/SMO) than in any other studied heterostructure (vacuum potential difference was around 3 eV compared to around 0.3 eV to 0.5 eV for other heterostructures), the dipole correction is not necessary as it introduced only minor errors in potential lineup calculations. An example for the case of low magnitude electric field dipole correction can be found in the Appendix B.

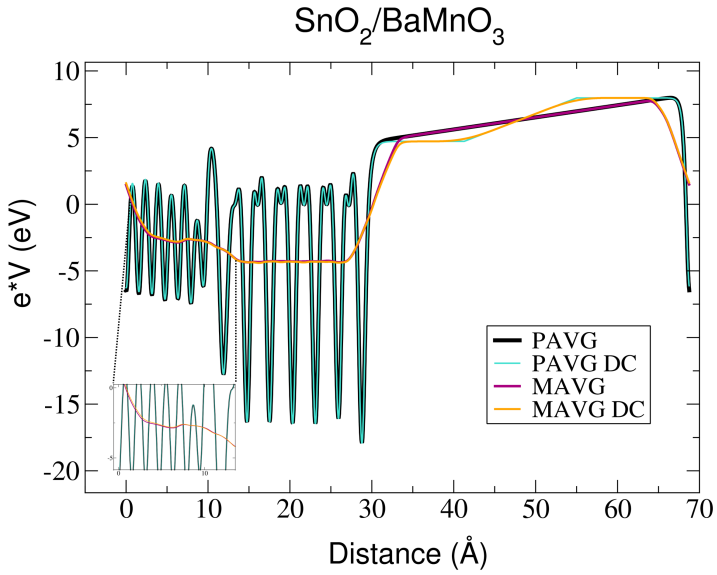

Figure 5.20: *Plane average and macroscopic average of the electrostatic potential of SnO_2/$BaMnO_3$ for dipole corrected and non-dipole corrected case. Below SnO_2 potential part of SnO_2 slab potential is enhanced to display difference between macroscopic potentials for dipole corrected and non-dipole corrected case. PAVG represents plane-averaged electrostatic potential without dipole correction, PAVG DC represents plane-averaged electrostatic potential with dipole correction, MAVG represents macroscopic average of the electrostatic potential without dipole correction, and MAVG DC represents macroscopic average of the electrostatic potential with dipole correction applied.*

5.3.4 Relative band alignment - band offsets

Band offset, as one of the most important properties of the two semiconductors in contact, has critical impact on charge dynamics and transport. Favourable band offset of two semiconductors provides a pathway that enables improved diffusion of charge carriers. If charge carriers are collected efficiently at the interface, recombination rate is low, and overall efficiency of the device is high. This crucially depends on several other factors, such as defect density at the interfaces, charge carrier lifetime, and charge mobility. Efficient charge carrier transport relies on favourable band offset which can diminish the effects of charge recombination. For the interfaces studied in this thesis, conduction band alignment between perovskite absorber and metal oxide ETL is the focus, as it improves the efficient transport of photoexcited electrons into the conduction band of ETL. Nevertheless, the valence band alignment is also of interest, as ETL needs to prevent hole transport towards the TCO. To calculate both valence and conduction band offsets, band edges are aligned with respect to the average potential of the bulk, as previously described. This alignment is then transfered to the heterostructure electrostatic potential plot, where band edges are aligned to the average of the electrostatic potential in the bulk-like region, giving relative

alignment of the band edges of the two semiconductors in contact. Figure 5.21 displays obtained band offsets for the nine studied heterostructures. Regarding the valence band offset (VBO), all heterostructures show favourable alignment, as the valence bands in perovskites are higher in energy than those in metal oxides. When electrons from the top of the valence band are photoexcited into the conduction band, the empty states within valence band of the perovskite have higher energy than of metal oxides. This prevents the transport of valence electrons from metal oxide towards the ETL and blocks holes from reaching TCO. Despite fairly large favourable VBO in all studied cases, in most cases the conduction band offset is undesirable. This is because of the small band gap of perovskites relative to metal oxides. Such CBO presents a potential barrier for injection of electrons into ETL conduction band. Additionally, this reduces device efficiency because it promotes charge recombination. For SnO_2 heterostructures with SMO and BMO a favourable band offset is obtained, as well as for TiO_2 heterostructures with SMO and BMO. Large difference in band gap between ZnO (3.47 eV) and strained CMO (0.78 eV), together with relatively large potential difference, led to unfavourable conduction band alignment at ZnO/CMO interface.

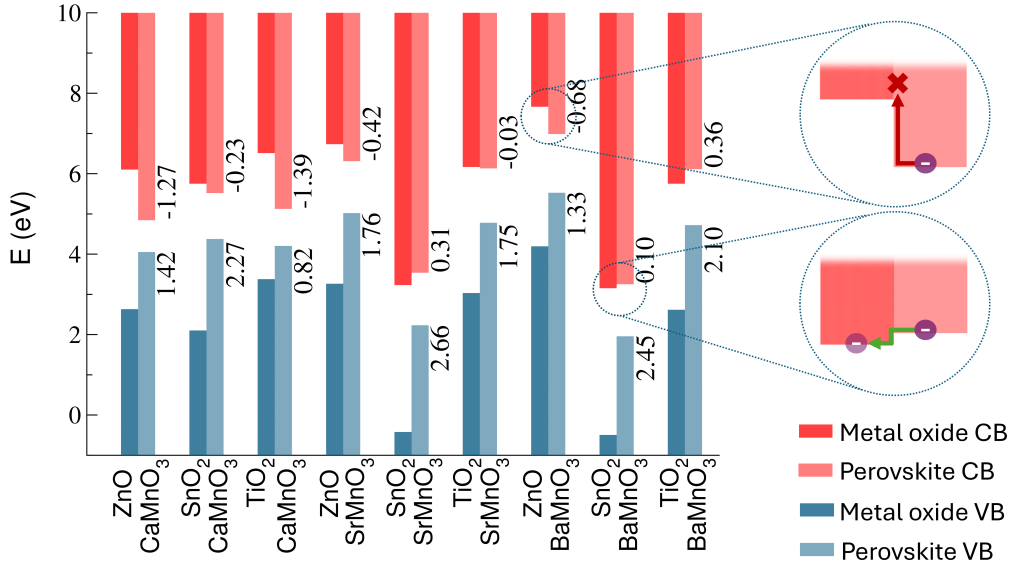

Figure 5.21: *Valence and conduction band offsets for nine studied heterostructures. Darker red bars signify metal oxide conduction bands, darker blue signifies metal oxide valence bands, light red signifies perovskite conduction bands, and light blue signifies perovskite valence bands. Numbers next to valence bands signify valence band offsets, and numbers next to conduction bands signify conduction band offsets. Positive value indicates that band edge of perovskite is above band edge of metal oxide, while negative value indicates that metal oxide band edge is above perovskite band edge.*

To deduce how relevant quantities that determine band offsets affect the values of band offsets, VBM and CBM positions, E_v and E_c, positions of electrostatic bulk potentials and potential differences are plotted in Figure 5.22. For SnO_2/CMO heterostructure the smallest potential difference was calculated, favouring desirable band alignment. However, the position of the VBM was lowered as a result of the large expansion of the out-of-plane lattice parameter. This resulted in a small difference between VBM and average potential, and led to unfavourable type I band offset, where VBM position of the perovskite is higher, but CBM position of CMO is below SnO_2 CBM. However, compared to conduction band offset (CBO) at ZnO/CMO interface, for SnO_2/CMO the CBO is much lower, calculated at -0.23 eV. In TiO_2/CMO, the potential difference is again significantly larger, comparable to that of ZnO/CMO (Figure 5.22 d)). Although among strained CMO models the largest difference between VBM and average potential is found for TiO_2 based heterostructure, this is insufficient to raise the CBM of CMO above TiO_2 CBM. This leads to type I band offset with larger CBO, similar to ZnO/CMO interface. It is obvious that to overcome the large difference in band gaps between metal oxides and perovksites, the VBM and average potential difference needs to be significantly higher for perovskites then it is for metal oxides. From Figure 5.22 it can be easily seen that metal oxides have, in general, higher average bulk potential compared to perovskites, while at the same time having lower VBM than of perovskites. While this does contribute towards obtaining favourable band alignment, in several cases it is insufficient and cannot raise CBM of perovskites above metal oxides CBM due to large potential difference of around 2 eV at the interface. This is the case in ZnO/SMO and ZnO/BMO heterostructures. For ZnO, the difference between VBM and average potential is around 1.75 eV. Compared with SMO and BMO, where this difference is around 5.94 eV for SMO and 6.26 eV for BMO, it is significantly lower. However, because of the largest potential differences out of all studied perovskites found in these heterostructures, calculated at -2.43 eV for ZnO/SMO and -3.17 eV for ZnO/BMO, the CBO is large, and hinders the injection of photoexcited electrons into ZnO conduction band. However, because of the large slope of the macroscopic potential across ZnO slab, the potential difference is not calculated as accurately as in other studied cases. Even when the error due to the slope of the macroscopic potential is taken into account, the type of conduction band offset remains the same in both cases, with only difference being the value of CBO and VBO. Therefore, the conclusion is that mainly due to the large potential difference at ZnO/SMO and ZnO/BMO heterostructures, the valence band offset is favourable for hole blocking. Conduction band offset is unfavourable, and would hinder the injection of electrons into ZnO conduction band. In SnO_2 heterostructures with SMO and BMO, lower potential difference is found relative to most other studied heterostructures, calculated at -1.18 eV for SnO_2/SMO, and -1.54 eV for SnO_2/BMO.

Furthermore, as larger difference between VBM and average bulk potential is found for SMO compared to CMO, and even larger for BMO, the resulting band offset type is type II (staggered). The staggered band offset of SnO_2/BMO heterostructure is highlighted in Figure 5.21 and shows how positive CBO aids in electron transport over the interface. TiO_2 heterostructures with SMO and BMO also showed favourable type II band offset. This is because the potential difference was not as high as in ZnO-based heterostructures due to much smaller charge transfer from metal oxide into perovskite interface layer. Errors introduced from surface dipole in SnO_2/SMO and SnO_2/BMO heterostructures, along with slope of the electrostatic potential across SnO_2 slab, lead to uncertainty in the predicted band alignment. Because interface trap states were also detected in these heterostructures, it can be concluded that they form an unfavourable case for charge dynamics.

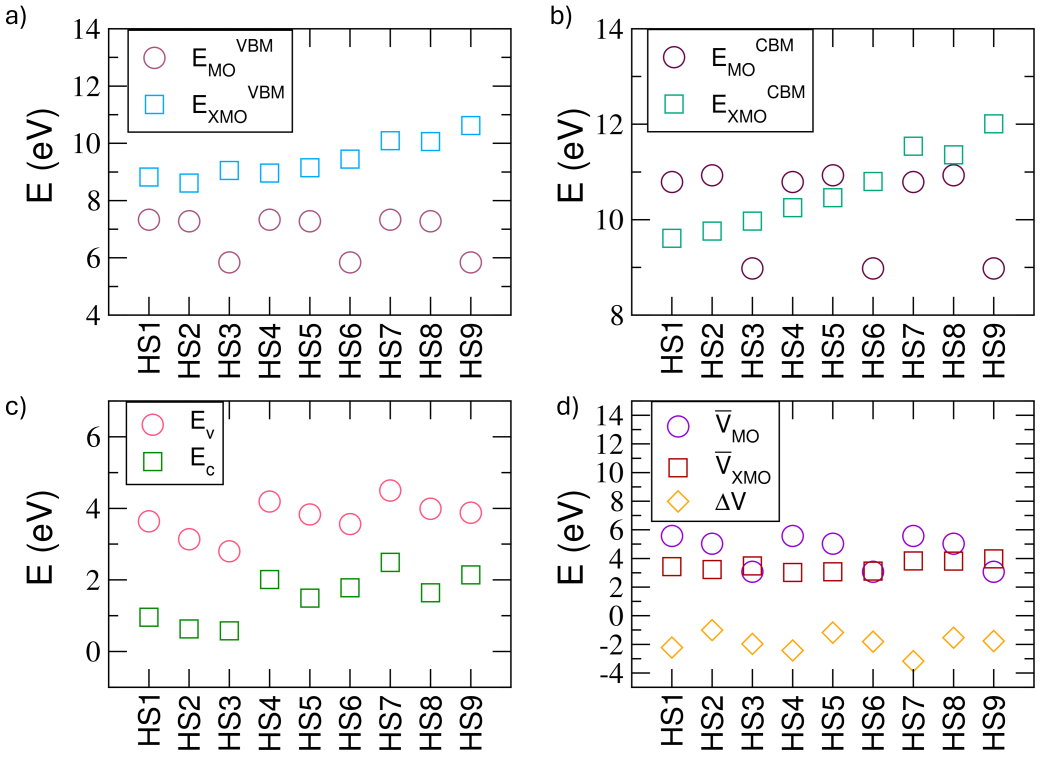

Figure 5.22: *a) Valence band maxima of perovskites (E_{XMO}^{VBM}) and of metal oxides (E_{MO}^{VBM}), b) conduction band minima of perovskites (E_{XMO}^{CBM}) and of metal oxides (E_{MO}^{CBM}), c) E_v and E_c, d) position of the average bulk potential of strained perovskites ($\bar{V}_{XMO}$), position of the average bulk potential of metal oxides ($\bar{V}_{MO}$), and potential differences of the bulk-like regions (ΔV) for each heterostructure. Heterostructures are denoted in the following order: HS1 - ZnO/$CaMnO_3$, HS2- SnO_2/$CaMnO_3$, HS3 - TiO_2/$CaMnO_3$, HS4 - ZnO/$SrMnO_3$, HS5 - SnO_2/$SrMnO_3$, HS6 - TiO_2/$SrMnO_3$, HS7 - ZnO/$BaMnO_3$, HS8 - SnO_2/$BaMnO_3$, HS9 - TiO_2/$BaMnO_3$*

Having negative CBO is undesirable, and interfaces with type I band offset generally do not have as efficient charge transfer over the interface compared to type II offset systems. However, when CBO is relatively low, still a substantial number of electrons that fill higher energy conduction band states could be transferred into ETL conduction band with sufficiently high charge carrier lifetime. This additionally depends on the interface trap density. If the excited electrons within higher conduction band energies are quickly and efficiently collected and transported into ETL conduction band, in the time frame smaller than the carrier lifetime, most of them do not undergo recombination. Furthermore, a small potential barrier was previously found to even be favourable, where PCE of PSC device was increased if small potential barrier was present. For up to 0.3 eV potential barrier between conduction band edge of perovskite and of metal oxide ETL the efficiency was increased [96, 97].

Band offset from local density of states

To further study how band edges of the bulk-like regions align, and to verify results of band offsets obtained with electrostatic potential, band offsets were additionally calculated using local density of states (LDOS) approach. Contributions to the total density of states from the ions belonging to an atomic layer are summed, hence providing an atomic layer resolved density of states. The LDOS plots are shown in Figure 5.23. For the studied cases where the slope of the electrostatic potential was observed, from LDOS steady positions of both VBM and CBM are predicted. However, slightly more noticeable are shifts of VBM in those cases, while the very edge has a constant position. Although in Figure 5.23 DOS edge can be observed at the energy where the line for VBM position was drawn, it is easily noticeable that VBM generally shifts upward in ZnO/SMO and ZnO/BMO, and downward in SnO_2/SMO, SnO_2/BMO and SnO_2/CMO. It is therefore predicted that valence bands bend more than conduction bands. This is valid for all studied cases where electric dipole was formed at the interface. However, it appears as the tails of conduction band edge which are visible in ZnO/SMO and ZnO/BMO heterostructures across ZnO bulk-like region are a result of the contribution from the surface states which has not fully vanished. Therefore, the conduction band edge is likely poluted by the residual contribution from the surface states, and it might not be a true conduction band edge. Based on LDOS, this led to lowering of potential barrier between conduction band edges at ZnO/SMO and ZnO/BMO heterostructures, calculated at 0.13 eV in ZnO/SMO and 0.15 eV at ZnO/BMO. True conduction band offset is likely much closer to the one calculated using average potential approach. To compare band offsets obtained using two different methods, Table 5.5 presents conduction and valence band offsets calculated from LDOS. With both methods the same types of band offsets are predicted. The values of calculated

band offsets differ in some cases. This can be the result of several factors. One of the reasons is LDOS predicted lower CBM position, which as previously stated appears to be a result of non-vanished surface states contribution. This effect cannot be predicted with electrostatic potential approach, as in that approach CBO is calculate from bulk band gaps. Additionally, from LDOS method it is typically more difficult to calculate exact band edge positions, mainly due to the use of smearing (electronic temperature), which has to be used for the projection of density of states on atomic orbitals. By lowering the smearing value a more precise band edge positions can be calculated, but it leads to a highly oscillating DOS function. Band offsets can also differ due to used value of average potential across metal oxide slab in the electrostatic potential approach. However, generally a good agreement is found for band offsets calculated with two methods. What can additionally be observed is that in ZnO/SMO and ZnO/BMO heterostructures mid-gap dispersive states emerge at ZnO surface, as was previously confirmed from probability density calculations. LDOS also confirms existence of interface states in all cases where they were predicted using probability density calculations. Same follows for observed surfaces states. All studied heterostructure have a visible interface gap, meaning that the formation of localized interface states did not lead to a metallic interface.

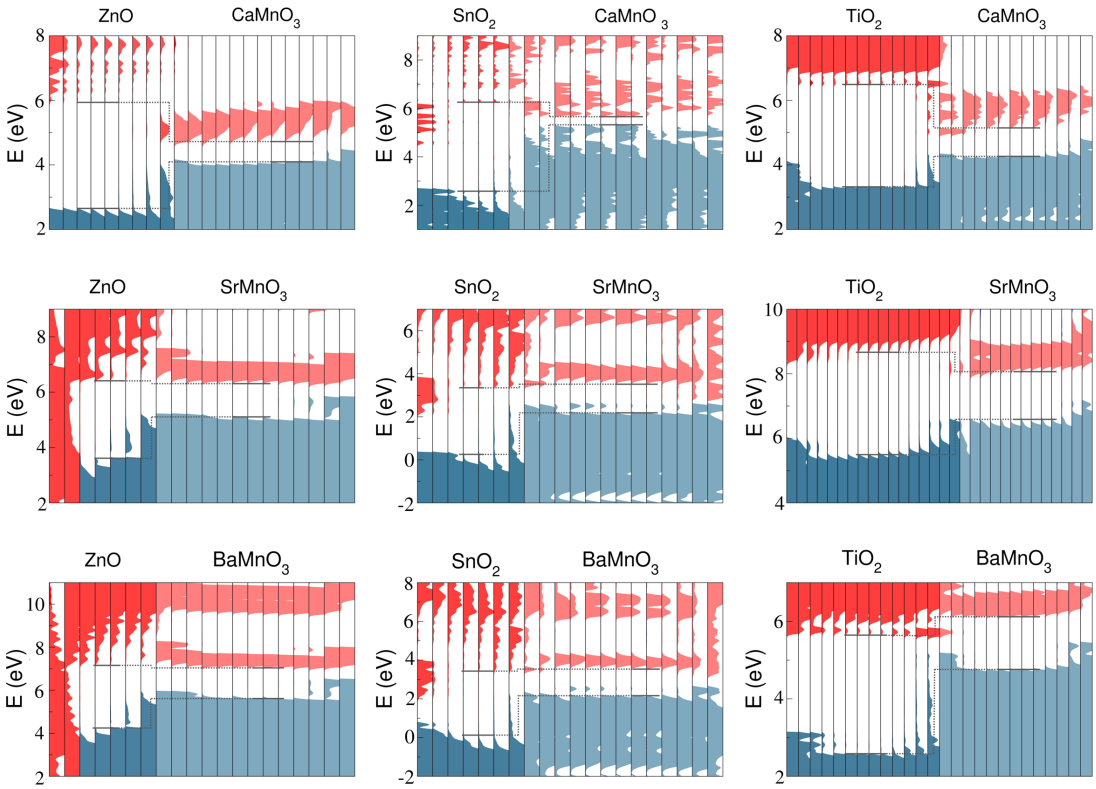

Figure 5.23: *Local density of states plots for nine studied heterostructures. Metal oxide valence bands are colored darker blue, metal oxide conduction bands are colored darker red, perovskite valence bands are colored lighter blue, and perovskite conduction bands are colored lighter red. Dark grey lines display how band edges of the bulk-like regions align.*

Table 5.5: *Conduction band offsets and valence band offsets calculated from local density of states plots for nine studied heterostructures. Negative value indicates that perovskite band edge is below metal oxide band edge.*

	ZnO/ $CaMnO_3$	SnO_2/ $CaMnO_3$	TiO_2/ $CaMnO_3$	ZnO/ $SrMnO_3$	SnO_2/ $SrMnO_3$	TiO_2/ $SrMnO_3$	ZnO/ $BaMnO_3$	SnO_2/ $BaMnO_3$	TiO_2/ $BaMnO_3$
CBO (eV)	-1.28	-0.62	-1.33	-0.13	0.10	-0.19	-0.15	0.09	0.43
VBO (eV)	1.42	2.68	0.94	1.46	2.26	1.57	1.46	2.18	2.19

Conclusion

The research conducted within this thesis included theoretical ground-state investigation of the structural and electronic properties of $CaMnO_3$, $SrMnO_3$ and $BaMnO_3$ perovskites which are of interest for their application in perovskite-based solar cells. The study showed optimal band gaps of investigated perovskites, ranging from 0.92 eV to 1.44 eV, in the range appropriate for optical absorption and high efficiency solar cell devices. The study of their optical properties showed high absorption throughout the visible range, and good optical matching with metal oxides commonly used as electron transport layers. These results point toward efficient light absorption within perovskites. Further experiments are required to complement these results with insights unavailable from *ab initio* theory. Main part of the research included investigation of interface properties of manganese perovskites with commonly used metal oxide electron transport layers, ZnO, SnO_2 and TiO_2. Metal oxide electron transport layers showed large band gaps, above 3 eV, and high curvature of conduction bands, with effective mass between $0.18m_0$ and $0.68m_0$, in a good agreement with previous experimental and theoretical studies. By using density functional theory relevant properties for charge dynamics across the interfaces were investigated, with main focus on the band offsets. To form stable interfaces, surface orientations of nine studied heterostructures were chosen based on the lowest achievable lattice mismatch. This should ensure higher stability, and low density of defects which can form under applied strain. To comply with low lattice mismatch condition, and because pseudomorphic growth of perovskites on metal oxides was assumed, perovskites were strained. Because of this, strained perovskite models were studied to deduce how strain impacts valence band edge positions, and their difference with average potential. Additionally, strain effects on effective mass was investigated. They showed small changes of band edge curvature for $CaMnO_3$ under smaller strain, while $SrMnO_3$ and $BaMnO_3$ showed significant conduction band flattening even for small imposed strain. This indicates increased electron effective mass in $SrMnO_3$ and $BaMnO_3$. To accurately represent the surface interactions at heterovalent interfaces, all supercell models were relaxed using robust theoretical algorithms. Atomic displacements were mainly restricted to several atomic layers closest to the interface. The study of charge dynamics properties was enabled by a sufficiently

large heterostructure models, which demonstrated bulk-like behaviour far away from the interface. Charge density difference isosurfaces revealed charge transfer between oxygen anions and metal oxide cations at the interface, with additional charge accumulation along the oxygen-metal oxide bond, indicating the formation of interface bonds of mixed ionic and covalent character. Formed bonds indicate the stability of the studied interfaces. In most heterostructures charge transfer was predicted from metal oxide surface to the perovskite surface. Only SnO_2/$SrMnO_3$ and SnO_2/$BaMnO_3$ heterostructures showed charge transfer from perovskite surface to metal oxide surface, due to significant charge transfer from manganese to oxygen across the interface. This led to sufficiently low potential difference. This, in turn, resulted in the formation of type II band offset. However, despite the predicted type II band offset, uncertainties were introduced due to the surface dipole, and due to the slope of the electrostatic potential caused by interface dipole. In most cases, type I band offset was obtained, where valence band offset is favourable, and leads to hole blocking at perovskite/metal oxide interface. It also leads to electron blocking, as potential barrier is formed due to unfavourable conduction band offset. In general, in studied cases where type I offset occurred it is mainly caused by a larger charge transfer from metal oxide to perovskite, which leads to the increase of potential difference. In TiO_2 heterostructures with $SrMnO_3$ and $BaMnO_3$ type II band offset was obtained, which was attributed to much smaller charge transfer from metal oxide surface to perovskite surface, which led to smaller potential difference compared to ZnO-based heterostructures. This was sufficient to enable the formation of favourable type II band offset. In several interfaces electric dipoles were formed, resulting in the slope of the electrostatic potential across metal oxide slabs. The slope of the electrostatic potential led to uncertainties in potential difference calculation, most significantly at ZnO/$SrMnO_3$ and ZnO/$BaMnO_3$ interfaces, but also at SnO_2 heterostructures with $SrMnO_3$ and $BaMnO_3$. The error due to slope of the macroscopic potential does not change the type of band offset in ZnO heterostructures, but could lead to a change of band offset type in SnO_2 heterostructures. Additionally, band structures of SnO_2 heterostructures with $SrMnO_3$ showed the formation of several mid-gap states which typically act as recombination centers for electrons. Interface states were also found at SnO_2/$BaMnO_3$, but they were formed as shallow electron and hole trap states. Due to small calculated conduction band offset, detected electron trap states can negatively affect device efficiency. It was shown that although shallow, electron trap state forms below conduction band edge of SnO_2, which is unfavourable for optimal device operation. Additionally, low lattice mismatch between $SrMnO_3$ and $BaMnO_3$ indicates the possibility to grow these heterostructures epitaxially without possible dislocation defects. To further acknowledge these materials as good candidates for perovskite solar cell applications requires additional studies based on the macroscopic models, as well as

experimental measurements of relevant quantities, such as defect density, charge carrier lifetime, etc.

There are several possible routes which can be taken to gain more insights on these materials and their applications in perovskite solar cells. Different surface orientations can be considered in several cases. However, there are not many options for this, as considering other orientations would in general increase lattice mismatch. Other approach can be the investigation of different surface terminations, but again, there are very limited additional options that would be able to create stable interfaces. A possibly good direction could be to investigate $A-$site cation mixing. Combination of strontium and barium could lead to favourable properties, due to change in lattice constants which could lead to even lower lattice mismatch with neighboring electron transport layer. It could also indirectly impact energy band edge positions through the change in MnO_6 bond length and bond angle. This could lead to more favourable electron effective mass, as it was seen that both $SrMnO_3$ and $BaMnO_3$ suffer from large electron effective mass increase even for small imposed strain. Non-stoichiometric perovskite approach is also available, which would alter the interaction at the interfaces. This approach could be highly successful in ZnO/$SrMnO_3$ and ZnO/$BaMnO_3$ heterostructures. For instance, it could be applied to balance the charge density of polar interface, and reduce the slope of the electrostatic potential. It could possibly lead to a reduced potential difference between ZnO and $SrMnO_3$ and $BaMnO_3$, which could result in favourable conduction band offset.

To overcome the unfavourable conduction band offset, several things can be implemented to improve it. Strain engineering can be effectively used to shift VBM and CBM position, and increase the band gap of the perovskites. To be able to determine how different types and magnitudes of strain would affect the properties of the perovskites studied within this thesis, a comprehensive and systematic investigation of strain effects is required. Additional possibility is to include cation mixing as an alternative approach. The mixing of cations impacts lattice constants, band gaps, and VBM and CBM position. This can then be very effectively used to tune lattice parameters to further lower the mismatch, making more stable and easier to grow heterostructures, tune band gap for optimal optical absorption, and tune the positions of VBM and CBM. This could even be implemented for SMO and BMO, as SMO typically undergoes tensile strain to accommodate for lattice mismatch with studied metal oxides, and BMO is compressed. By possibly combining strontium and barium cations in various fractions in the $Ba_xSr_{1-x}MnO_3$ form, the band gap should remain in the desirable range, as the exchange of cations has very little effect on band gap, but would lead to change in lattice constants, which could work in favour of lower lattice mismatch with studied metal oxide ETL's. Additionally, this would somewhat alter the position of VBM and CBM, which could also work in favour

of obtaining desirable conduction band offset. Furthermore, as this study did not include investigation of different surface orientations and terminations, this approach could also be implemented to try to find the optimal match that could lead to beneficial properties for PSC applications. Finally, there are two additional approaches that could be taken: the study of non-stoichiometric perovskites, to find optimal interface structure that would benefit favourable band alignment, and using additional interface buffer layers which could be used to alter the band alignment for optimal device operation, but would lead to more complex device architecture. While ground-state DFT simulations offer valuable insights into charge dynamics at heterostructure interfaces, they provide an incomplete perspective. A comprehensive evaluation of $XMnO_3$ perovskites for photovoltaic applications requires further investigation into critical factors such as carrier lifetimes and exciton binding energies.

Appendix A

Computational details and convergence tests

To conduct density functional theory calculations, QuantumEspresso open-source code was used [98]. This approach uses pseudopotentials as described in the second chapter. The pseudopotentials used for all studied compounds were norm-conserving. The used pseudopotentials were taken from the QuantumEspresso website and were obtained through a procedure as described by D.R. Hamann [99]. The pseudopotentials had the valence electron configuration shown in Table 5.6.

Table 5.6: *Valence electron configuration within used pseudopotentials for all used chemical elements.*

Chemical element	Valence electron configuration
O	$2s^2 2p^4$
Ca	$3s^2 3p^6 4s^2$
Sr	$4s^2 4p^6 5s^2$
Ba	$5s^2 5p^6 6s^2$
Ti	$3s^2 3p^6 4s^2 3d^2$
Sn	$5s^2 4d^{10} 5p^2$
Mn	$3s^2 3p^6 4s^2 3d^5$
Zn	$3s^2 3p^6 4s^2 3d^{10}$

To ensure high accuracy of the results, while maintaining reasonable computational cost, the convergence tests for several quantities were performed. For the expansion of wave function in the plane-wave basis set, an energy cutoff is typically set, which means that only plane-waves which have kinetic energy below the set threshold are considered. To obtain energy cutoff threshold, E_{cut} parameter value was increased in increments from 10 Ry to

100 Ry for bulk materials, and from 60 Ry to 120 Ry for heterostructure supercell models. The total energy convergence threshold for supercells is usually set at 1 mRy/atom. Further, in DFT integration over the Brillouine zone is usually approximated by the summation over discrete k-point grid. Converged energy cutoffs and k-point grids for bulk systems are shown in Table 5.7 For heterostructures, unit cell dimension in the direction of the growth of the heterostructure is much larger than the cell parameters perpendicular to the interface. Therefore, its corresponding reciprocal space dimension is very small. Because of this, typically only calculation in the middle of reciprocal cell is required. This means that for the k-point mesh, in the direction of the growth of the heterostructure only one k-point was used. For optical properties of the perovskites, a denser k-point grid of $18\times18\times18$ was used. To ensure that the outer surfaces of the supercell model interacting does not significantly impact total energy of the system, convergence test was also conducted for the vacuum thickness. Thus, for each supercell model, vacuum thickness was initially set at 10Å and increased up to 45Å to find the converged vacuum thickness. Converged energy cutoffs, k-point grids, and vacuum thicknesses are shown in Table 5.8.

Table 5.7: *Converged kinetic energy cutoff values and k-point meshes for all studied bulk systems.*

	E_{cut} (Ry)	k-point grid
ZnO	80	$8\times8\times8$
SnO_2	90	$6\times6\times6$
TiO_2	110	$8\times8\times8$
$CaMnO_3$	110	$4\times4\times4$
$SrMnO_3$	100	$4\times4\times4$
$BaMnO_3$	150	$4\times4\times4$

Table 5.8: *Converged kinetic energy cutoff value, converged k-point mesh and converged vacuum thickness for each of the studied heterostructures.*

Heterostructure	E_{cut} (Ry)	k-point grid	Vacuum thickness (Å)
$ZnO/CaMnO_3$	110	6×1×6	20
$SnO_2/CaMnO_3$	110	4×4×1	20
$TiO_2/CaMnO_3$	110	4×4×1	20
$ZnO/SrMnO_3$	110	8×8×1	20
$SnO_2/SrMnO_3$	110	4×4×1	35
$TiO_2/SrMnO_3$	110	4×1×4	20
$ZnO/BaMnO_3$	110	8×8×1	20
$SnO_2/BaMnO_3$	110	4×4×1	40
$TiO_2/BaMnO_3$	110	4×1×4	20

The linear response approach which was used to find Hubbard U values for perovskites requires convergence test for the q-point grid with respect to Hubbard U value. The converged q-point grids are specified in Table 5.9 For linear response calculations previously converged energy cutoff was used, as well as converged k-point grid. To find Hubbard U values, several iterations of calculations were performed, which include initializing the Hubbard U procedure by initially setting U parameter value to 10^{-4} eV and performing SCF calculation. Then, the hp.x code performs linear response calculation by displacing atoms on which Hubbard U correction was initially set, and calculating the response to these perturbations. From this a new Hubbard U value was obtained, which was used to relax atomic coordinates and unit cell. Afterwards, the whole procedure is repeated with new Hubbard U parameter. When linear response calculation gives out Hubbard U value which agrees to within 0.1 eV with U value set in previous iteration, the convergence of Hubbard U parameter is achieved. This U value is then further used for all other calculations. The converged Hubbard U values are shown in Table 5.9. For metal oxides, linear response approach has issues with numerical instability when metal oxides contain fully occupied d orbitals on which the correction is meant to be applied to [44]. As both Zn and Sn contain fully occupied d orbitals, the linear response approach could not be implemented for ZnO and SnO_2. For TiO_2, linear response approach was tested, which resulted in underestimated band gap of 2.60 eV when the correction was applied only on titanium 3d states, and overestimated at 3.90 eV when it was applied to both titanium 3d

and oxygen 2p states. Very similar results were obtained for TiO_2 in a previous study by Kirchner-Hall et al. [100]. Due to the large discrepancy in the band gap obtained using linear response obtained U value compared to experimentally obtained band gap, semi-empirical approach was implemented for TiO_2 as well. For all metal oxides, therefore, the used Hubbard U parameter value was the one which gave band gap value very close to experimentally measured value. Hubbard U values are shown in Table 5.9.

Table 5.9: *Hubbard U values, orbitals upon which the corrections were used, q-point grid used in linear reponse approach, and method which was used to obtain Hubbard U value. SE signifies semi-empirical approach, and LR signifies linear response approach.*

	ZnO	SnO_2	TiO_2	$CaMnO_3$	$SrMnO_3$	$BaMnO_3$
Hubbard U	9.00, 6.50	6.80	4.5, 3.0	5.91	5.75	5.82
Manifold	Zn-3d, O-2p	O-2p	Ti-3d	Mn-3d	Mn-3d	Mn-3d
q-point grid	-	-	-	4×4×4	4×4×4	2×2×2
Method	SE	SE	SE	LR	LR	LR

Appendix B

Dipole correction for small surface dipole

To show the effects of small surface dipole, electrostatic potentials were plotted for ZnO/CMO heterostructure, and are shown in Figure 5.24. Very slight slope of the vacuum potential is found in this case. General overlap of both plane-averaged and macroscopic average of the electrostatic potential confirms very little contribution of surface dipole to the behavior of the electrostatic potential and its lineup. Correction of the surface dipole is confirmed by the vacuum potential, showing two separate constant value regions. While it can be expected that the response of ZnO charge density to the dipole correction would be more severe in ZnO/SMO and ZnO/BMO heterostructures, due to small surface dipole magnitude in those heterostructures it can be assumed that the contribution of the dipole correction would be insignificant. However, for the two cases where the largest surface dipole was found, SnO_2/SMO and SnO_2/BMO, given the largest error introduced due to surface dipole, one has to keep in mind that it can affect the band alignment if the band edge offsets are sufficiently small and fall in the range of introduced error from surface dipole, while for small surface dipole there is no observable difference in potential lineup with and without dipole correction.

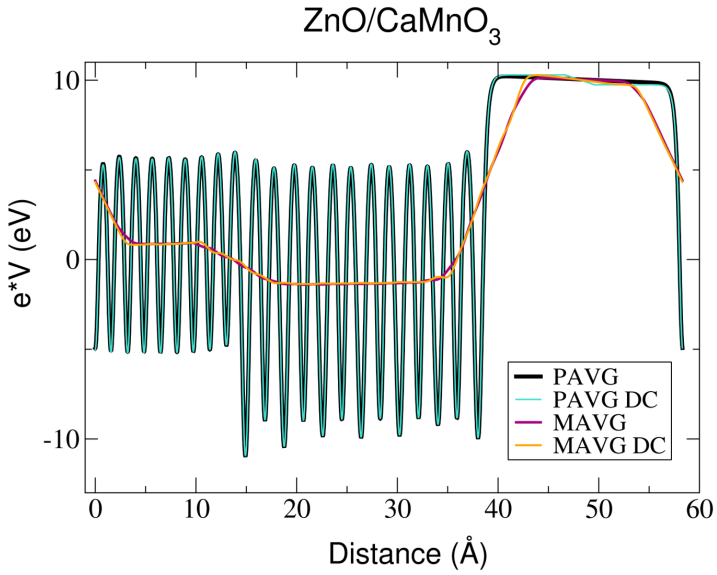

Figure 5.24: *Plane average and macroscopic average of the electrostatic potential of $ZnO/CaMnO_3$ for dipole corrected and non-dipole corrected case. Plot shows nearly complete overlap of potentials for dipole corrected and non-dipole corrected case. PAVG represents plane-averaged electrostatic potential without dipole correction, PAVG DC represents plane-averaged electrostatic potential with dipole correction, MAVG represents macroscopic average of the electrostatic potential without dipole correction, and MAVG DC represents macroscopic average of the electrostatic potential with dipole correction applied.*

References

[1] A. Kojima et al. “Organometal halide perovskites as visible-light sensitizers for photovoltaic cells”. In: *Journal of the american chemical society* 131.17 (2009), pp. 6050–6051.

[2] M. A. Green et al. “Solar cell efficiency tables (Version 64)”. In: *Progress in Photovoltaics: Research and Applications* 32.7 (2024), pp. 425–441. DOI: https://doi.org/10.1002/pip.3831. eprint: https://onlinelibrary.wiley.com/doi/pdf/10.1002/pip.3831. URL: https://onlinelibrary.wiley.com/doi/abs/10.1002/pip.3831.

[3] W. R. Mateker and M. D. McGehee. “Progress in Understanding Degradation Mechanisms and Improving Stability in Organic Photovoltaics”. In: *Advanced Materials* 29.10 (2017), p. 1603940. DOI: https://doi.org/10.1002/adma.201603940. eprint: https://advanced.onlinelibrary.wiley.com/doi/pdf/10.1002/adma.201603940. URL: https://advanced.onlinelibrary.wiley.com/doi/abs/10.1002/adma.201603940.

[4] T. Seyisi et al. “Major challenges for commercialization of perovskite solar cells: A critical review”. In: *Energy Reports* 13 (2025), pp. 1400–1415. ISSN: 2352-4847. DOI: https://doi.org/10.1016/j.egyr.2025.01.019. URL: https://www.sciencedirect.com/science/article/pii/S2352484725000198.

[5] J. Huang et al. “Impact of H2O on organic–inorganic hybrid perovskite solar cells”. In: *Energy Environ. Sci.* 10 (11 2017), pp. 2284–2311. DOI: 10.1039/C7EE01674C. URL: http://dx.doi.org/10.1039/C7EE01674C.

[6] W. Xiang, S. (Liu, and W. Tress. “A review on the stability of inorganic metal halide perovskites: challenges and opportunities for stable solar cells”. In: *Energy Environ. Sci.* 14 (4 2021), pp. 2090–2113. DOI: 10.1039/D1EE00157D. URL: http://dx.doi.org/10.1039/D1EE00157D.

[7] W. Yao Zhun and and S. (Liu. “Stability of the CsPbI3 perovskite: from fundamentals to improvements”. In: *J. Mater. Chem. A* 9 (18 2021), pp. 11124–11144. DOI: 10.1039/D1TA01252E. URL: http://dx.doi.org/10.1039/D1TA01252E.

[8] J. Zhang et al. “All-Inorganic CsPbX3 Perovskite Solar Cells: Progress and Prospects”. In: *Angewandte Chemie International Edition* 58.44 (2019), pp. 15596–15618. DOI: https://doi.org/10.1002/anie.201901081. eprint: https://onlinelibrary.wiley.com/doi/pdf/10.1002/anie.201901081. URL: https://onlinelibrary.wiley.com/doi/abs/10.1002/anie.201901081.

[9] S. Xu et al. “Research Progress of Cs-Based All-Inorganic Perovskite Solar Cells”. In: *Energies* 17.11 (2024). ISSN: 1996-1073. DOI: 10.3390/en17112671. URL: https://www.mdpi.com/1996-1073/17/11/2671.

[10] S. Sanchez et al. “Efficient and Stable Inorganic Perovskite Solar Cells Manufactured by Pulsed Flash Infrared Annealing”. In: *Advanced Energy Materials* 8.30 (2018), p. 1802060. DOI: https://doi.org/10.1002/aenm.201802060. eprint: https://advanced.onlinelibrary.wiley.com/doi/pdf/10.1002/aenm.201802060. URL: https://advanced.onlinelibrary.wiley.com/doi/abs/10.1002/aenm.201802060.

[11] L. A. Frolova et al. “Exploring the Effects of the Pb2+ Substitution in MAPbI3 on the Photovoltaic Performance of the Hybrid Perovskite Solar Cells”. In: *The Journal of Physical Chemistry Letters* 7.21 (2016), pp. 4353–4357. DOI: 10.1021/acs.jpclett.6b02122. eprint: https://doi.org/10.1021/acs.jpclett.6b02122. URL: https://doi.org/10.1021/acs.jpclett.6b02122.

[12] P. Schulz. “Interface Design for Metal Halide Perovskite Solar Cells”. In: *ACS Energy Letters* 3.6 (2018), pp. 1287–1293. DOI: 10.1021/acsenergylett.8b00404. eprint: https://doi.org/10.1021/acsenergylett.8b00404. URL: https://doi.org/10.1021/acsenergylett.8b00404.

[13] C. Eames et al. “Ionic transport in hybrid lead iodide perovskite solar cells”. In: *Nature communications* 6.1 (2015), p. 7497.

[14] H. Kronmüller and S. Parkin. *Handbook of Magnetism and Advanced Magnetic Materials: Spintronics and magnetoelectronics*. Handbook of Magnetism and Advanced Magnetic Materials. John Wiley & Sons, 2007. ISBN: 9780470022177.

[15] J. Noh et al. “Chemical Management for Colorful, Efficient, and Stable Inorganic–Organic Hybrid Nanostructured Solar Cells”. In: *Nano letters* 13 (Mar. 2013). DOI: 10.1021/nl400349b.

[16] F. Igbari, M. Bilal, and Z. Li. “Strategies for performance and stability advancement in multicomponent perovskite photovoltaics”. In: *J. Mater. Chem. A* 13 (39 2025), pp. 32964–33011. DOI: 10.1039/D5TA04375A. URL: http://dx.doi.org/10.1039/D5TA04375A.

[17] R. Tirawat et al. “Measuring metal halide perovskite single cell degradation consistent with module-based conditions”. In: *Sustainable Energy Fuels* 8 (3 2024), pp. 546–553. DOI: 10.1039/D3SE01268A. URL: http://dx.doi.org/10.1039/D3SE01268A.

[18] Y. Zhao et al. “Discovery of temperature-induced stability reversal in perovskites using high-throughput robotic learning”. In: *Nature Communications* 12 (Apr. 2021), p. 2191. DOI: 10.1038/s41467-021-22472-x.

[19] Y. Wang et al. “Lattice Mismatch at the Heterojunction of Perovskite Solar Cells”. In: *Angewandte Chemie International Edition* 63.29 (2024), e202405878. DOI: https://doi.org/10.1002/anie.202405878. eprint: https://onlinelibrary.wiley.com/doi/pdf/10.1002/anie.202405878. URL: https://onlinelibrary.wiley.com/doi/abs/10.1002/anie.202405878.

[20] M. Eshete and G. Di Liberto. “Modeling heterojunctions: a computational chemistry perspective”. In: *RSC Appl. Interfaces* 2 (4 2025), pp. 897–916. DOI: 10.1039/D5LF00104H. URL: http://dx.doi.org/10.1039/D5LF00104H.

[21] Y. Li et al. “Recent Progress of Critical Interface Engineering for Highly Efficient and Stable Perovskite Solar Cells”. In: *Advanced Energy Materials* 12.5 (2022), p. 2102730. DOI: https://doi.org/10.1002/aenm.202102730. eprint: https://advanced.onlinelibrary.wiley.com/doi/pdf/10.1002/aenm.202102730. URL: https://advanced.onlinelibrary.wiley.com/doi/abs/10.1002/aenm.202102730.

[22] S. Shao and M. A. Loi. “The Role of the Interfaces in Perovskite Solar Cells”. In: *Advanced Materials Interfaces* 7.1 (2020), p. 1901469. DOI: https://doi.org/10.1002/admi.201901469. eprint: https://advanced.onlinelibrary.wiley.com/doi/pdf/10.1002/admi.201901469. URL: https://advanced.onlinelibrary.wiley.com/doi/abs/10.1002/admi.201901469.

[23] Y. Yu, J. Xia, and Y. Liang. “Basic understanding of perovskite solar cells and passivation mechanism”. In: *AIP Advances* 12.5 (May 2022), p. 055307. ISSN: 2158-3226. DOI: 10.1063/5.0058441. eprint: https://pubs.aip.org/aip/adv/article-pdf/doi/10.1063/5.0058441/16468170/055307_1_online.pdf. URL: https://doi.org/10.1063/5.0058441.

[24] J. Y. Kim et al. “High-efficiency perovskite solar cells”. In: *Chemical reviews* 120.15 (2020), pp. 7867–7918.

[25] E. Mosconi, E. Ronca, and F. De Angelis. “First-Principles Investigation of the TiO2/Organohalide Perovskites Interface: The Role of Interfacial Chlorine”. In: *The Journal of Physical Chemistry Letters* 5.15 (2014). PMID: 26277953, pp. 2619–2625. DOI: 10.1021/jz501127k. eprint: https://doi.org/10.1021/jz501127k. URL: https://doi.org/10.1021/jz501127k.

[26] E. W. Welch et al. “A density functional theory study on the interface stability between CsPbBr3 and CuI”. In: *AIP Advances* 10.8 (Aug. 2020), p. 085023. ISSN: 2158-3226. DOI: 10.1063/5.0018925. eprint: https://pubs.aip.org/aip/adv/article-pdf/doi/10.1063/5.0018925/12977370/085023_1_online.pdf. URL: https://doi.org/10.1063/5.0018925.

[27] S. Sant, M. Luisier, and A. Schenk. “Density functional theory based analysis of the origin of traps at the InAs/Si hetero-interface”. In: *Applied Physics Letters* 111.24 (2017).

[28] I. Kovač et al. “Charge carrier dynamics across the metal oxide/BaTiO3 interfaces toward photovoltaic applications from the theoretical perspective”. In: *Surfaces and interfaces* 39 (2023), p. 102974.

[29] K. Pandey et al. “Improving electron transport in the hybrid perovskite solar cells using CaMnO3-based buffer layer”. In: *Nano Energy* 45 (2018), pp. 287–297.

[30] P. Zhao et al. “Calcium manganate: A promising candidate as buffer layer for hybrid halide perovskite photovoltaic-thermoelectric systems”. In: *Journal of Applied Physics* 116.19 (Nov. 2014), p. 194901. ISSN: 0021-8979. DOI: 10.1063/1.4901636. eprint: https://pubs.aip.org/aip/jap/article-pdf/doi/10.1063/1.4901636/13260466/194901_1_online.pdf. URL: https://doi.org/10.1063/1.4901636.

[31] M. Mužević et al. “Potential of AMnO3 (A= Ca, Sr, Ba, La) as active layer in inorganic perovskite solar cells”. In: *ChemPhysChem* 24.9 (2023), e202200837.

[32] I. Kovač et al. “Insights into the charge dynamics at metal oxide/manganate perovskite interfaces from density functional theory”. In: *Applied Surface Science* (2026), p. 166497. ISSN: 0169-4332. DOI: https://doi.org/10.1016/j.apsusc.2026.166497. URL: https://www.sciencedirect.com/science/article/pii/S0169433226007014.

[33] L. H. Thomas. “The calculation of atomic fields”. In: *Mathematical Proceedings of the Cambridge Philosophical Society* 23.5 (1927). DOI: 10.1017/S0305004100011683.

[34] E. Fermi. “Un metodo statistico per la determinazione di alcune priorieta dell’atome”. In: *Rend. Accad. Naz. Lincei* 6.602-607 (1927), p. 32.

[35] P. Hohenberg and W. Kohn. “Inhomogeneous Electron Gas”. In: *Phys. Rev.* 136 (3B 1964), B864–B871. DOI: 10.1103/PhysRev.136.B864. URL: https://link.aps.org/doi/10.1103/PhysRev.136.B864.

[36] W. Kohn and L. J. Sham. “Self-Consistent Equations Including Exchange and Correlation Effects”. In: *Phys. Rev.* 140 (4A 1965), A1133–A1138. DOI: 10.1103/PhysRev.140.A1133. URL: https://link.aps.org/doi/10.1103/PhysRev.140.A1133.

[37] A. J. Cohen, P. Mori-Sánchez, and W. Yang. “Challenges for Density Functional Theory”. In: *Chemical Reviews* 112.1 (2012). PMID: 22191548, pp. 289–320. DOI: 10.1021/cr200107z. eprint: https://doi.org/10.1021/cr200107z. URL: https://doi.org/10.1021/cr200107z.

[38] M. C. Payne et al. “Iterative minimization techniques for ab initio total-energy calculations: molecular dynamics and conjugate gradients”. In: *Rev. Mod. Phys.* 64 (4 1992), pp. 1045–1097. DOI: 10.1103/RevModPhys.64.1045. URL: https://link.aps.org/doi/10.1103/RevModPhys.64.1045.

[39] R. P. Feynman. “Forces in Molecules”. In: *Phys. Rev.* 56 (4 1939), pp. 340–343. DOI: 10.1103/PhysRev.56.340. URL: https://link.aps.org/doi/10.1103/PhysRev.56.340.

[40] C. G. BROYDEN. “The Convergence of a Class of Double-rank Minimization Algorithms 1. General Considerations”. In: *IMA Journal of Applied Mathematics* 6.1 (Mar. 1970), pp. 76–90. ISSN: 0272-4960. DOI: 10.1093/imamat/6.1.76. eprint: https://academic.oup.com/imamat/article-pdf/6/1/76/2233756/6-1-76.pdf. URL: https://doi.org/10.1093/imamat/6.1.76.

[41] I. Timrov, N. Marzari, and M. Cococcioni. “Hubbard parameters from density-functional perturbation theory”. In: *Phys. Rev. B* 98 (8 2018), p. 085127. DOI: 10.1103/PhysRevB.98.085127. URL: https://link.aps.org/doi/10.1103/PhysRevB.98.085127.

[42] M. Cococcioni and S. de Gironcoli. “Linear response approach to the calculation of the effective interaction parameters in the LDA + U method”. In: *Phys. Rev. B* 71 (3 2005), p. 035105. DOI: 10.1103/PhysRevB.71.035105. URL: https://link.aps.org/doi/10.1103/PhysRevB.71.035105.

[43] E. M. Flores et al. “Optical and structural investigation of ZnO@ ZnS core–shell nanostructures”. In: *Materials Chemistry and Physics* 173 (2016), pp. 347–354.

[44] K. Yu and E. A. Carter. “Communication: Comparing ab initio methods of obtaining effective U parameters for closed-shell materials”. In: *The Journal of Chemical Physics* 140.12 (2014), p. 121105. ISSN: 0021-9606. DOI: 10.1063/1.4869718. eprint: https://pubs.aip.org/aip/jcp/article-pdf/doi/10.1063/1.4869718/13234368/121105_1_online.pdf. URL: https://doi.org/10.1063/1.4869718.

[45] H. J. Kulik and N. Marzari. “Systematic study of first-row transition-metal diatomic molecules: A self-consistent DFT+ U approach”. In: *The Journal of chemical physics* 133.11 (2010).

[46] S.-j. Hu et al. “First-principles LDA + U calculations of the Co-doped ZnO magnetic semiconductor”. In: *Phys. Rev. B* 73 (24 2006), p. 245205. DOI: 10.1103/PhysRevB.73.245205. URL: https://link.aps.org/doi/10.1103/PhysRevB.73.245205.

[47] H. Kuzmany. *Solid-state spectroscopy: an introduction*. Springer Science & Business Media, 2009.

[48] F. Zheng, J. Tao, and A. M. Rappe. “Frequency-dependent dielectric function of semiconductors with application to physisorption”. In: *Phys. Rev. B* 95 (3 2017), p. 035203. DOI: 10.1103/PhysRevB.95.035203. URL: https://link.aps.org/doi/10.1103/PhysRevB.95.035203.

[49] M. Peressi, N. Binggeli, and A. Baldereschi. “Band engineering at interfaces: theory and numerical experiments”. In: *Journal of Physics D: Applied Physics* 31.11 (1998), p. 1273. DOI: 10.1088/0022-3727/31/11/002. URL: https://doi.org/10.1088/0022-3727/31/11/002.

[50] A. Baldereschi, S. Baroni, and R. Resta. “Band Offsets in Lattice-Matched Heterojunctions: A Model and First-Principles Calculations for GaAs/AlAs”. In: *Phys. Rev. Lett.* 61 (6 1988), pp. 734–737. DOI: 10.1103/PhysRevLett.61.734. URL: https://link.aps.org/doi/10.1103/PhysRevLett.61.734.

[51] L. Colombo, R. Resta, and S. Baroni. “Valence-band offsets at strained Si/Ge interfaces”. In: *Phys. Rev. B* 44 (11 1991), pp. 5572–5579. DOI: 10.1103/PhysRevB.44.5572. URL: https://link.aps.org/doi/10.1103/PhysRevB.44.5572.

[52] C. Kittel. *Introduction to Solid State Physics*. Wiley, 2004. ISBN: 9780471415268. URL: https://books.google.hr/books?id=kym4QgAACAAJ.

[53] H. Taguchi et al. “High-temperature phase transition of CaMnO3”. In: *Journal of Solid State Chemistry* 78.2 (1989), pp. 312–315. ISSN: 0022-4596. DOI: https://doi.org/10.1016/0022-4596(89)90113-8. URL: https://www.sciencedirect.com/science/article/pii/0022459689901138.

[54] T. Negas and R. S. Roth. “The system SrMnO3x”. In: *Journal of Solid State Chemistry* 1.3 (1970), pp. 409–418. ISSN: 0022-4596. DOI: https://doi.org/10.1016/0022-4596(70)90123-4. URL: https://www.sciencedirect.com/science/article/pii/0022459670901234.

[55] T. Negas and R. Roth. “Phase equilibria and structural relations in the system BaMnO3x”. In: *Journal of Solid State Chemistry* 3.3 (1971), pp. 323–339. ISSN: 0022-4596. DOI: https://doi.org/10.1016/0022-4596(71)90068-5. URL: https://www.sciencedirect.com/science/article/pii/0022459671900685.

[56] Z. Zeng, M. Greenblatt, and M. Croft. “Large magnetoresistance in antiferromagnetic $\mathrm{CaMnO}_{3-\mathrm{ffi}}$”. In: *Phys. Rev. B* 59 (13 1999), pp. 8784–8788. DOI: 10.1103/PhysRevB.59.8784. URL: https://link.aps.org/doi/10.1103/PhysRevB.59.8784.

[57] S. F. Matar. “Ab initio investigations in magnetic oxides”. In: *Progress in Solid State Chemistry* 31.4 (2003), pp. 239–299.

[58] S. Bhattacharjee, E. Bousquet, and P. Ghosez. “Engineering multiferroism in CaMnO 3”. In: *Physical review letters* 102.11 (2009), p. 117602.

[59] K. Poeppelmeier et al. “Structure determination of CaMnO3 and CaMnO2.5 by X-ray and neutron methods”. In: *Journal of Solid State Chemistry* 45.1 (1982), pp. 71–79. ISSN: 0022-4596. DOI: https://doi.org/10.1016/0022-4596(82)90292-4. URL: https://www.sciencedirect.com/science/article/pii/0022459682902924.

[60] K. Kuroda et al. “The crystal structure of -SrMnO3”. In: *Journal of Solid State Chemistry* 38.3 (1981), pp. 297–299. ISSN: 0022-4596. DOI: https://doi.org/10.1016/0022-4596(81)90059-1. URL: https://www.sciencedirect.com/science/article/pii/0022459681900591.

[61] S. Qin et al. “High-Pressure Synthesis and Magnetism of the 4H-BaMnO3 Single Crystal and Its 6H-Type Polymorph”. In: *Inorganic Chemistry* 60.21 (2021). PMID: 34658238, pp. 16308–16315. DOI: 10.1021/acs.inorgchem.1c02155. eprint: https://doi.org/10.1021/acs.inorgchem.1c02155. URL: https://doi.org/10.1021/acs.inorgchem.1c02155.

[62] D. W. Boukhvalov and I. V. Solovyev. "Defects of the crystal structure and Jahn-Teller distortion in $BiMnO_3$". In: *Phys. Rev. B* 82 (24 2010), p. 245101. DOI: 10.1103/PhysRevB.82.245101. URL: https://link.aps.org/doi/10.1103/PhysRevB.82.245101.

[63] P. Chen and R. Zhu. "Overcoming the performance deadlock by ideal-bandgap perovskites". In: *Matter* 4.5 (2021), pp. 1445–1447. ISSN: 2590-2385. DOI: https://doi.org/10.1016/j.matt.2021.04.007. URL: https://www.sciencedirect.com/science/article/pii/S2590238521001685.

[64] J. Jung et al. "Determination of electronic band structures of CaMnO 3 and LaMnO 3 using optical-conductivity analyses". In: *Physical Review B* 55.23 (1997), p. 15489.

[65] A. Žužić et al. "The optical properties of strontium manganite thin films prepared by novel phototreatment technique". In: *Journal of alloys and compounds* 951 (2023), p. 169972.

[66] A. Sukserm, U. Pinsook, and T. Bovornratanaraks. "Structural phase transition of G-type antiferromagnetic SrMnO3 under pressure". In: *Physica Scripta* 99.7 (2024), p. 075931.

[67] W. Matysiak, T. Tański, and W. Smok. "Study of optical and dielectric constants of hybrid SnO2 electrospun nanostructures". In: *Applied Physics A* 126.2 (2020), p. 115.

[68] S. Goldsmith, E. Çetinörgü, and R. Boxman. "Modeling the optical properties of tin oxide thin films". In: *Thin Solid Films* 517.17 (2009). 4th International Conference on Technological Advances of Thin Films and Surface Coatings, pp. 5146–5150. ISSN: 0040-6090. DOI: https://doi.org/10.1016/j.tsf.2009.03.019. URL: https://www.sciencedirect.com/science/article/pii/S0040609009004702.

[69] A. R. Goñi et al. "Dependence on pressure of the refractive indices of wurtzite ZnO, GaN, and AlN". In: *Phys. Rev. B* 90 (4 2014), p. 045208. DOI: 10.1103/PhysRevB.90.045208. URL: https://link.aps.org/doi/10.1103/PhysRevB.90.045208.

[70] I. Sta et al. "Structural and optical properties of TiO2 thin films prepared by spin coating". In: *Journal of sol-gel science and technology* 72.2 (2014), pp. 421–427.

[71] J. Y. Kim et al. “High-Efficiency Perovskite Solar Cells”. In: *Chemical Reviews* 120.15 (2020). PMID: 32786671, pp. 7867–7918. DOI: 10.1021/acs.chemrev.0c00107. eprint: https://doi.org/10.1021/acs.chemrev.0c00107. URL: https://doi.org/10.1021/acs.chemrev.0c00107.

[72] Q. Jiang, X. Zhang, and J. You. “SnO2: A Wonderful Electron Transport Layer for Perovskite Solar Cells”. In: *Small* 14.31 (2018), p. 1801154. DOI: https://doi.org/10.1002/smll.201801154. eprint: https://onlinelibrary.wiley.com/doi/pdf/10.1002/smll.201801154. URL: https://onlinelibrary.wiley.com/doi/abs/10.1002/smll.201801154.

[73] J. P. Correa Baena et al. “Highly efficient planar perovskite solar cells through band alignment engineering”. In: *Energy Environ. Sci.* 8 (10 2015), pp. 2928–2934. DOI: 10.1039/C5EE02608C. URL: http://dx.doi.org/10.1039/C5EE02608C.

[74] D.-Y. Son et al. “Effects of Seed Layer on Growth of ZnO Nanorod and Performance of Perovskite Solar Cell”. In: *The Journal of Physical Chemistry C* 119.19 (2015), pp. 10321–10328. DOI: 10.1021/acs.jpcc.5b03276. eprint: https://doi.org/10.1021/acs.jpcc.5b03276. URL: https://doi.org/10.1021/acs.jpcc.5b03276.

[75] A. F. Akbulatov et al. “The impact of ZnO on the stability of perovskite films and solar cells: Surface chemistry rules the game!” In: *Materials Today Energy* 47 (2025), p. 101747. ISSN: 2468-6069. DOI: https://doi.org/10.1016/j.mtener.2024.101747. URL: https://www.sciencedirect.com/science/article/pii/S2468606924002594.

[76] J. Almeida et al. “Synthesis and characterization of NiMn2O4 nanoparticles using gelatin as organic precursor”. In: *Journal of Magnetism and Magnetic Materials* 320.14 (2008), e304–e307. ISSN: 0304-8853. DOI: https://doi.org/10.1016/j.jmmm.2008.02.062. URL: https://www.sciencedirect.com/science/article/pii/S0304885308001662.

[77] P. Khaenamkaew et al. “Crystal Structure, Lattice Strain, Morphology, and Electrical Properties of SnO2 Nanoparticles Induced by Low Calcination Temperature”. In: *Advances in Materials Science and Engineering* 2020.1 (2020), p. 3852421. DOI: https://doi.org/10.1155/2020/3852421. eprint: https://onlinelibrary.wiley.com/doi/pdf/10.1155/2020/3852421. URL: https://onlinelibrary.wiley.com/doi/abs/10.1155/2020/3852421.

[78] S. Wu et al. “Exploring the Phase Transformation Mechanism of Titanium Dioxide by High Temperature in Situ Method”. In: *IOP Conference Series: Materials Science and Engineering* 493.1 (2019), p. 012010. DOI: 10.1088/1757-899X/

493/1/012010. URL: https://doi.org/10.1088/1757-899X/493/1/012010.

[79] M. H. Huang et al. "Room-Temperature Ultraviolet Nanowire Nanolasers". In: *Science* 292.5523 (2001), pp. 1897–1899. DOI: 10.1126/science.1060367. eprint: https://www.science.org/doi/pdf/10.1126/science.1060367. URL: https://www.science.org/doi/abs/10.1126/science.1060367.

[80] Z. M. Jarzebski and J. P. Marton. "Physical Properties of SnO2 Materials: II . Electrical Properties". In: *Journal of The Electrochemical Society* 123.9 (1976), p. 299C. DOI: 10.1149/1.2133090. URL: https://doi.org/10.1149/1.2133090.

[81] H. Tang et al. "Photoluminescence in TiO2 anatase single crystals". In: *Solid State Communications* 87.9 (1993), pp. 847–850. ISSN: 0038-1098. DOI: https://doi.org/10.1016/0038-1098(93)90427-0. URL: https://www.sciencedirect.com/science/article/pii/003810989390427O.

[82] M. E. Arroyo-de Dompablo, A. Morales-García, and M. Taravillo. "DFT+U calculations of crystal lattice, electronic structure, and phase stability under pressure of TiO2 polymorphs". In: *The Journal of Chemical Physics* 135.5 (2011), p. 054503. ISSN: 0021-9606. DOI: 10.1063/1.3617244. eprint: https://pubs.aip.org/aip/jcp/article-pdf/doi/10.1063/1.3617244/15439375/054503_1_online.pdf. URL: https://doi.org/10.1063/1.3617244.

[83] G. Di Liberto, S. Tosoni, and G. Pacchioni. "Nature and Role of Surface Junctions in BiOIO3 Photocatalysts". In: *Advanced Functional Materials* 31.20 (), p. 2009472. DOI: https://doi.org/10.1002/adfm.202009472. eprint: https://advanced.onlinelibrary.wiley.com/doi/pdf/10.1002/adfm.202009472. URL: https://advanced.onlinelibrary.wiley.com/doi/abs/10.1002/adfm.202009472.

[84] N. Sultana et al. "Unveiling the structures and electronic properties of CH3NH3PbI3 interfaces with TiO2, ZnO, and SnO2: a first-principles study". In: *Journal of Materials Science* 54 (Nov. 2019). DOI: 10.1007/s10853-019-03867-0.

[85] M. J. Akhtar et al. "Bulk and Surface Simulation Studies of La1-xCaxMnO3". In: *Chemistry of Materials* 18.6 (2006), pp. 1552–1560. DOI: 10.1021/cm052260r. eprint: https://doi.org/10.1021/cm052260r. URL: https://doi.org/10.1021/cm052260r.

[86] D. Imbrenda et al. “Surface- and strain-tuning of the optical dielectric function in epitaxially grown CaMnO3”. In: *Applied Physics Letters* 108.8 (2016), p. 082902. ISSN: 0003-6951. DOI: 10.1063/1.4942374. eprint: https://pubs.aip.org/aip/apl/article-pdf/doi/10.1063/1.4942374/13765491/082902_1_online.pdf. URL: https://doi.org/10.1063/1.4942374.

[87] M. B. Nielsen et al. “Phase stability of the $SrMnO_3$ hexagonal perovskite system at high pressure and temperature”. In: *Phys. Rev. B* 90 (21 2014), p. 214101. DOI: 10.1103/PhysRevB.90.214101. URL: https://link.aps.org/doi/10.1103/PhysRevB.90.214101.

[88] N. Hamdad. “The ground states properties and the spin effect on the cubic and hexagonal perovskite manganese oxide BaMnO3: GGA+U calculation”. In: *Physica B: Condensed Matter* 406.6 (2011), pp. 1194–1203. ISSN: 0921-4526. DOI: https://doi.org/10.1016/j.physb.2010.11.018. URL: https://www.sciencedirect.com/science/article/pii/S0921452610010732.

[89] P.-O. Löwdin. “On the Non-Orthogonality Problem Connected with the Use of Atomic Wave Functions in the Theory of Molecules and Crystals”. In: *The Journal of Chemical Physics* 18.3 (Mar. 1950), pp. 365–375. ISSN: 0021-9606. DOI: 10.1063/1.1747632. eprint: https://pubs.aip.org/aip/jcp/article-pdf/18/3/365/18797214/365_1_online.pdf. URL: https://doi.org/10.1063/1.1747632.

[90] W. S. Suh et al. “Optimal film thickness and Sn oxidation state of sputter-deposited SnO 2 electron transport layers for efficient perovskite solar cells”. In: *Sustainable Energy & Fuels* 8.22 (2024), pp. 5214–5224.

[91] T. Du et al. “Light-intensity and thickness dependent efficiency of planar perovskite solar cells: charge recombination versus extraction”. In: *J. Mater. Chem. C* 8 (36 2020), pp. 12648–12655. DOI: 10.1039/D0TC03390A. URL: http://dx.doi.org/10.1039/D0TC03390A.

[92] R. Jacobs, J. Booske, and D. Morgan. “Understanding and Controlling the Work Function of Perovskite Oxides Using Density Functional Theory”. In: *Advanced Functional Materials* 26.30 (2016), pp. 5471–5482. DOI: https://doi.org/10.1002/adfm.201600243. eprint: https://advanced.onlinelibrary.wiley.com/doi/pdf/10.1002/adfm.201600243. URL: https://advanced.onlinelibrary.wiley.com/doi/abs/10.1002/adfm.201600243.

[93] Z. Zhong and P. Hansmann. “Tuning the work function in transition metal oxides and their heterostructures”. In: *Phys. Rev. B* 93 (23 2016), p. 235116. DOI: 10.

1103/PhysRevB.93.235116. URL: https://link.aps.org/doi/10.1103/PhysRevB.93.235116.

[94] C. Kaewmeechai, Y. Laosiritaworn, and A. P. Jaroenjittichai. "DFT band alignment of polar and nonpolar GaN/MgGeN2, ZnO/MgGeN2 and GaN/ZnO heterostructures for optoelectronic device design". In: *Applied Surface Science* 533 (2020), p. 147503. ISSN: 0169-4332. DOI: https://doi.org/10.1016/j.apsusc.2020.147503. URL: https://www.sciencedirect.com/science/article/pii/S0169433220322601.

[95] L. Bengtsson. "Dipole correction for surface supercell calculations". In: *Phys. Rev. B* 59 (19 1999), pp. 12301–12304. DOI: 10.1103/PhysRevB.59.12301. URL: https://link.aps.org/doi/10.1103/PhysRevB.59.12301.

[96] T. Minemoto and M. Murata. "Theoretical analysis on effect of band offsets in perovskite solar cells". In: *Solar Energy Materials and Solar Cells* 133 (2015), pp. 8–14. ISSN: 0927-0248. DOI: https://doi.org/10.1016/j.solmat.2014.10.036. URL: https://www.sciencedirect.com/science/article/pii/S0927024814005674.

[97] D. N. Q. Agha and Q. T. Algwari. "The influence of the conduction band engineering on the perovskite solar cell performance". In: *Results in Optics* 9 (2022), p. 100291. ISSN: 2666-9501. DOI: https://doi.org/10.1016/j.rio.2022.100291. URL: https://www.sciencedirect.com/science/article/pii/S2666950122000803.

[98] P. Giannozzi et al. "Advanced capabilities for materials modelling with Quantum ESPRESSO". In: *Journal of physics: Condensed matter* 29.46 (2017), p. 465901.

[99] D. Hamann. "Optimized norm-conserving Vanderbilt pseudopotentials". In: *Physical Review B—Condensed Matter and Materials Physics* 88.8 (2013), p. 085117.

[100] N. E. Kirchner-Hall et al. "Extensive Benchmarking of DFT+U Calculations for Predicting Band Gaps". In: *Applied Sciences* 11.5 (2021). ISSN: 2076-3417. DOI: 10.3390/app11052395. URL: https://www.mdpi.com/2076-3417/11/5/2395.